Diffusion, Deformation, and Damage in Lithium-Ion Batteries and Microelectronics

Diffusion, Deformation, and Damage in Lithium-Ion Batteries and Microelectronics

A dissertation presented

by

George Mathews Pharr V

to

The School of Engineering and Applied Sciences

in partial fulfillment of the requirements

for the degree of

Doctor of Philosophy

in the subject of

Engineering Sciences

Harvard University

Cambridge, Massachusetts

April, 2014

Thesis Advisors
Zhigang Suo, Joost Vlassak

Author
George Mathews Pharr V

Diffusion, Deformation, and Damage in Lithium-Ion Batteries and Microelectronics

Abstract

This thesis explores mechanical behavior of microelectronic devices and lithium-ion batteries. We first examine electromigration-induced void formation in solder bumps by constructing a theory that couples electromigration and creep. The theory can predict the critical current density below which voids do not form. Due to the effects of creep, this quantity is found to be independent of the solder size and decrease exponentially with increasing temperature, different from existing theories.

We then investigate the interplay between mass transport, deformation, stress, and fracture in lithium-ion battery electrodes. First, we model fracture of elastic electrodes by combining ideas from diffusion kinetics and fracture mechanics. Next, we examine mechanics of high-capacity lithium-ion batteries, which demonstrate inelastic deformation, by constructing a model that accounts for diffusion and elastic-plastic deformation. These models suggest that fracture is prevented in small and soft electrode materials that are cycled slowly.

To investigate crystalline silicon electrodes, we construct a continuum model of concurrent reaction-controlled kinetics and plasticity. To quantify the kinetics of

the lithiation process, we perform electrochemical experiments on crystalline silicon wafers of various orientations. Using the velocities measured in these experiments and our continuum model, we correctly predict anisotropic morphologies and fracture patterns developed in crystalline silicon nanopillars.

We then measure the fracture energy of lithiated silicon, finding it to be similar to that of pure silicon and essentially independent of the lithium concentration. These findings demonstrate that lithiated silicon has a peculiar ability to flow plastically but fracture in a brittle manner. To investigate this interesting combination of properties, we measure stresses in silicon thin films as a function of charging rate. Increasing the rate of lithiation resulted in a corresponding increase in the flow stress, indicating rate-sensitive plasticity.

Microelectronics and lithium-ion batteries are rich in mechanics, requiring considerations from large deformation, plasticity, creep, kinetics, and fracture mechanics. These systems involve an intimate coupling between mechanics and a number of other fields, such as chemical reactions, electric fields, mass transport, and electrochemistry. Thus, it is believed that this thesis will provide general insight into systems that involve coupling between mechanics and other disciplines.

Table of Contents

Acknowledgements

To me, this section is the most important part of my thesis, for one simple reason: without the people mentioned here, there would be no thesis of which to speak. My professors have stimulated me and provided me essential technical skills. My advisors have inspired, motivated, and encouraged me. My collaborators have taken my research to another level. My friends and family have supported me through thick and thin. I lack the eloquence to properly articulate my gratitude to these people but I will try here nevertheless.

The main reason I decided to come to Harvard is that I had heard so many great things about my advisors-to-be, Professor Zhigang Suo and Professor Joost Vlassak. In this regard, I have not been the least bit disappointed. Both are brilliant scholars who have a deep love for their craft. Both have open-door policies and foster friendly and collaborative research groups. Both have given me extreme freedom as to what research to pursue. Both are incredibly supportive, not just in terms of research but also in terms of life in general. The strong collaboration between Zhigang and Joost allowed me to pursue a joint theoretical and experimental approach to my work, which has always been a goal of mine.

Zhigang's enthusiasm is contagious; he inspires people without even trying. He has a way of making everything fun, and I have always appreciated his glass-half-full attitude. Zhigang also has a natural ability for elucidating the essential physics of a problem. His clear and logical way of thinking makes problems

easily understandable, even to someone such as myself. I am particularly thankful for Zhigang's patience with me. In hindsight, I knew next to nothing when I came to Harvard. It is nothing short of a miracle that Zhigang put up with me then. In the future, I will certainly try my best to be as patient with people as Zhigang was with me.

Joost has provided me invaluable guidance on conducting experiments. He has a clear way of thinking through what could be happening in an experiment from every possible angle. Joost also has a keen eye for detail and holds high standards of research quality and thoroughness. I really appreciate these traits and will strive to incorporate them in my future research. I have knocked on Joost's door for help more than I would like to admit, and he always takes the time to answer my questions. Joost is also an exceptional motivator, and I have learned from his perseverance. As an example, there was one particular project I felt might be a lost cause. However, Joost kept encouraging me not to give up, and eventually everything came together. For this, I am deeply indebted to him.

I would also like to thank my wonderful collaborators. My closest collaborator is Kejie Zhao. It has been a privilege to co-author 9 publications with him. Kejie and I work well together as a team, playing off each other's strengths. Once Kejie has an idea, nothing can stop him from seeing it come to fruition, especially not sleep. His drive has inspired me, greatly increasing my productivity. At some point, Zhigang told us we were working together too much and needed a divorce. We tried for a while, but we just could not seem to keep ourselves apart

from each other. I hope my wife is not jealous. I would also like to thank my other collaborators from Harvard: Prof. Efthimios Kaxiras, Prof. Jeong-Yun Sun, Prof. Xinwei Wang, Prof. Shengqiang Cai, Dr. John Gregoire, Dr. Wei Li Wang, Dr. Georgios Tritsaris, Dr. Laurence Brassart, Yong-Seok Choi, Dogus Cubuk, and Lauren Hartle, and my collaborators from Intel: Dr. Fan-Yi Ouyang and Dr. Pilin Liu.

I would also like to thank a number of other distinguished professors at Harvard with whom I have had the privilege of interacting, including Prof. Katia Bertoldi, Prof. David Clarke, Prof. John Hutchinson, Prof. Mike Aziz, Prof. Howard Stone, Prof. Michael Brenner, and many others. I would like to give a special thanks to Prof. Frans Spaepen, whose class AP 282 I had the honor of TFing. Also, he was always willing to talk to me and gave me loads of advice concerning my research. I am also greatly indebted to my committee members Prof. Jim Rice and Prof. Shriram Ramanathan.

I have learned so much from my interaction with the Vlassak and Suo groups. A special thanks to Prof. Nanshu Lu, Prof. Xuanhe Zhao, Prof. Jian Zhu, Prof. Tiefeng Li, Dr. Yuhang Hu, Dr. Christoph Keplinger, Dr. Gidong Sim, Dr. Patrick McCluskey, Dr. Han Li, Dr. Xiaodong Zhang, Dr. Rainer Kaltseis, Dr. Keith Choon Chiang Foo, Dr. Jiangshui Huang, Lihua Jin, Philipp Rothemund, Widusha Illeperuma, Jianyu Li, Tongqing Lu, Kechao Xiao, Kamyar Davoudi, Dongwoo Lee, Qihan Liu, and Chao Chen.

I would also like to extend thanks to my other friends from Harvard: Prof. Rebecca Kramer, Dr. Roger Diebold, Dr. Amanda Randles, Dr. Katie Hoffman, Dr. Joe

Martel, John Kolinski, John Platt, Zhiyan Wei, Bill Bonificio, Brian Huskinson, Kian Kerman, Michael Cox, and Josh Goss. These people helped keep me sane during my time here.

I would also like to convey appreciation to the Harvard School of Engineering and Applied Science, Intel, the National Science Foundation Graduate Research Fellowship Program, and the National Defense Science and Engineering Graduate Fellowship for financial support. Without this support, this thesis would not be possible.

Finally, I would like to dedicate this thesis to my family. You have done so much for me that my words cannot do it justice. I thank my parents for their unconditional love, support, and belief in me. They have encouraged me to pursue my dreams, whatever they may be. They have shown me how to be kind, friendly, considerate, humble, appreciative, and loving. They have taught me to work hard and to play hard. One day, I hope I can instill these same values in my children. I would also like to thank my brother, grandparents, aunts, uncles, and cousins, who have provided me with strength through their steady love and support. Last but not least, my wife, Kate. You have supported me with unwavering love through all of my ups and downs. You are kind, caring, intelligent, funny, and beautiful. We have grown so much together through the years, and I am so lucky I get to spend the rest of my life with you.

Chapter 1

Introduction

This thesis investigates the mechanical behavior of microelectronic devices and lithium-ion batteries. These systems are rich in mechanics, as they require considerations from large deformation, plasticity, creep, kinetics, and fracture mechanics. Moreover, they involve an intimate coupling between mechanics and a number of other fields, such as chemical reactions, electric fields, mass transport, and electrochemistry. In these systems, electric fields can drive mass transport and promote chemical reactions. As atoms move and rearrange, the material deforms. Under constraint, this deformation creates a field of stress, which may lead to damage in the material, such as fracture, void formation, or undesired morphological change. Meanwhile, the mechanical stresses generated can significantly affect other processes in the system. For example, atoms tend to be transported from regions of relatively high compressive stress to regions of relatively low compressive stress. Similarly, if large enough stresses are built up, chemical reactions can be shut off entirely. The remainder of this chapter provides an introduction to microelectronics and lithium-ion batteries.

1.1 Electromigration-induced damage in microelectronic devices

Under an applied electric potential, electrons move through a metal from the negative terminal to the positive terminal. Owing to the delocalization of electrons in metals, this motion is mostly unimpeded, as indicated by the path of the leftmost electron in Figure 1.1. However, due to thermal vibrations or defects, such as vacancies (black square in Figure 1.1), electrons can collide with the metal atoms, as indicated by the path of the rightmost electron in Figure 1.1. During these collisions, electrons impart momentum to the metal atom. Since the mass of the electron is small compared that of the nucleus of the atom, the transferred momentum is usually too small to permanently displace the atoms. However, as the current density increases, the number of electrons colliding with atoms increases, thereby increasing the rate of atomic displacement. Such conditions result in mass transport under the influence of the electric field, which is termed electromigration.

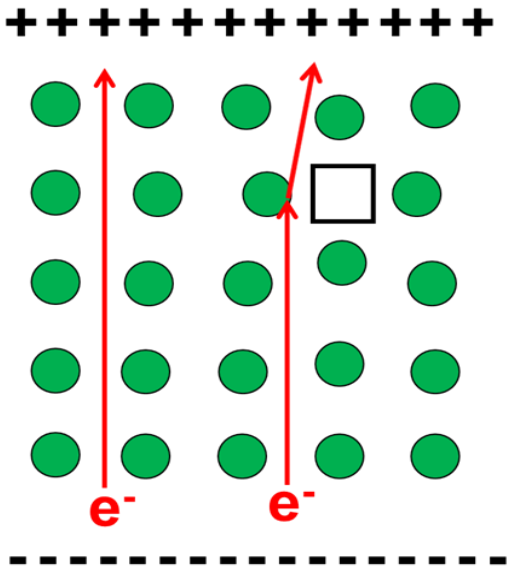

Figure 1.1. Under an electric field, atoms usually move freely through a metal lattice electron). Due to imperfections, such as vacancies (black square), electrons may collide with atoms, imparting momentum to them (rightmost electron).

Integrated circuits are microelectronic devices used in virtually all electronic equipment today. These devices consist of a set of electronic circuits on a single semiconductor chip. As this technology advances, the constituent components of these devices continue to decrease in size. Meanwhile, the power requirements for these components tend to stay the same or even increase. This combination of factors results in larger current densities, which have led to electromigration-induced damage in some devices. As an example, in aluminum films, electromigration was found to result in device failure due to the opening of interconnections.[1] Interestingly, in aluminum interconnect lines, Blech observed a critical current density, below which electromigration does not cause damage.[1] This phenomenon was attributed to the stresses that are built up during mass transport.[2] As material is transported from the cathode to the anode, a state of compression develops near the anode while a state of tension develops near the cathode. This resulting gradient in stress along the length of the line drives atoms back toward the cathode, counteracting electromigration. As the current density increases, larger stresses must be built up to counteract the diffusional flux from electromigration. However, at some point, the stress at either end of the interconnect is limited by some mechanism of failure, such as the formation of voids or the extrusion of the metal into the surrounding dielectrics. Thus, there is a so-called “critical current density,” above which damage of the device occurs.

Blech made his observations in metallic interconnect lines.[1],[2] Another component typically found in semiconductor devices is that of a solder bump (Figure

1.2).[3] A solder is a fusible metal alloy that is used to interconnect the semiconductor device (e.g., an integrated circuit) to a circuit board. During fabrication, the solder is deposited onto a pad of the integrated circuit and then aligned with a corresponding pad on the circuit board. The solder is then heated above the melting point and allowed to cool back to room temperature to create a mechanical and electrical connection between the components. Since the solder must be melted during the fabrication process, it is desirable for the solder to have a relatively low melting point.

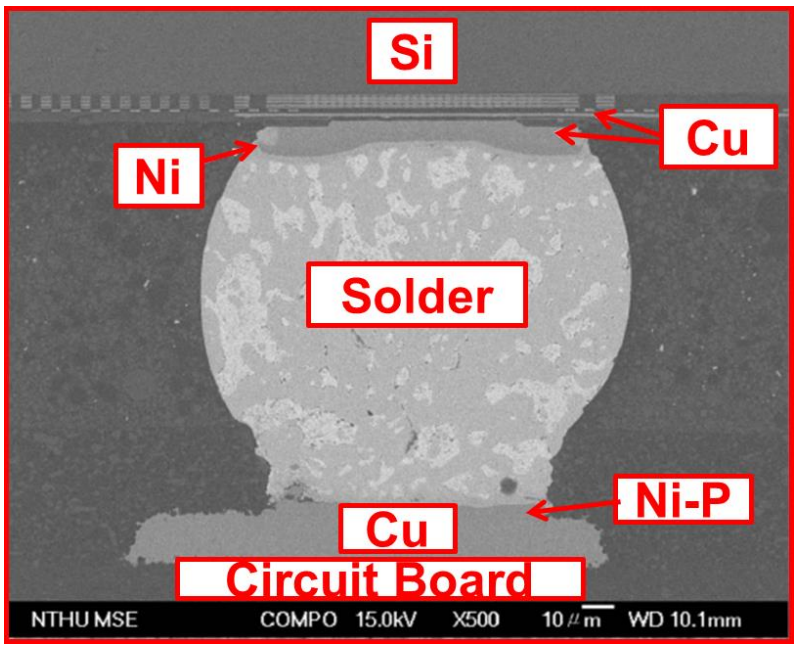

Figure 1.2. Micrograph of a flip chip solder joint. Figure adapted from Reference [3].

During operation of the microelectronic devices, current flows from the chip side, through the solder, and to the external circuitry (or vice-versa). Under certain conditions, this "current stressing" can lead to void formation and eventual failure of the connection.[4] For instance, in Figure 1.3, electrons are moving in the direction

as indicated by the arrow. After some time, voids are formed in the upstream region of the electron flow (red oval in Figure 1.3a). Once these voids are formed, they quickly propagate across the cross-section of the bump, leading to an open circuit and hence failure of the interconnect (Figure 1.3b).[4]

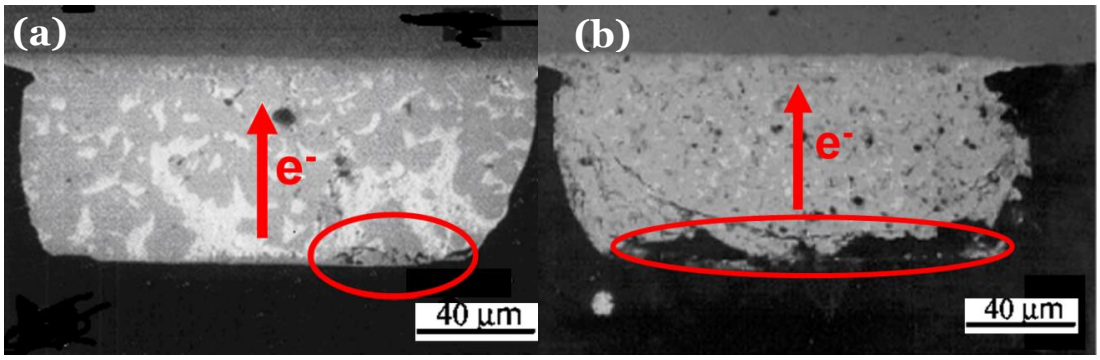

Figure 1.3. (a) Voids (red oval) can form in solders during operation. (b) These voids can propagate across the solder, leading to an open circuit (red oval). Figure adapted from Reference [4].

To model this electromigration-induced damage, Blech's analysis[1],[2] may seem appropriate. However, solder bumps present a further complication. Due to their low melting points, solders can reach ¾ of their melting point in terms of the absolute scale during operation. At these temperatures, significant deformation via a creep mechanism may occur. Thus, an additional rate process, creep, must be considered for proper analysis of electromigration in a solder bump. To do so, in Chapter 2 we construct a theory that couples electromigration and creep. Using material data, we demonstrate that creep effects are significant for proper analysis of practical solder systems. Furthermore, we find vastly different scaling of the critical current density on various physical parameters when the effects of creep are considered.

1.2 Kinetics, deformation, and fracture of lithium-ion battery electrodes

A lithium-ion battery is an electrochemical transducer, converting chemical energy to electrical energy and vice-versa. Within the battery, two electrodes are separated by an electrolyte (Figure 1.4). The electrodes host lithium atoms. The electrolyte conducts lithium only as an ionic species and does not conduct electrons. The electrodes are also connected by a wire that conducts only electrons. One of the electrodes (the negative electrode) has a large chemical potential of lithium relative to the other (the positive electrode). As a result, there is a driving force for lithium to move from the negative electrode to the positive one. To do so, a lithium atom must dissociate into a lithium ion and an electron. The lithium-ion then moves through the electrolyte and enters the positive electrode. Meanwhile, to maintain electroneutrality, an electron moves through the wire, powering an external device during the process. Upon reaching the positive electrode, the electron combines with the lithium-ion to form neutral lithium. This process is known as discharge (Figure 1.4). During charge, the battery is connected to an external power source, and the process is reversed.

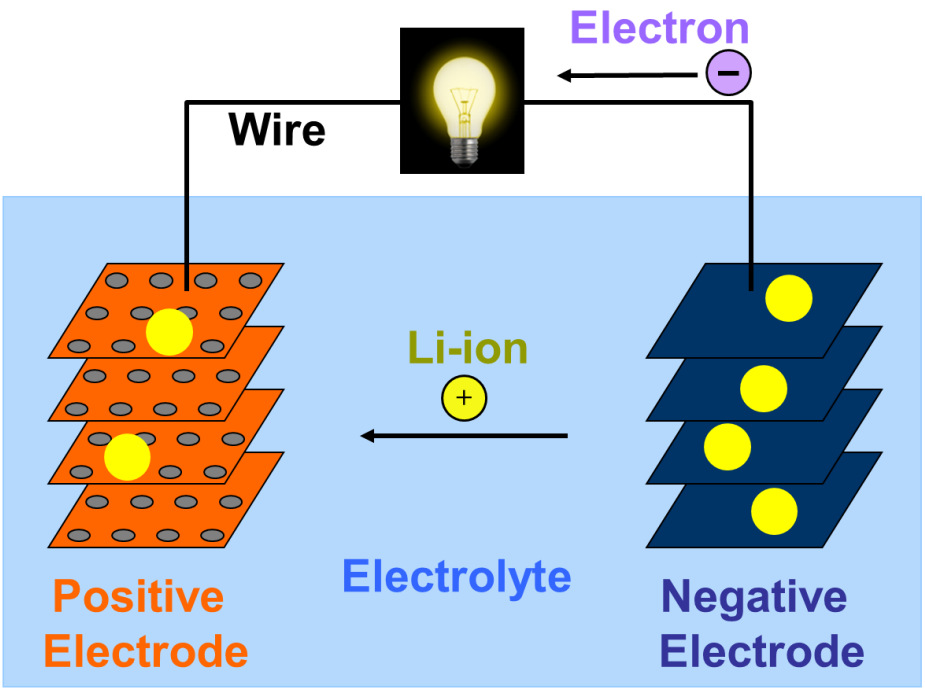

Figure 1.4. A schematic of a lithium-ion battery during discharge.

Lithium-ion batteries are known for their large energy and power densities, as compared to various existing battery technologies (Figure 1.5).[5] As a result, they have found widespread use in practice for applications sensitive to size as weight, such as electric vehicles and portable electronics – cellular phones, laptop computers, and power tools, among others.[6],[7] Within the context of these applications, there remains a demand for lower cost, longer lifetime, larger rate capabilities, and larger capacities.[8],[9] As a familiar example, cellular phones have to be charged every day or two, and laptop computers have to be charged every few hours. Increases in the volumetric capacities of lithium-ion batteries would extend the operating time between charges. Similarly, battery packs in all-electric cars account for a substantial portion of the weight of the car. Increases in the gravimetric capacities of the batteries would reduce the weight. As another example, larger

rate-capabilities would decrease the time required to charge the system and would improve performance in applications that have high demands for power, such as power tools and electric vehicles.

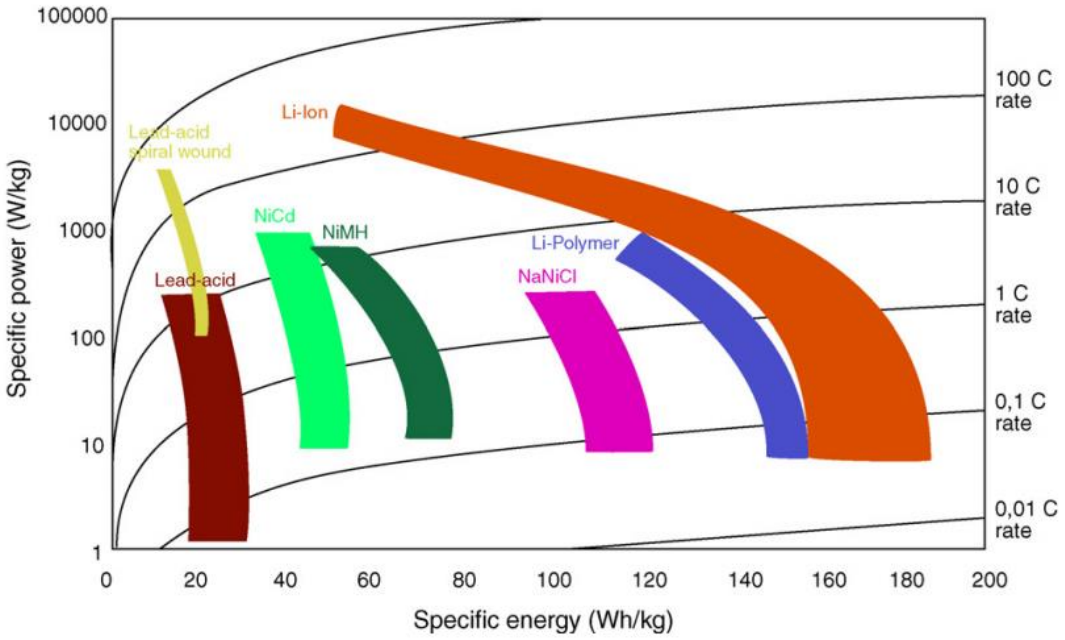

Figure 1.5. Comparison of various battery technologies in terms of specific power (vertical and specific energy (horizontal axis).[5]

Fortunately, a number of electrode materials with better performance exist. As an example, Table 1.1 shows a number of candidate materials for anodes.[10] The anode most commonly used in commercial lithium-ion batteries is that of graphite (C in Table 1.1). As can be seen in the Table 1.1, a number of alternative materials have better substantially characteristics than those of graphite. For instance, Si has more than ten times the theoretical specific capacity and charge density (i.e., gravimetric and volumetric capacities) than those of C.[10] However, mechanical degradation has been a bottleneck in commercializing many of these high-capacity systems. During charge and discharge, the amount of lithium in the host electrode varies significantly, resulting in deformation of the electrode. Materials with larger capacities tend to

deform more. For instance, from Table 1.1, graphite expands by only 12% while silicon expands by 320% upon full lithiation.[10] This deformation is often constrained by various means, such as grain boundaries, different phases of active and inactive materials, and phase boundaries.[11] Similarly, poor kinetics within the active materials can result in an inhomogeneous distribution of lithium and hence a mismatch in strain.[12] This constrained deformation generates stress, which can lead to fracture of the electrode materials. Indeed, fracture has been observed during cycling of a number of electrode materials, as shown in Figure 1.6.[13]-[15] This mechanical degradation can lead to the fading of the capacity of the battery, either by isolating active materials, increasing the electrical resistance, and/or by creating new surface area on which detrimental chemical reactions occur.[16]-[18] As previously mentioned, this mechanical degradation has been a bottleneck to the development of high-capacity electrodes. Thus, a proper understanding of how electrodes can sustain electrochemical cycling without mechanical degradation is vital for the development of high-capacity lithium-ion batteries.

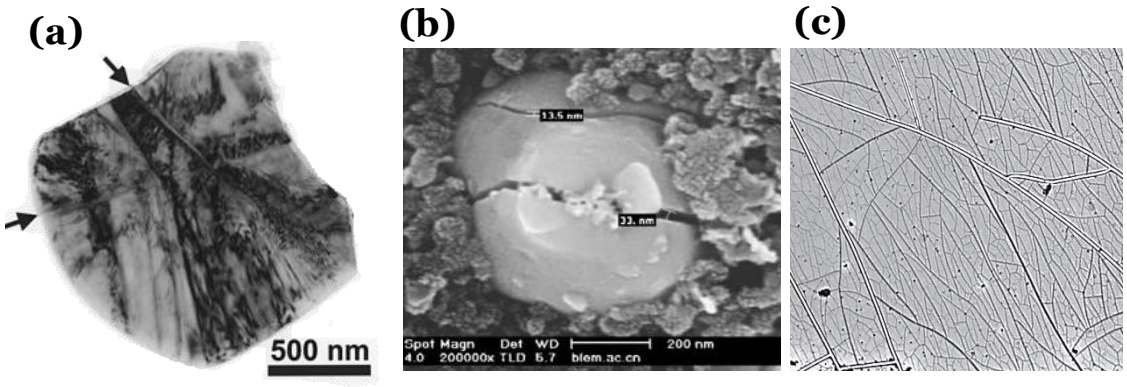

Figure 1.6. Fracture of (a) a $LiCoO_2$ particle after 50 electrochemical cycles,[13] (b) a $LiFePO_4$ particle after 50 electrochemical cycles,[14] and (c) a thin film of Si after one electrochemical cycle.[15]

Materials	**Li**	**C**	**$Li_4Ti_5O_{12}$**	**Si**	**Sn**	**Sb**	**Al**	**Mg**	**Bi**
Density (g/cm^3)	0.53	2.25	3.5	2.33	7.29	6.7	2.7	1.3	9.78
Lithiated phase	Li	LiC_6	$Li_7Ti_5O_{12}$	$Li_{4.4}Si$	$Li_{4.4}Sn$	Li_3Sb	LiAl	Li_3Mg	Li_3Bi
Specific capacity (mAh/g)	3,862	372	175	4,200	994	660	993	3,350	385
Charge density (mAh/cm^3)	2,047	837	613	9,786	7,246	4,422	2,681	4,355	3,765
Volume change (%)	100	12	1	320	260	200	96	100	215
Potential vs. Li (~V)	0	0.05	1.6	0.4	0.6	0.9	0.3	0.1	0.8

Table 1.1. Comparison of a number of properties of various anode materials. The table is adapted from Reference [10].

This thesis examines the interplay between mass transport, deformation, stress, and fracture in lithium-ion battery electrodes. In Chapter 3, we model fracture of electrodes by combining ideas from diffusion kinetics and fracture mechanics. We perform a numerical simulation to examine how to prevent fracture of a $LiCoO_2$ particle. In Chapter 4, we develop a mechanical model that demonstrates the importance of inelastic deformation in high-capacity electrodes. In particular, the model suggests that fracture of high-capacity electrodes can be prevented in small and soft electrode materials that are charged/discharged slowly. In Chapter 5, we investigate a promising design for high-capacity lithium-ion batteries: hollow, coated nano-structures. We analyze conditions to prevent fracture of active materials and debonding between the active and inactive materials. In

Chapters 6-7, we examine the initial lithiation of crystalline silicon electrodes, which is found to occur by a two-phase reaction mechanism. Chapter 6 builds a mechanical model that accounts for concurrent reaction-controlled kinetics and plasticity. The stresses that develop are found to contribute substantially to the driving force for lithiation, potentially shutting off lithiation completely. Chapter 7 provides an experimental investigation that quantifies the anisotropy of lithiation kinetics in crystalline silicon electrodes. A kinetic model accounting for coupling between redox reactions, diffusion, and chemical reactions is also presented. In Chapter 8, we develop an experimental technique to measure the fracture energy of high-capacity electrodes. We use this technique to measure the fracture energy of lithiated silicon electrodes as a function of lithium concentration**.** In Chapter 9, we measure stresses in silicon thin films as a function of charging rate. Increasing the rate of lithiation resulted in a corresponding increase in the flow stress, indicating rate-sensitive plasticity. Rate-sensitive material parameters are quantified, providing insight into the unusual ability of lithiated silicon to flow plastically but fracture in a brittle manner.

Chapter 2

Concurrent Electromigration and Creep in Solders

2.1 Introduction

In microelectronic devices, intense electric currents motivate atoms to diffuse—a process known as electromigration. Although electromigration is present in many components of the devices, the current density needed to cause electromigration in solder bumps is much smaller than in any other components.[19] Electromigration can cause the bumps to form voids, leading to failure.[20]

Blech observed in an interconnect line a critical current density, below which electromigration does not cause damage.[1] This observation was interpreted by Blech and Herring as follows:[2] as the electric current causes atoms to migrate from one end to the other along the interconnect, a gradient of stress builds up, counteracting electromigration. After some time, the interconnect develops a steady-state stress gradient, and net migration of atoms stops. The magnitude of the stress at either end of the interconnect is limited by some mechanisms of failure, such as the formation of voids and extrusion of the metal into the surrounding dielectrics, so that the achievable stress gradient is large in short interconnects. Consequently, short interconnects are immortal, immune from electromigration-induced failure[21]-[24]. This consideration has played a significant role in the design of interconnects.[19],[25]-[27]

It is tempting to apply the Blech-Herring analysis to solder bumps. However, solder bumps require an additional consideration. During operation, a bump can reach ¾ of its melting point,[28] and the bump creeps.[29] The bump is often surrounded by relatively compliant molding compounds, possibly allowing creep to relax the stress in the bump. By contrast, an interconnect is often confined by relatively stiff dielectrics, which enables the interconnect to retain hydrostatic stress in the presence of creep.[30]

To apply the Blech-Herring analysis to solder bumps, this chapter considers concurrent electromigration and creep. When electric current flows in the bump, stress is generated by electromigration, but relaxed by creep. After some time, the bump develops a steady-state stress field. To determine this steady-state stress field, Section 2.2 reviews a theory of concurrent electromigration and creep. Section 2.3 shows that the relative rates of the two processes—electromigration and creep—can be quantified by an intrinsic length. When the height of the bump is small compared to the intrinsic length, electromigration is fast relative to creep, and the theory recovers the classical prediction of Blech and Herring, in which the steady-state stress is linearly distributed in the bump. When the height of the bump is large compared to the intrinsic length, electromigration is slow relative to creep, and the theory reveals a unique situation, in which the steady-state stress nearly vanishes in the bump, except in a thin layer around the boundary of the bump.

These two limiting cases, as well as the intermediate behavior, are illustrated in Section 2.4 with a thin film. Section 2.5 then establishes a critical stress above

which voids will grow, based on the Laplace condition. Section 2.6 uses Pb-free solder data to investigate how the critical current density needed to cause void nucleation depends on various parameters of the solder. We find that, at normal operating temperatures, for a SnAg4Cu0.5 solder bump larger than ~1 μm, creep is important, and the Blech-Herring analysis is inadequate. Section 2.7 compares the theoretical predictions to experimental observations. Finally, in Section 2.8 we justify our approximation of the solder bump as a thin film by comparison to 3D simulations.

2.2 Theory of concurrent electromigration and creep

When electric current passes through a solder bump, the flow of electrons—the electron wind—motivates atoms of the bump to diffuse. As atoms relocate from the cathode to the anode, a field of stress builds up in the bump, tensile at the cathode, and compressive at the anode. While electromigration generates stress, creep tends to relax it. After some time, the concurrent electromigration and creep set up a steady-state stress field in the bump. This section summarizes a previously developed theory of concurrent creep and diffusion.[31]

Following Darken[32], we imagine that inert markers are scattered throughout a material. These markers do not diffuse; rather, they move along with the deformation of the material. It should be noted that this idea is not merely hypothetical. Movements of markers in solder bumps have been visualized with diamond particles and arrays of nanoindentations.[33],[34] Let (x_1, x_2, x_3) represent

the coordinates of a fixed space, and $v_i(x_1,x_2,x_3,t)$ be the velocity vector of the marker at position (x_1,x_2,x_3) at time t. The gradient of the marker velocity defines the strain-rate tensor:

$$d_{ij} = \frac{1}{2}\left(v_{i,j} + v_{j,i}\right). \tag{2.1}$$

Let Ω be the volume per atom in the body. Imagine a plane fixed in space and perpendicular to the axis x_i. The net atomic flux, N_i, is the number of atoms that move across the plane, per unit area and per unit time, as shown in Figure 2.1. We can independently measure this net atomic flux and the marker velocity. The convection flux, v_i/Ω, is the number of atoms moving with the marker across the plane, per unit area per unit time. The difference between the two fluxes defines the self-diffusion flux J_i, namely,

$$N_i = J_i + \frac{v_i}{\Omega}. \tag{2.2}$$

This equation states that the net flux, N_i, is the sum of the diffusion flux, J_i, and the convection flux, v_i/Ω.

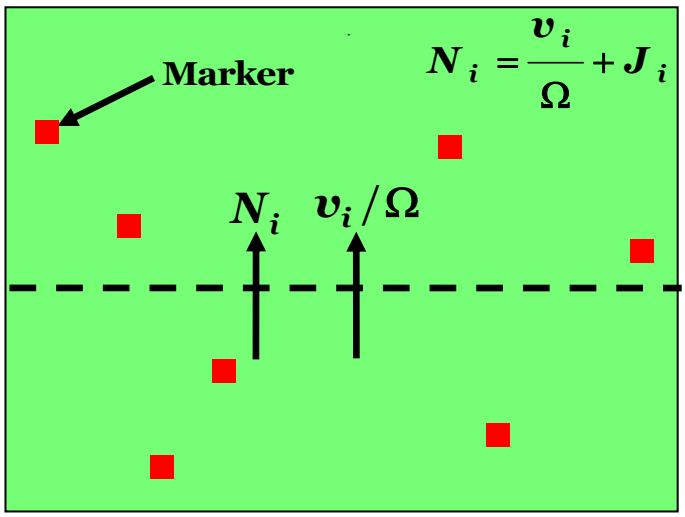

Figure 2.1. The marker velocity determines the convection flux, v_i/Ω. The net atomic flux, N_i, can also be independently measured. The atomic flux in excess of the convective flux defines the diffusion flux, J_i.

To emphasize the main features of this theory with minimum complication, we neglect elasticity. We also know that abundant sources and sinks, such as grain boundaries and dislocations, exist in a solder bump, as illustrated in Figure 2.2. As noted by Balluffi, these sources and sinks tend to maintain equilibrium concentrations of vacancies, which are usually small.[35] Therefore, a fixed volume will contain a constant number of atoms at all time, and the net atomic flux is divergence free,

$$N_{k,k} = 0 . \tag{2.3}$$

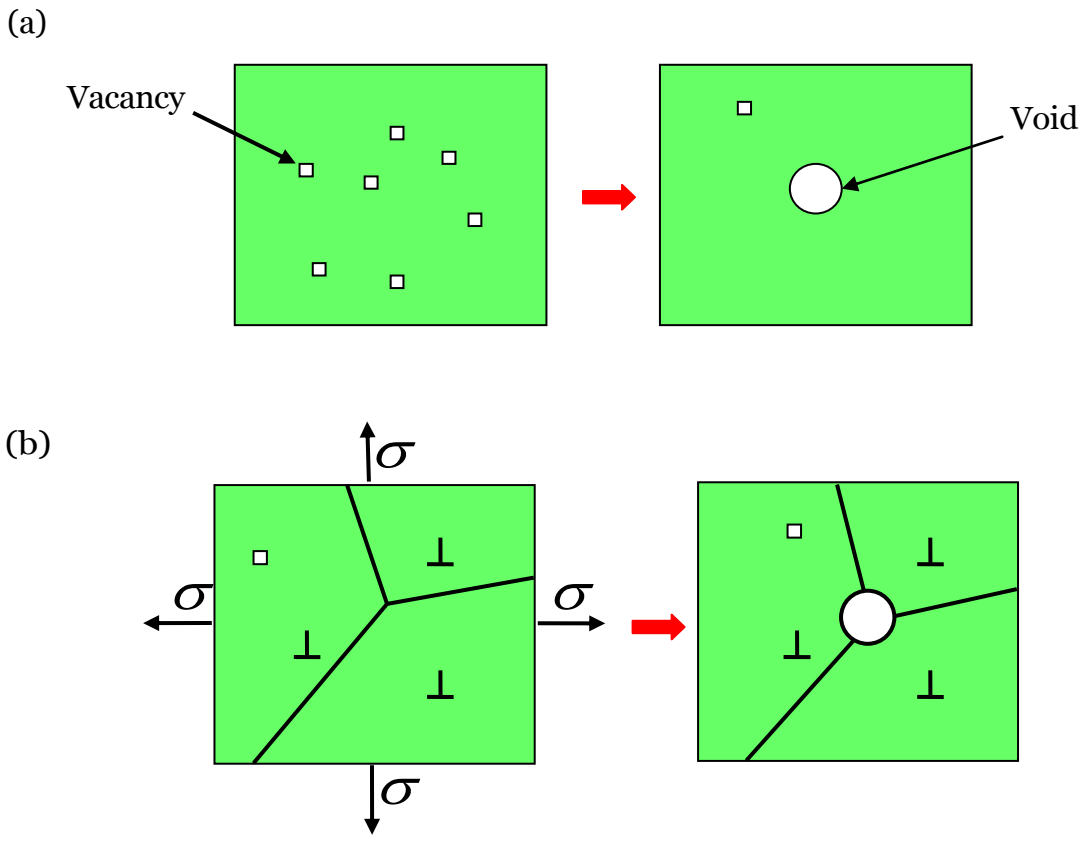

Figure 2.2. Two possible scenarios exist for growth of a void. In (a), flux divergence generates vacancies, which coalesce to form voids. In (b), sinks/sources keep vacancy concentrations at the equilibrium level. Flux divergence generates stress under constraint, leading to growth of a void.

A combination of Equations (2.2) and (2.3) gives

$$v_{k,k} = -\Omega J_{k,k} \ . \tag{2.4}$$

This equation states that even though the material is incompressible, the marker velocity has a divergence to compensate for the divergence in the diffusion flux.

We take the strain-rate to be the sum of that due to creep, $d_{ij}^{\ C}$, and that due to diffusion, $d_{ij}^{\ D}$,

$$d_{ij} = d_{ij}^{\ C} + d_{ij}^{\ D} \ . \tag{2.5}$$

We assume that the divergence in diffusion flux causes an equal strain rate in all three directions:

$$d_{ij}^{\ D} = -\frac{\Omega}{3} J_{k,k} \delta_{ij} \ , \tag{2.6}$$

where $\delta_{ij} = 1$ when $i = j$ and $\delta_{ij} = 0$ otherwise. We adopt this rule based on experimental evidence of its validity: it is consistent with observations of lateral shrinkage of thin foils during selective evaporation[36], and it correctly predicts the bending of a thin foil diffusion couple.[37] However, it can be modified, if for some reason atoms are preferentially placed on certain crystal planes.[38]

Combining Equations (2.1) and (2.4) – (2.6) gives the creep strain rate in terms of the marker velocity field:

$$d_{ij}^{\ C} = \frac{1}{2}\left(v_{i,j} + v_{j,i}\right) - \frac{1}{3} v_{k,k} \delta_{ij} \ . \tag{2.7}$$

Since creep generates negligible acceleration, the force balance equations can be written as

$$\left(\sigma_{ij}\right)_{,j} = 0, \ \text{in the volume} \tag{2.8}$$

$$\sigma_{ij} n_j = t_i, \ \text{on the surface} \ . \tag{2.9}$$

The mean stress is defined as

$$\sigma_m = \frac{1}{3}\left(\sigma_{11} + \sigma_{22} + \sigma_{33}\right). \tag{2.10}$$

The chemical potential induced by this mean stress is $\mu = -\Omega\sigma_m$. This quantity represents the free energy change associated with moving an atom in a stress-free reference body to a point in the material subject to mean stress σ_m. Following Blech and Herring[4], both the electron wind force and the gradient of the chemical potential drive diffusion:

$$J_i = \frac{D}{\Omega kT}\left[F_i + \left(\Omega\sigma_m\right)_{,i}\right], \tag{2.11}$$

where D is the self-diffusion coefficient, kT is the temperature in the unit of energy, and F_i is the electron wind force. The electron wind force relates to the electric current through the relation $F_i = Ze\rho j_i$, where Z is the effective valence of atoms, e is the elementary charge, ρ is the resistivity, and j is the current density.[39]

The deviatoric stress tensor is given by

$$s_{ij} = \sigma_{ij} - \sigma_m\delta_{ij}. \tag{2.12}$$

The equivalent stress is defined as

$$\sigma_e = \sqrt{3s_{ij}s_{ij}/2}. \tag{2.13}$$

The creep strain rate is commonly written as the product of the deviatoric stress and some function of the equivalent stress

$$d_{ij}^{C} = \alpha\left(\sigma_e\right)s_{ij}. \tag{2.14}$$

The function $\alpha(\sigma_e)$ is determined by fitting the relation between stress and strain rate measured under a simple stress state. For instance, performing a uniaxial

tension test, experimentalists may obtain a constitutive equation with the general form

$$\frac{d_{11}^{C}}{\dot{\varepsilon}_0} = f\left(\frac{\sigma_{11}}{\sigma_0}\right), \tag{2.15}$$

where d_{11}^{C} and σ_{11} are the strain rate and stress in the loading direction, σ_0 is a reference stress, and $\dot{\varepsilon}_0$ is the strain rate in the loading direction at the stress σ_0. For a uniaxial tensile test the equivalent stress is $\sigma_e = \sigma_{11}$ and the deviatoric stress is $s_{11} = 2\sigma_{11}/3$. Thus, equating (2.14) and (2.15) gives $\alpha(\sigma_e) = 3\dot{\varepsilon}_0 f(\sigma_e/\sigma_0)/(2\sigma_e)$, and the general 3D constitutive equation is

$$\frac{d_{ij}^{C}}{\dot{\varepsilon}_0} = \frac{3}{2}\frac{s_{ij}}{\sigma_e} f\left(\frac{\sigma_e}{\sigma_0}\right). \tag{2.16}$$

Define the effective creep strain rate as $d_e^C = \left(2d_{ij}^C d_{ij}^C/3\right)^{1/2}$. This definition, in combination with (2.12), (2.13) and (2.16), gives that $d_e^C/\dot{\varepsilon}_0 = f(\sigma_e/\sigma_0)$. Thus, the function relates the effective creep strain rate to the effective stress.

2.3 Scaling and limiting cases

This theory has a characteristic length, as can be seen through a scaling analysis. Inserting the creep model (2.16) and the creep strain rate expression (2.7) into the force balance (2.8), we obtain

$$\left[\frac{1}{3}\frac{\sigma_e}{\dot{\varepsilon}_0 f(\sigma_e/\sigma_0)}\left(v_{i,j} + v_{j,i} - \frac{2}{3}v_{k,k}\delta_{ij}\right)\right]_{,j} + (\sigma_m)_{,i} = 0. \tag{2.17}$$

Inserting the diffusion law (2.11) into the kinematic constraint (2.4), we obtain

$$v_{k,k} = -\left\{\frac{D}{kT}\left[F_k + (\Omega\sigma_m)_{,k}\right]\right\}_{,k}. \tag{2.18}$$

As mentioned above, the effective stress σ_e is related to the effective strain rate d_e^C through the function *f*. The effective strain rate is defined as $d_e^C = \left(2d_{ij}^C d_{ij}^C / 3\right)^{1/2}$, and the creep strain rate tensor d_{ij}^C is related to the velocity field by (2.7). Consequently, (2.17) and (2.18) consist of four partial differential equations that govern the four fields v_1, v_2, v_3 and σ_m. Under the special condition that the diffusion flux is divergence-free, $J_{k,k} = 0$ and $v_{k,k} = 0$, (2.17) recovers Stokes's equation for creep, and (2.18) recovers Herring's equation for self-diffusion.

Let Λ be the length to be determined. Scale the stress by σ_0, the marker velocities by $\Lambda\dot{\varepsilon}_0$, the wind forces by $\Omega\sigma_0/\Lambda$, and the spatial coordinates by Λ. Equations (2.17) and (2.18) become dimensionless and parameter-free provided we set

$$\Lambda = \sqrt{\frac{D\Omega\sigma_0}{kT\dot{\varepsilon}_0}}\,. \tag{2.19}$$

This length characterizes the relative rate of creep and diffusion. Let H be a length scale in the boundary-value problem, e.g., the height of a solder bump. Large values of Λ/H indicate that the time necessary for diffusion across the material is fast relative to the time necessary for creep.

We now wish to investigate how Λ/H affects the steady-state stress field in a solder bump. Since the electron wind force is roughly constant through the thickness of the solder, it alone does not result in a divergence in diffusion flux. However, different materials contact the solder at its boundaries, and atoms diffuse at different rates on each side of the boundary. For instance, the diffusivity of Sn in Sn is much faster than that of Sn in Cu. This results in a divergence in the diffusion

flux of Sn at the boundary between Sn and Cu. For a steady state to be reached, a stress gradient must be built up to counteract this divergence in diffusion flux. The length over which this stress gradient will be built up depends on the ratio Λ / H.

In one limit, $\Lambda / H >> 1$, diffusion is so much faster than creep that the effect of creep can be neglected. In this limit, the theory outlined in Section 2.2 will reduce to the analysis of Blech and Herring.[2] For a steady state to be reached, the diffusion flux must vanish, $J_i = 0$. For a 1D wind force in the x_3 direction, Equation (2.11) then gives $F_3 + \Omega(d\sigma_m / dx_3) = 0$ in the steady state. The stress gradient is a constant governed by the boundary conditions and is built up through the entire thickness of the solder.

In the other limit, $\Lambda / H << 1$, creep is extremely fast relative to diffusion. Since creep tends to relax stress, in this limit it seems that the stress may be zero everywhere in the solder. However, as previously mentioned, there is a flux divergence at the boundary. To satisfy this boundary condition, a stress gradient must be built up to offset this flux divergence. Since the characteristic length Λ is small relative to the size H of the boundary value problem, this stress will be localized near the boundary of the solder, as illustrated in Figure 2.3.

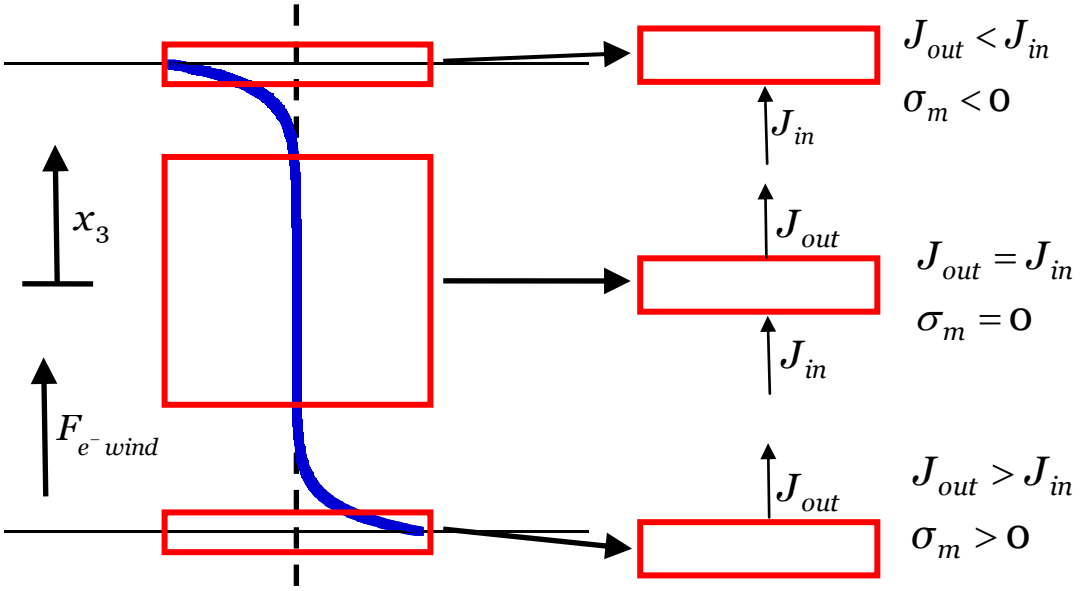

Figure 2.3. Solder bump with stress distribution for a rapidly creeping material. The horizontal axis is the stress level and the vertical axis is the position through the thickness of the solder bump. The blue line shows the stress distribution through the thickness of the solder $\sigma_m(x_3)$. The black, dotted line indicates zero stress; to the left of this curve the material is in compression and to the right of the curve the material is in tension. Stress is nearly zero everywhere but deviates from zero near the boundaries to counteract the flux divergence there. The flux divergence is illustrated in the red boxes, which represent differential volume elements at three locations through the thickness.

2.4 Stress in a thin film

To see how the physical ideas developed in Section 2.3 arise mathematically, let us consider a thin film of a solder material sandwiched between two other materials, as illustrated in Figure 2.4. Let us also assume the material under uniaxial tension obeys power-law creep $\dot{\varepsilon} = \dot{\varepsilon}_0 (\sigma / \sigma_0)^n$. An electron wind force will cause atoms to diffuse in the direction of the wind force, creating a state of compression near the anode and tension near the cathode. This stress state is biaxial with $\sigma_{11} = \sigma_{22}$, and the equivalent stress is $\sigma_e = |\sigma_{11}|$.

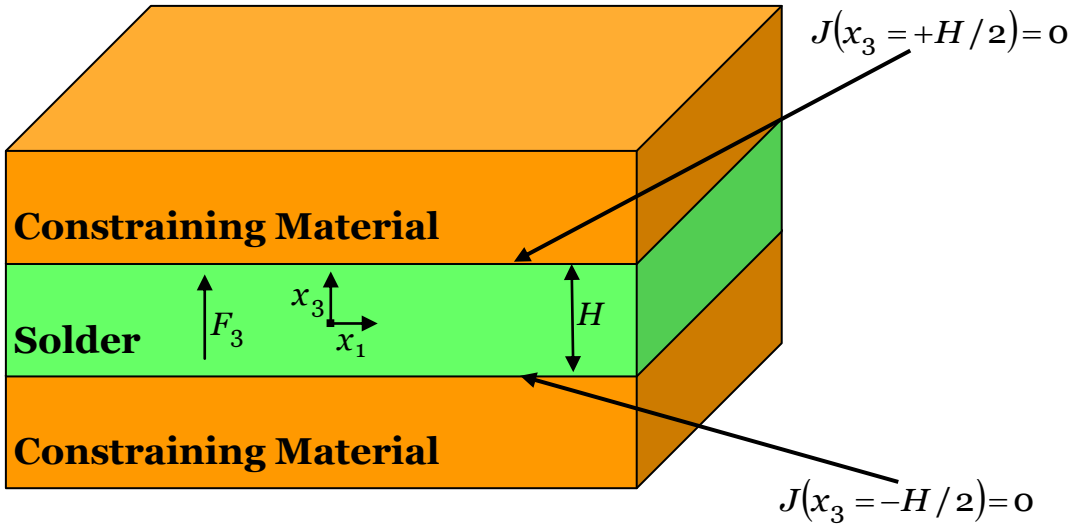

Figure 2.4. A thin film of a solder material, height H, is subject to a through-thickness electron wind force, F_2. The film is sandwiched between two materials that constrain it. Atoms do not diffuse into the two surrounding materials, so that there is no diffusion flux into or out of the solder. As atoms migrate through the solder, they create a state of compression near the upper boundary and tension near the lower boundary.

Equation (2.11) gives the diffusion flux as $J_3 = (D/\Omega kT)(F_3 + [2\Omega/3]d\sigma_{11}/dx_3)$. This diffusion flux induces a strain rate $d_{11}^{\ D} = -(\Omega/3)dJ_3/dx_3$. The bounding materials above and below the film constrain it from deforming laterally, so that the total strain rates vanish in the lateral directions: $d_{11} = 0$. Scaling the stresses by σ_0 and the spatial coordinates by the thickness H, we obtain

$$-\frac{4}{9}\left(\frac{\Lambda}{H}\right)^2 \frac{d^2\tilde{\sigma}_{11}}{d\tilde{x}_3^{\ 2}} + \tilde{\sigma}_{11}^{\ n} = 0, \qquad (2.20)$$

where Λ is the characteristic length given in Equation (2.19) and the tildes represent non-dimensional quantities. We have dropped the absolute value by examining this expression on the domain $-1/2 \le \tilde{x}_3 \le 0$ where the material is under tension.

The boundary conditions are such that atoms do not diffuse out of the solder and into the bounding materials. Thus, the diffusion flux vanishes at the faces of the film, or

$$\frac{d\tilde{\sigma}_{11}\left(\tilde{x}_3 = \pm 1/2\right)}{d\tilde{x}_3} = -\frac{3F_3 H}{2\Omega\sigma_0} \ . \tag{2.21}$$

From Equation (2.20), two clear limits exist. For $\Lambda/H >> 1$, the second term is negligible, and the stress field will be linear in $\tilde{x}_3$, namely $\tilde{\sigma}_{11}\left(\tilde{x}_3\right) = -\left[3F_3 H/(2\Omega\sigma_0)\right]\tilde{x}_3$. This limit is consistent with the seminal analysis of Blech in which the stress is distributed linearly along the length of the material.[4]

For $\Lambda/H << 1$, it seems tempting to entirely drop the first term in Equation (2.20). However, this would result in $\tilde{\sigma}_{11} = 0$ everywhere and would not satisfy the boundary conditions (2.21). Instead, we have a boundary-layer effect in which the stress in nearly zero everywhere through the thickness of the film but deviates rapidly from zero near the boundaries to satisfy the boundary conditions. In Equation (2.20), let $u = \dfrac{d\tilde{\sigma}_{11}}{d\tilde{x}_3}$ so that

$$-\frac{4}{9}\left(\frac{\Lambda}{H}\right)^2 \frac{du}{d\tilde{x}_3} + \tilde{\sigma}_{11}{}^n = -\frac{4}{9}\left(\frac{\Lambda}{H}\right)^2 \frac{du}{d\tilde{\sigma}_{11}}\frac{d\tilde{\sigma}_{11}}{d\tilde{x}_3} + \tilde{\sigma}_{11}{}^n = -\frac{4}{9}\left(\frac{\Lambda}{H}\right)^2 \frac{du}{d\tilde{\sigma}_{11}} u + \tilde{\sigma}_{11}{}^n = 0 \ .$$

Separating the variables and integrating results in $\left(\dfrac{d\tilde{\sigma}_{11}}{d\tilde{x}_3}\right)^2 = \dfrac{9}{2(n+1)(\Lambda/H)^2}\tilde{\sigma}_{11}{}^{n+1} + C$, where C is an integration constant. As previously argued, for $\Lambda/H << 1$, the stress is essentially zero over most of the domain. Thus, $\tilde{\sigma}_{11}\left(\tilde{x}_3 = 0\right) \approx 0$ and $d\tilde{\sigma}_{11}/d\tilde{x}_3\left(\tilde{x}_3 = 0\right) \approx 0$ so that $C \approx 0$. We now have

$$\left(\frac{d\tilde{\sigma}_{11}}{d\tilde{x}_3}\right)^2 = \frac{9}{2(n+1)(\Lambda/H)^2}\tilde{\sigma}_{11}^{\,n+1}. \qquad (2.22)$$

The maximum tensile stress will be located at the boundary, $\tilde{x}_3 = -1/2$. Substituting the boundary condition (2.21) into (2.22) gives:

$$\tilde{\sigma}_{\max} = \left[\frac{\sqrt{n+1}F_3}{\sqrt{2}\Omega\sigma_0}\Lambda\right]^{2/(n+1)}. \qquad (2.23)$$

Hence, for a power-law creep material with $\Lambda/H << 1$, the maximum stress in the film scales as $\Lambda^{2/(n+1)}$ and is independent of the thickness H.

To get a better sense of how stress varies through the thickness, Equation (2.20) subject to the boundary conditions (2.21) was solved using the finite-element software COMSOL Multiphysics. In this software, the 1D General Form in the PDE Modes was selected to perform the analysis. We have used $n = 3$ and $F_3 H/\Omega\sigma_0 = 86.9$, which are representative values for a SnAgCu solder during operation (with $j = 10^8\ A/m^2$, $T = 100\ ^\circ C$, $H = 50\ \mu m$).[28] The stress distribution through the film thickness is plotted in Figure 2.5 as a function of Λ/H. The stress is zero at the middle of the film, is tensile on one side, and is compressive on the other. We can clearly see a transition from the boundary layer regime to the Blech regime (linear stress distribution) as Λ/H increases. Also from Figure 2.5, we observe that a large Λ/H, or fast diffusion relative to creep, results in a relatively large stress. Likewise, slow diffusion relative to creep results in a relatively small stress. We can interpret this observation in the following way: if atomic diffusion is fast relative to creep, a large stress is built up before it can be relaxed by deformation (creep). Conversely, if creep is fast relative to diffusion, the material is

liquid-like and can deform very rapidly to prevent large stress build-up.

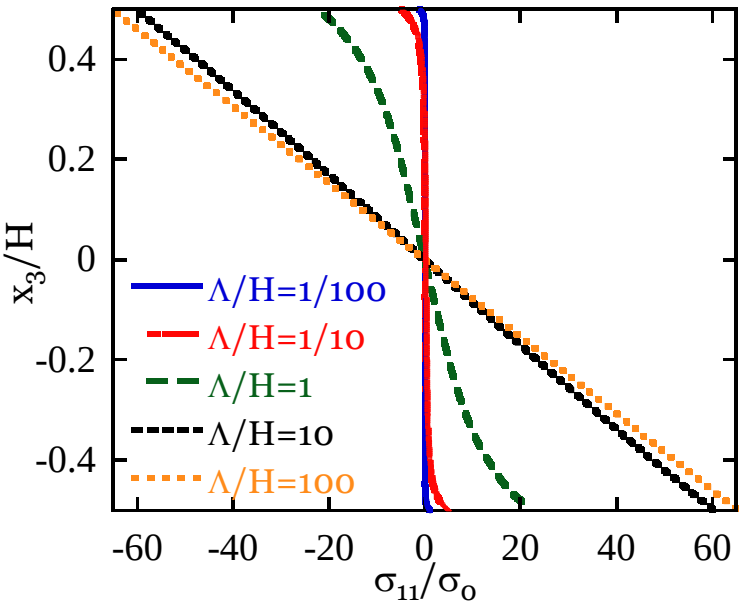

Figure 2.5. Stress distribution through the film thickness as a function of characteristic length Λ for a material with power law creep. The stress distribution changes from a boundary layer-type distribution to a linear one as Λ/H increases. Also, the maximum stress increases as Λ/H increases.

2.5 Void formation in solder bumps

It is commonly suggested that voids are formed in the solder by supersaturation of vacancies at the cathode.[4] The idea is that atoms diffuse by a vacancy mechanism in the direction of the electron flow; hence, vacancies migrate in the direction opposite to atomic diffusion. When enough vacancies accumulate near the cathode, they can condense to form a void, as shown in Figure 2.2a. The void can grow as additional vacancies are supplied to it. Once the voids propagate across the length of the contact, the bump fails. This physical picture is adopted by most researchers in the area.

The above picture, however, is inconsistent with the following consideration. A solder bump has numerous sources and sinks of vacancies spread throughout it, such as grain boundaries and dislocations. As noted by Balluffi, these sources and sinks tend to keep vacancy concentrations at equilibrium levels, as illustrated in Figure 2.2b.[35] Hence, vacancy supersaturation is unlikely. Instead, we adopt an alternative physical picture for the formation of voids. In our picture, conduction electrons motivate atoms in the solder to diffuse, which can result in flux divergence. Under constraint, this flux divergence creates stress in the solder. Stress acts on the initial flaws in the material that were created during the manufacturing process. According to the Laplace equation, these flaws will grow provided:

$$\sigma > \frac{2\gamma}{a}, \tag{2.24}$$

where γ is the surface tension and a is the initial flaw radius, as in Figure 2.6. We assume that the material will fail (have a big change in resistance) when these initial flaws grow. Conversely, the material will be immortal as long as the stress everywhere in the material is less than the critical stress, $\sigma_c = 2\gamma / a$. A similar physical picture has long been used in analyzing the formation of voids during tensile creep, or the removal of pores during sintering.[40]

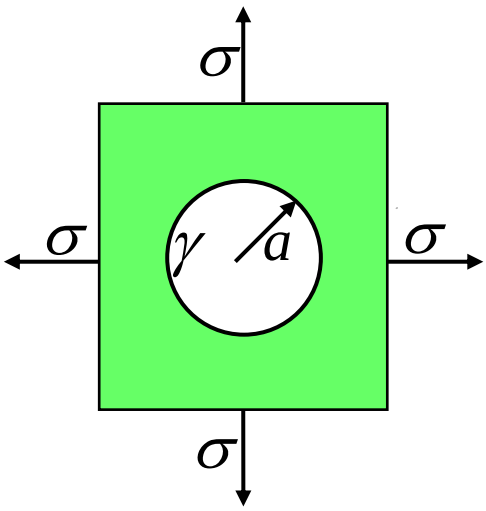

Figure 2.6. For voids to grow we have the condition $\sigma > 2\gamma/a$, where γ is the surface tension and a is the initial flaw radius.

2.6 Analysis using Pb-free solder data

We now desire to perform a similar analysis of an actual solder system. Under a uniaxial tensile test, a double power law form commonly is found to represent the creep behavior in a solder. For instance, Wiese gives the relation for SnAg4Cu0.5 as

$$\dot{\varepsilon} = A_1 D_1 \left(\frac{\sigma}{\sigma_0}\right)^3 + A_2 D_2 \left(\frac{\sigma}{\sigma_0}\right)^{12}, \qquad (2.25)$$

where $\dot{\varepsilon}$ is the creep rate in the loading direction, $\sigma_0 = 1\,\text{MPa}$ is a reference stress, $A_1 = 4\times10^{-7}/\text{sec}$, $A_2 = 1\times10^{-12}/\text{sec}$, D_1=exp(-3223/T), and D_2=exp(-7348/T).[41] The first term on the right hand side of (2.25) corresponds to the creep behavior in the low-stress regime, where dislocation climb processes dominate the deformation behavior.[41] The second term corresponds to the creep behavior in the high-stress regime, where combined glide/climb processes dominate.[41] Other parameters needed for the simulation include: $Z = 18$,[28] $e = 1.602\times10^{-19}\,\text{C}$,

$\rho_{100^\circ C} = 1.48\times10^{-7}$ Ohm-m ,[42] $\Omega_{Sn} = 2.705\times10^{-29}\ m^3$, and $D = 1.07\times10^{-3}\exp(-105{,}000/RT)\ (m^2/s)$.[43] It is worthwhile to note that the diffusivity given is the self-diffusivity of Sn. This value was used because the solder bumps of interest are composed of primarily Sn and because Sn is the dominate diffusing species in an important mode of electromigration failure.[44] Also, the diffusivity used in the simulation is for diffusion along the a-axis (body-centered tetragonal crystal structure). The diffusivity along the c-axis is comparable, with an activation energy of $107\ kJ/mol$.[43]

With these data, the characteristic length Λ is plotted as a function of temperature in Figure 2.7. From this figure, we see that for the above data, the characteristic length Λ increases as the temperature increases. This occurs because the diffusivity increases more rapidly with temperature than the creep rate does. Also, in the plotted temperature range, the characteristic length is in the micron scale, which is roughly comparable to the size of a typical solder bump ($\sim 50\ \mu m$).

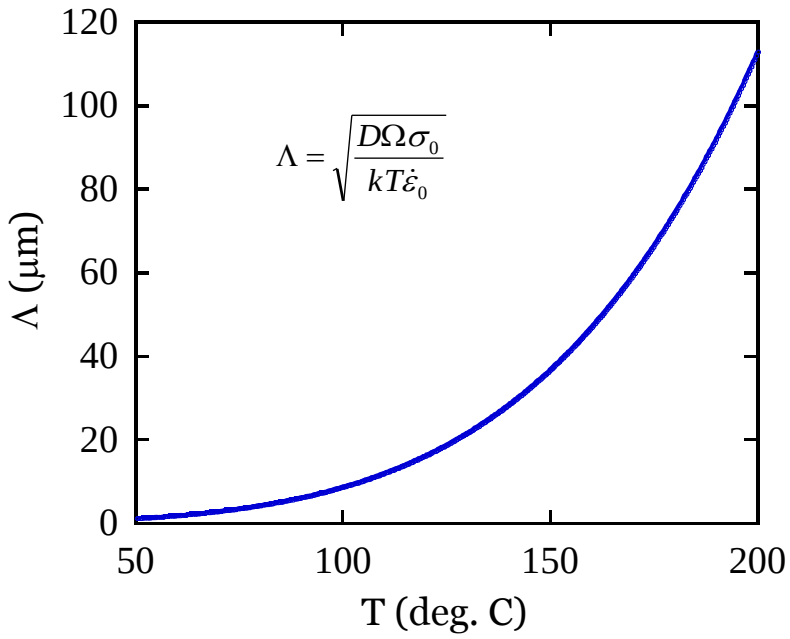

Figure 2.7. Characteristic length as a function of temperature. For SnAg4Cu0.5 with constitutive law (2.25), Λ increases with T, meaning diffusion increases more rapidly than creep does as the temperature increases.

For the constitutive law (2.25), the governing ODE is

$$-\frac{2D\Omega}{9kT}\frac{d^2\sigma_{11}}{dx_3^{\,2}}+\frac{\sigma_{11}}{2\sigma_0}\left[A_1D_1\left(\frac{|\sigma_{11}|}{\sigma_0}\right)^2+A_2D_2\left(\frac{|\sigma_{11}|}{\sigma_0}\right)^{11}\right]=0\,. \tag{2.26}$$

The boundary conditions are

$$\frac{d\sigma_{11}(x_3=\pm H/2)}{dx_3}=-\frac{3F_3}{2\Omega}\,. \tag{2.27}$$

As mentioned in Section 2.5, we hypothesize that a critical stress exists above which voids will grow. This critical stress is given by the Laplace equation: $\sigma_c=2\gamma/a$. For Sn, $\gamma\approx 0.5$ N/m [45] and assuming that the initial flaw has a radius of 100 nm, a representative value for this critical stress is $\sigma_{critical}\approx 10$ MPa. It should be noted that this is a simple model to estimate the critical stress. Alternatively, the creep strengths of the material may be used if these data are

available. For instance, the creep strength of a SnAg3.5 solder at 100°C is about 5 MPa.[28] This value is comparable to the value estimated from the Laplace equation. The main point for the purposes of this chapter is that a critical stress exists and is a constant on the order of 10 MPa. This critical stress depends on material properties of the solder and on the manufacturing process.

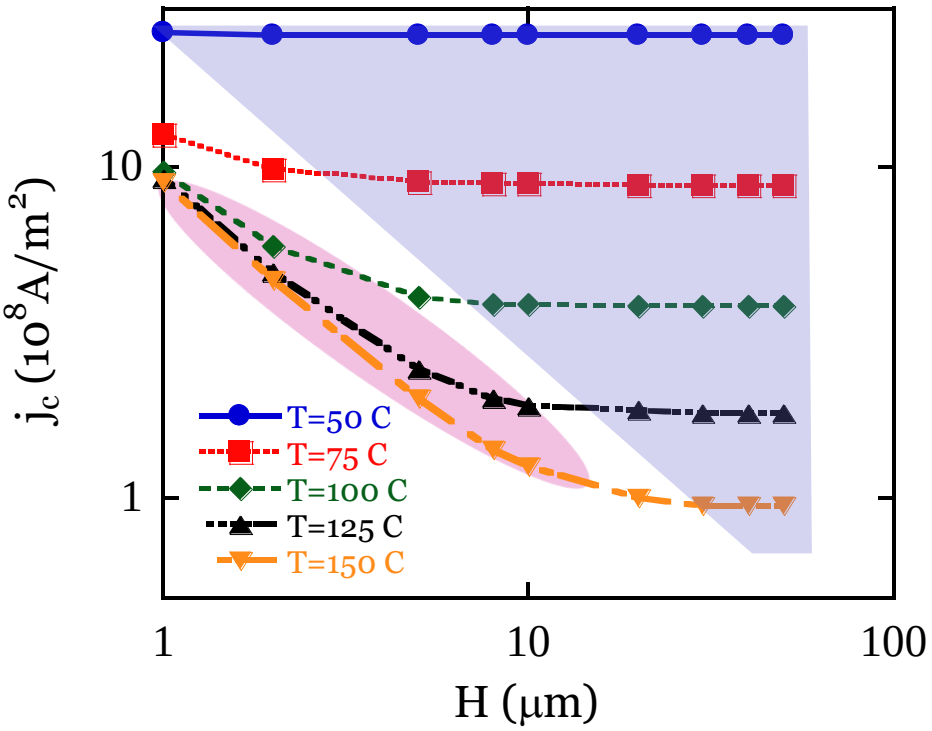

Figure 2.8. Critical current density as a function of thickness and temperature for SnAg4Cu0.5. The pink region indicates the Blech regime, and the light blue region represents the boundary-layer regime.

We would like to calculate the current density necessary to reach this critical stress. For each film thickness and temperature, the current density (from $F_i = Ze\rho j_i$) was varied in COMSOL until a maximum stress of $\sigma_{\max} = \sigma_c = 10$ MPa was achieved, and this current density was recorded as the critical current density j_c. The critical current density as a function of thickness and temperature is plotted in Figure 2.8. From this figure, for a given thickness, the critical current density

decreases as the temperature increases. The explanation for this observation can be ascertained by examining Figure 2.7; the characteristic length Λ increases as the temperature increases. As previously discussed, for a given current density, an increase in Λ results in an increase in $\sigma_{\max}$. A larger maximum stress for each current density means it requires a smaller current density to reach σ_c. Thus, the critical current density will decrease as temperature increases.

It is also interesting to note the functional form of $j_c(T)$ when $\Lambda/H \ll 1$. Although SnAg4Cu0.5 in general obeys a double power law relation given by Equation (2.25), for the stress levels and temperatures of interest, the first term usually is much larger than the second. Thus, it can be approximated by single power-law creep, as analyzed in Section 2.4, and we can rewrite Equation (2.23) as

$$\sigma_c = \left[\frac{\sqrt{n+1}(Ze\rho j_c)}{\sqrt{2}\Omega\sigma_0}\right]^{2/(n+1)} \Lambda^{2/(n+1)}, \tag{2.28}$$

and therefore

$$j_c \propto 1/\Lambda. \tag{2.29}$$

Also, since Λ is given by $\Lambda = \sqrt{\frac{D\Omega\sigma_0}{kT\dot{\varepsilon}_0}} = \sqrt{\frac{\Omega}{kT} D_0 \exp\left(-\frac{Q_D}{kT}\right) C_0 \exp\left(\frac{Q_c}{kT}\right)}$, one obtains $j_c \propto \sqrt{kT}\exp\left(\frac{Q_D - Q_C}{2kT}\right)$. We can further simplify this relationship by noticing that the square root term is quite weak. For instance, for an increase from $100\,^{\circ}C$ to $200\,^{\circ}C$, j_c will increase only by 13% due to the contribution from the $\sqrt{kT}$ term. The dependence on the exponential term is much stronger. Thus, we approximately have

$$j_c \propto \exp\left(\frac{Q_D - Q_C}{2kT}\right). \tag{2.30}$$

Therefore, in the boundary layer regime, we expect an exponential dependence of the critical current density on temperature. Such a dependence cannot easily be explained in terms of Blech's analysis. In his analysis, he attributed this dependence to the increase in flow stress, i.e. a change in the maximum compressive/tensile stresses the material can withstand. Albeit a possible explanation, our theory has a more straightforward explanation, as given in the derivation above. Specifically, for a material in the boundary layer regime, the critical current density scales with the reciprocal of the characteristic length, $j_c \propto 1/\Lambda$. The characteristic length depends on the diffusivity and creep law of the material, which exhibit Arrhenius-type relations. Consequently, the critical current density scales exponentially with temperature, as given in Equation (2.30).

The critical product $j_c H$ as recognized by Blech is plotted as a function of the thickness H in Figure 2.9. In his analysis, Blech claims this product should be a constant above which electromigration damage will occur.[2] The product should be independent of the size. This figure demonstrates that for a given temperature, there is a transition from the Blech regime to the boundary-layer regime as the film thickness increases. Specifically, between 100-150°C, using experimentally determined solder properties, this transition occurs between 1-10 μm. This means that according to the data and the simulation, a solder larger than 10 μm is actually in the boundary layer regime during operation. Thus, it appears that this boundary layer effect may be important in proper analysis of the stress distribution in Pb-free

solder bumps.

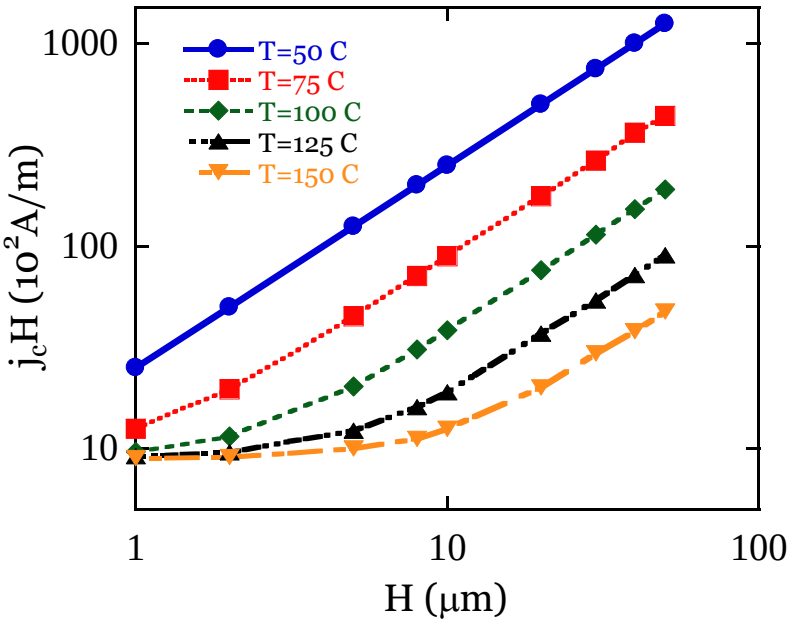

Figure 2.9. Critical product as a function of film thickness and temperature.

2.7 Comparison with experimental results

Comparison with experiments is difficult due to the lack of data for critical current densities in actual solder bumps. However, we can still make some comparisons to solder materials with slightly different geometries. For instance, Hsu et al measured the critical current density as a function of temperature for 350 μm long Blech-type SnAg3.8Cu0.7 solder stripes.[46] This material is in the boundary layer regime for the testing conditions so we expect $\ln(j_c) \propto 1/T$ as given in Equation (2.30). A comparison of the simulated results (for a 350 μm SnAg3.8Cu0.7 solder stripe) and the experimental data is given in Figure 2.10. The apparent activation energy, Q, found from the simulation is 0.385 eV. The experimental data also shows an exponential dependence with Q = 0.333 eV,

comparable to the predicted value.

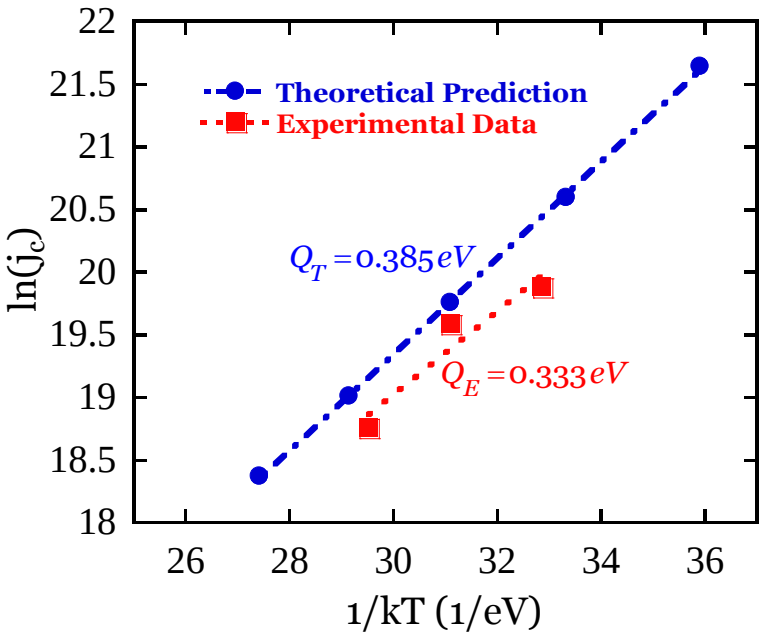

Figure 2.10. Critical current density as a function of temperature. The experimental data is for a 350 μm SnAg3.8Cu0.7 solder stripe.

As another example, Yoon et al examined the dependence of the threshold current density on line length.[47] In these experiments, five SnPb solder lines were tested with lengths ranging between 100 and 1000 μm at a temperature of 140˚C. Their experiments found that the critical current density is a constant independent of line length. Using the creep and law and diffusivity from Siewert et al, the characteristic length of SnPb is found to be $\Lambda = 0.199$ μm at 140˚C .[28] Thus, $\Lambda / H << 1$ for these experiments and we predict the SnPb solder to be well within the boundary layer regime. As was suggested in Section 2.4, for a solder in the boundary layer regime, we predict the critical current density to be independent of size, as was found in the experiments.

2.8 3D solder versus thin film

In the previous sections, we have approximated the solder bump as a thin film. Initially, we desired to solve the full set of 3D governing equations, (2.17) and (2.18), using the finite element software COMSOL Multiphysics. However, it was found that the creep law for the solder is highly nonlinear, leading to some convergence and/or memory problems. We then realized that we should be able to approximate the solder bump as a thin film, making the problem 1D. A 1D problem has a drastically reduced number of degrees of freedom, which allowed for a much finer mesh and ultimately for convergence in COMSOL.

However, we need to justify this approximation of the solder bump being represented as a thin film. To do so, we implemented Equations (2.17) and (2.18) in COMSOL using the general form of the PDE modes module. However, the constitutive law used was a linear relation, namely $d_{ij}^{C} = s_{ij}/2\eta$, where η is the viscosity of the material. This linear problem is much easier to solve with the finite element software. The boundary conditions used are no flux through any surfaces, traction-free lateral surfaces, and no marker velocity on the upper and lower boundaries:

$$\begin{array}{ll} J_i n_i = 0 & \text{all surfaces} \\ t_i = \sigma_{ij} n_j = 0 & \text{lateral surfaces} \\ v_i = 0 & \text{top/bottom surfaces} \end{array} \qquad (2.31)$$

Typical stress distributions resulting from the simulation are shown in Figure 2.11.

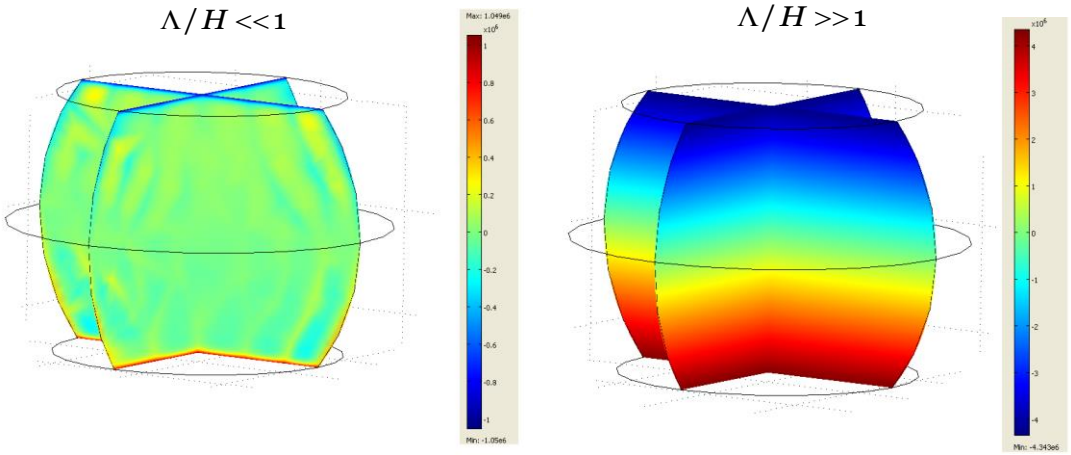

Figure 2.11. Typical stress distributions for linear creep using the 3D model in COMSOL.

Physically, differences between the 3D model and the thin film one will arise due to stress relaxation via creep on the lateral surfaces of the 3D model. Such relaxation cannot occur in the 1D model since the material is constrained from deforming laterally. However, for $\Lambda/H << 1$, we expect the stress to be confined to thin layers near the upper and lower boundaries. Since we also have a no marker velocity boundary condition at these boundaries, in these layers we roughly have no lateral deformation. Thus, in the region where stress exists, the material is constrained laterally, suggesting that the thin film approximation is appropriate. Likewise, for $\Lambda/H >> 1$, creep is very slow compared to diffusion. Thus, stress relaxation via creep is negligible, and the thin film approximation seems valid. The comparisons given in Figure 2.12 confirm these ideas. From this figure, we can see that in these two limiting cases, $\Lambda/H << 1$ and $\Lambda/H >> 1$, the 3D and 1D simulations agree quite well. Thus, these physical justifications and simulations suggest that the approximation of the solder bump as a thin film is valid for the two

limiting cases, $\Lambda/H << 1$ and $\Lambda/H >> 1$.

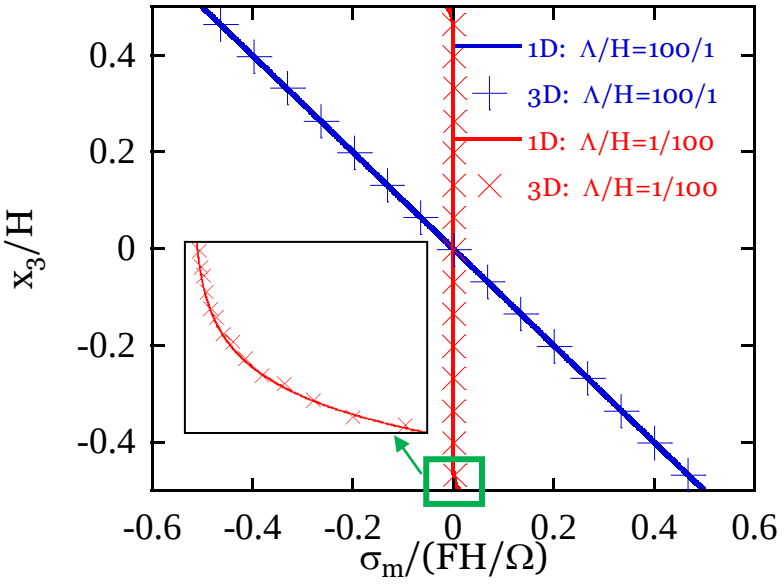

Figure 2.12. Comparison of stress in 3D and 1D simulations plotted through the thickness. A close up view of the green boxed region is given in the bottom left corner of the plot.

2.9 Summary

To determine the stress field in a solder bump, we have presented a theory that couples creep and electromigration. This theory results in governing equations (2.17) and (2.18), a set of coupled PDE's that allow for the calculation of the stress and deformation fields. From these equations, an intrinsic length emerges, (2.19), which characterizes the relative rates of creep and diffusion. When diffusion is slow relative to creep, we find the stress is relatively small and localized to the boundary of the solder. We suggest that when stress exceeds a threshold value, voids will form in the solder. Using Pb-free solder data, we discover that the effects of creep are significant and must be taken into account for proper analysis of

electromigration-induced failure in solder bumps. Comparisons with experiments demonstrate general agreement with the theory. To further augment the content of this theory, we need more experimental data on electromigration failure in Pb-free solders. Specifically, it would be useful to have a systematic study measuring critical current density for various solder sizes and operating temperatures.

Chapter 3

Fracture of Electrodes Caused by Fast Charging

3.1 Introduction

Batteries are key in the commercialization of clean and secure energy.[1],[48] Essential roles of batteries include leveling loads on power grids and storing energy from renewable sources. Furthermore, batteries are ubiquitous in all forms of electronics and transportation. For applications sensitive to weight and size, such as portable electronics and electric cars, the technology of choice is lithium-ion batteries.[49]

A lithium-ion battery contains an electrolyte and two electrodes. Each electrode is an atomic framework that hosts mobile lithium. During charging or discharging of the battery, lithium ions are extracted from one electrode, migrate through the electrolyte, and are then inserted into the other electrode. Meanwhile electrons flow from one electrode to the other through an external metallic wire. Extraction or insertion of lithium induces stresses in the electrodes that may cause fracture[50] or morphological change.[16] The loss of structural integrity may reduce electric conductance, causing the capacity of the battery to fade.

Lithiation-induced damage is a bottleneck in developing batteries of high energy density. For example, the ability of silicon to absorb a large amount of lithium has motivated intense research,[51] but such absorption causes volumetric

swelling of ~400%, leading to fracture. The mechanical failure has so far prevented silicon from serving as a viable electrode. Fracture has also been observed in commercial electrodes that undergo small deformation, such as $LiCoO_2$, $LiMn_2O_4$ and $LiFePO_4$.[52]-[55]

Lithiation-induced deformation and stress have been studied in recent years. For example, Christensen and Newman calculated swelling and stress,[56], [57] Sastry and co-workers simulated the stress generation during lithiation under galvanostatic control,[58] and Cheng and co-workers calculated the strain energy under both potentiostatic and galvanostatic operations in spherical particles.[59],[60] Lithiation-induced stress in silicon has been calculated.[61], [62] Several recent papers have studied lithiation-induced fracture by applying fracture mechanics.[11], [66],[69]

While a conceptual framework to analyze lithiation-induced deformation, stress and fracture is emerging, limited work has been published that predicts fracture of practical systems by using actual material data. This chapter attempts to predict fracture in a widely used material for cathode, $LiCoO_2$. A commercial electrode often takes the form of active particles embedded in a binding matrix (Figure 3.1). The distribution of lithium in the particle is inhomogeneous. The gradient of this inhomogeneity is large if the battery is charged at a rate faster than lithium can homogenize in the particle by diffusion. We calculate the distributions of lithium and stress in a $LiCoO_2$ particle, and then calculate the energy release rates for the particle containing preexisting cracks. These calculations predict the critical rate of charging and size of the particle, below which fracture is averted.

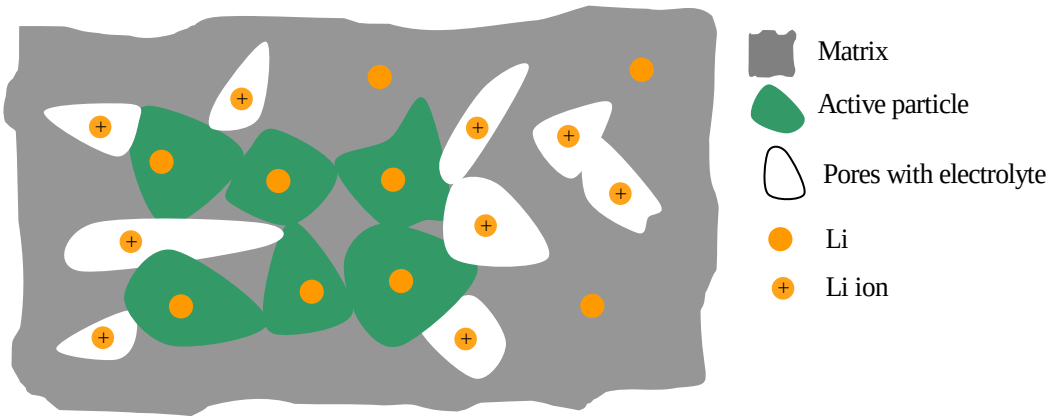

Figure 3.1. A schematic of the microstructure of the cathode. The cathode is composed of active particles, a matrix, and pores containing the electrolyte.

3.2 Theory and scaling

In a battery, the electrolyte conducts lithium ions but not electrons. When the battery discharges, the difference in the chemical potential of lithium in the two electrodes drives the ions to diffuse out of the anode, through the electrolyte, and into the cathode. To keep the electrodes electrically neutral, electrons flow from the anode to the cathode through the external metallic wire. Both the ionic and the electronic processes are reversed when the battery is charged by an external power source. As illustrated in Figure 3.1, an electrode in commercial Li-ion batteries is usually a composite, consisting of active particles, a matrix composed of polymer binders and additives, and pores filled with the electrolyte.[55] Migration of lithium in the electrolyte is fast, so that diffusion of lithium in the active particles limits the rate of charging and discharging. Because of the porosity of the composite and the compliance of the binder, stress in an active particle is often due primarily to the mismatch created by an inhomogeneous distribution of lithium within the particle.

The degree of the inhomogeneity depends on the competition between the

rate of discharging and the rate of diffusion. Denote τ as the time to discharge the battery, D a representative value of diffusivity of lithium in the particle, and L the characteristic size of the particle. These quantities form a dimensionless group:

$$\chi = \frac{L}{\sqrt{D\tau}} \tag{3.1}$$

The parameter χ measures the relative rate of discharging and diffusion. If χ is large, the battery is discharged at a rate faster than lithium can homogenize in the particle by diffusion. Consequently, lithium is crowded in the outer shell of the particle, causing a large stress in the particle (Figure 3.2a). By contrast, if χ is small, the battery is discharged at a rate slow enough for lithium in the particle to maintain nearly a homogeneous distribution. Consequently, lithiation causes the particle to swell or contract, but the particle is nearly unstressed (Figure 3.2b).

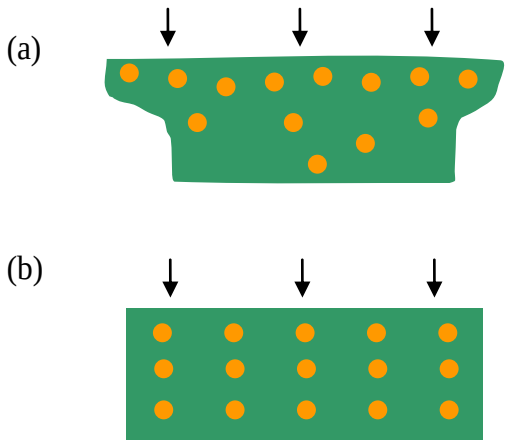

Figure 3.2. (a) When the rate of discharging is high, the distribution of lithium in the active particle is inhomogeneous, which causes a field of stress in the particle. (b) When the rate of discharging is low, the distribution of lithium in the particle is nearly homogenous, and the magnitude of the stress in the particle is negligible. The arrows indicate the direction of lithium insertion.

Crack-like flaws are assumed to preexist in the active particles.[55] We ask if the lithiation-induced stress will cause any of the flaws to grow. The elastic energy in

the particle reduces when a crack advances. The reduction of the elastic energy in the particle associated with the crack advancing a unit area defines the energy release rate, G. Dimensional considerations dictate that the energy release rate should take the form

$$G = ZE\varepsilon_m^2 L, \tag{3.2}$$

where E is Young's modulus of the particle, L a characteristic size of the particle, and ε_m a characteristic mismatch strain, defined as

$$\varepsilon_m = \frac{l_1 - l_0}{l_0} \tag{3.3}$$

Here, l_0 and l_1 are the lattice parameters in the initial state and in the fully lithiated state, respectively. At a given time, the distribution of the stress in the particle is determined by solving the diffusion equation, and the dimensionless coefficient Z is determined by solving the elastic boundary-value problem. Once the geometry of the particle and the location of the crack are given, Z can only vary with the length of the crack, the dimensionless parameter χ, and time. We note this functional dependence in a normalized form:

$$Z = f\left(\frac{a}{L}, \chi, \frac{t}{\tau}\right), \tag{3.4}$$

where a denotes the length of the crack. At a fixed value of χ and a fixed time, if the crack is very short, the elastic energy in the particle does not change appreciably when the crack grows, and the energy release rate is small. Likewise, when the crack is very long, the elastic energy is nearly fully relaxed because the crack introduces larger constraint-free area, and the energy release rate is also small. In between these

two limits, the energy release rate reaches the maximum value $G_{\max}$ for a crack of a certain length. Let Γ be the fracture energy of the particle. No preexisting flaws will advance if the maximum energy release rate is below the fracture energy of the particle

$$G_{\max} < \Gamma . \tag{3.5}$$

To ensure no preexisting flaws will advance, $G_{\max}$ indicates the energy release rate maximized for all configurations of the flaws and for all time. This approach has been used to analyze many systems, such as polycrystals,[70] composites,[71] and thin films.[72]

The comparison between the energy release rate and the fracture energy defines another dimensionless parameter

$$\Lambda = \frac{E\varepsilon_m^2 L}{\Gamma} . \tag{3.6}$$

When Λ is small, the elastic energy is insufficient to cause fracture. Therefore, a particle with small stiffness, small size, and large fracture energy is more resistant to fracture. This statement is consistent with recent experimental observation that the electrochemical cycling behavior is significantly improved if the size of active particles is small.[73], [74]

The dimensionless groups χ and Λ characterize the fracture behavior of the active particles. In the case of a highly inhomogeneous distribution of Li ions, to prevent fracture it is necessary to decrease the particle size, decrease the rate of discharging, and/or enhance the fracture energy. This concept is sketched schematically in Figure 3.3 in terms of χ and Λ. The red line delineates an upper

boundary to the safe regime in which no fracture occurs.

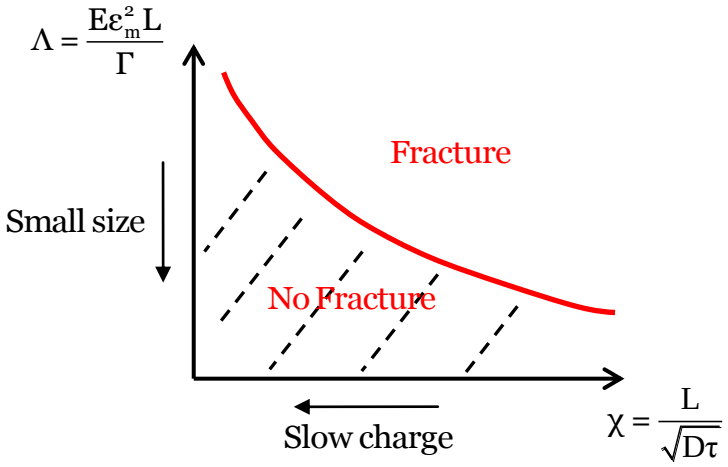

Figure 3.3. Criteria to avoid fracture of an electrode particle in terms of the non-dimensional quantities Λ and χ.

The concentration of lithium in the particle is a time-dependent field governed by the diffusion equation:

$$\frac{\partial c}{\partial t} = \nabla \cdot \left[D(c) \nabla c \right], \tag{3.7}$$

where c denotes the normalized lithium concentration in the host–the actual lithium concentration divided by the concentration of lithium in the fully lithiated state, $LiCoO_2$. In practical applications, the size of a $LiCoO_2$ electrode particle is on the order of microns or smaller. At such a small scale, the particle is often a single crystal or at most consists of a few grains.[13] Thus, the electrode is assumed to be a single crystal with a 2D geometry. Lithium ions only diffuse along the x axis. The model is shown in Figure 3.4c, in which L characterizes the particle size.

The stress field is calculated by solving an elastic boundary-value problem. Since elastic deformation is much faster than atomic diffusion, mechanical equilibrium is established during lithiation. Therefore, the governing equations are

taken from the theory of linear elasticity. As the particle is embedded in a porous and compliant matrix, traction-free boundary conditions are prescribed.

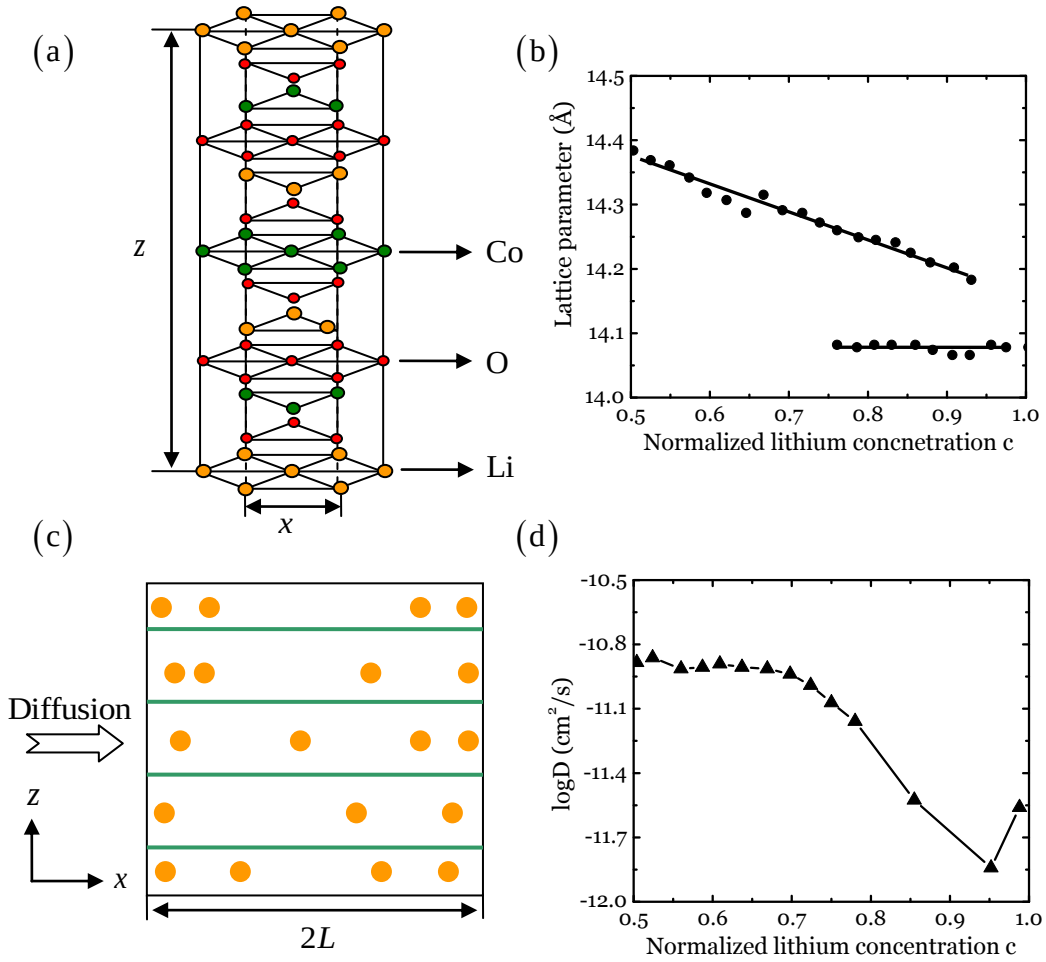

Figure 3.4. (a) The layered structure of $LiCoO_2$. (b) Variation of lattice parameter along the *z*-axis with normalized lithium concentration (Reproduced from reference [75]). The lattice parameter along the x-axis is nearly a constant. (c) 1D diffusion model used in the numerical simulations. Lithium diffusion is along the x-axis, towards the center of the particle. (d) The lithium diffusivity as a function of the normalized lithium concentration (Reproduced from reference [76]).

3.3 Numerical results for $LiCoO_2$

Following the above theory, we perform calculations for a $LiCoO_2$ particle. As illustrated in Figure 3.4a, $LiCoO_2$ has a layered crystalline structure, where oxygen ions form close-packed planes in an ABCABC sequence, and cobalt and lithium ions

occupy alternating layers of octahedral sites between the oxygen layers. The oxygen ions cause repulsion between the neighboring layers. These oxygen layers are attracted to the lithium ions inserted between them. Thus, during discharge the insertion of the lithium ions decreases the repulsion between the CoO_2 sheets and leads to a contraction.[75] The lattice parameter along the direction normal to the CoO_2 sheets is shown as a function of lithium concentration in Figure 3.4b. The insertion of lithium also causes strains in the other directions of the crystal but these strains are much smaller[75] and are hence neglected in the numerical simulations.

In practice, the working regime for lithium cobalt oxide is in the range of $0.5 \leq c \leq 1$. Experiments show that the diffusivity D decreases one order of magnitude when the normalized lithium concentration increases from 0.5 to 1.[76] Here, we reproduce the experimental diffusivity dependence on lithium concentration in Figure 3.4d. In the simulation we have allowed the diffusivity to vary with concentration, a dependence that is usually neglected in other works.

The initial and boundary conditions are given by

$$\begin{aligned} &t = 0; && c = 0.5 \\ &x = 0;\ t > 0 && \frac{\partial c}{\partial x} = 0 \\ &x = L;\ t > 0 && -D(c)\nabla c = \text{constant} \end{aligned} \tag{3.8}$$

The constant in Equation (3.8) is given by the discharge current density under galvanostatic (constant current) operation. Thus, in the simulation the discharge rate is controlled by changing the flux constant. Discharge is completed once the normalized concentration of lithium at the outside surface reaches a value of unity. The concentration profile of lithium inside the particle is obtained by solving the

diffusion equation in COMSOL Multiphysics.

Figure 3.5a and Figure 3.5b show the distributions of Li at several times, at discharge rates of 0.5C and 2C respectively. Here the discharge rates are reported in the C-rate convention given by C/τ, where the value of τ is calculated as the theoretical capacity (~140 mAh/g) divided by the discharge current. It is evident from the figures that, in both cases, the lithium concentration gradient increases with discharge time. This behavior is a direct consequence of the decrease in effective diffusivity with increasing lithium concentration (Figure 3.4d). As the discharge rate increases from 0.5C to of 2C, the lithium distribution inside the host particle becomes less homogeneous, in agreement with the schematics in Figure 3.2.

This inhomogeneous distribution of lithium results in a large deformation mismatch. The strain along *z* direction (Figure 3.4a) in the host particle is given by

$$\varepsilon = \frac{l(c) - l_o}{l_o} \tag{3.9}$$

where $l(c)$ is the lattice parameter at a given lithium concentration, l_o is the lattice parameter at the initial normalized Li concentration c = 0.5. Here we use the experimental values for the $LiCoO_2$ lattice parameter as a function of concentration to calculate the strain.[75] The inhomogeneous distribution of lithium leads to a non-uniform strain field inside the particle and thus a stress field in the particle.

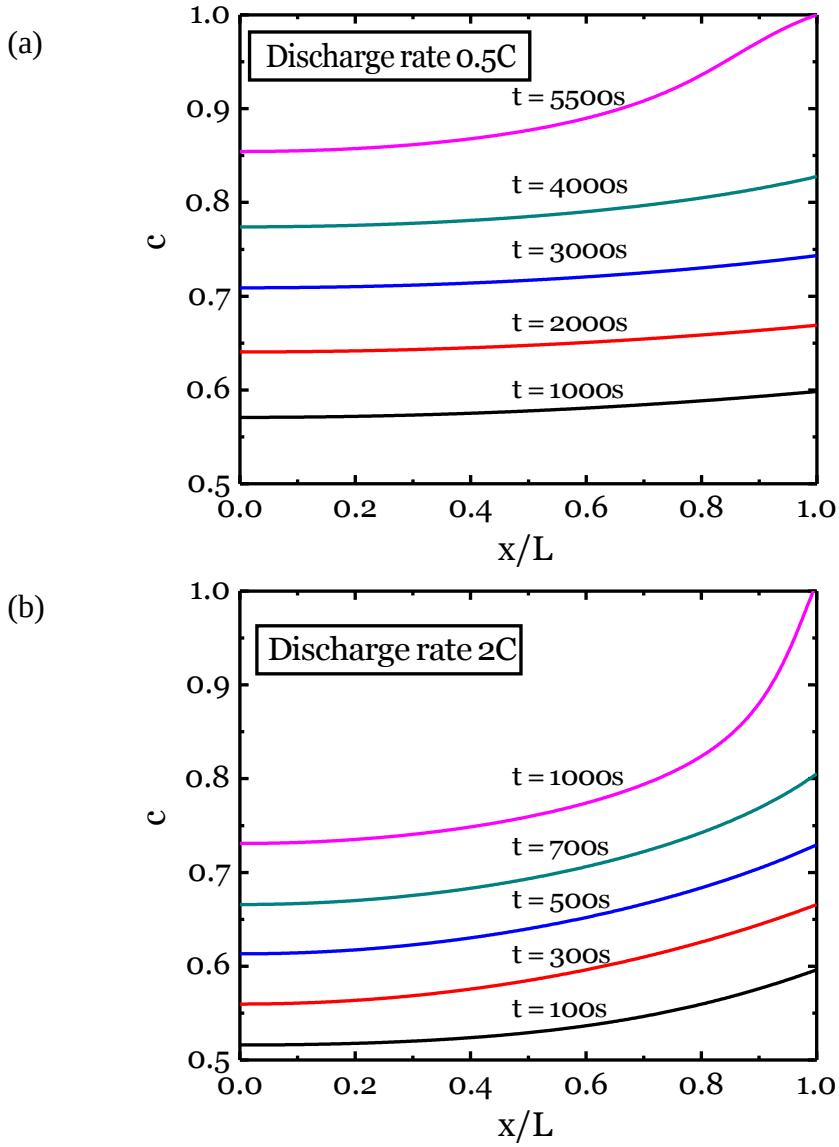

Figure 3.5. Lithium distribution with time for a $LiCoO_2$ particle at (a) discharge rate of 0.5C, (b) discharge rate of 2C. Here $x/L=0$ represents the center of the particle, and $x/L=1$ represents the outside surface.

The stress field is calculated by solving the elastic boundary value problem with the finite element software ABAQUS. An orthotropic material model is employed with stiffness coefficients taken from atomistic simulations.[77] The input strain field is simulated by imposing a thermal strain, equal to the concentration induced mismatch strain; the stress field is obtained as the output. In this

configuration, the stress component σ_{zz} is the tensile stress responsible for the crack propagation. Figure 3.6a and Figure 3.6b plot the internal mismatch strains and the normalized stress distributions as a function of the dimensionless distance at discharge rates of 0.5C and 2C, respectively. We represent E as $C_{22} = 375\text{GPa}$ used for the normalization. It can be seen that the outer shell (near $x/L = 1$) of the particle is under tension, while the core (near $x/L = 0$) is under compression during lithium insertion. The tensile stress in the outer shell may drive a preexisting crack to grow. The driving force is much larger for the faster discharge of rate 2C because of the highly inhomogeneous distribution of lithium.

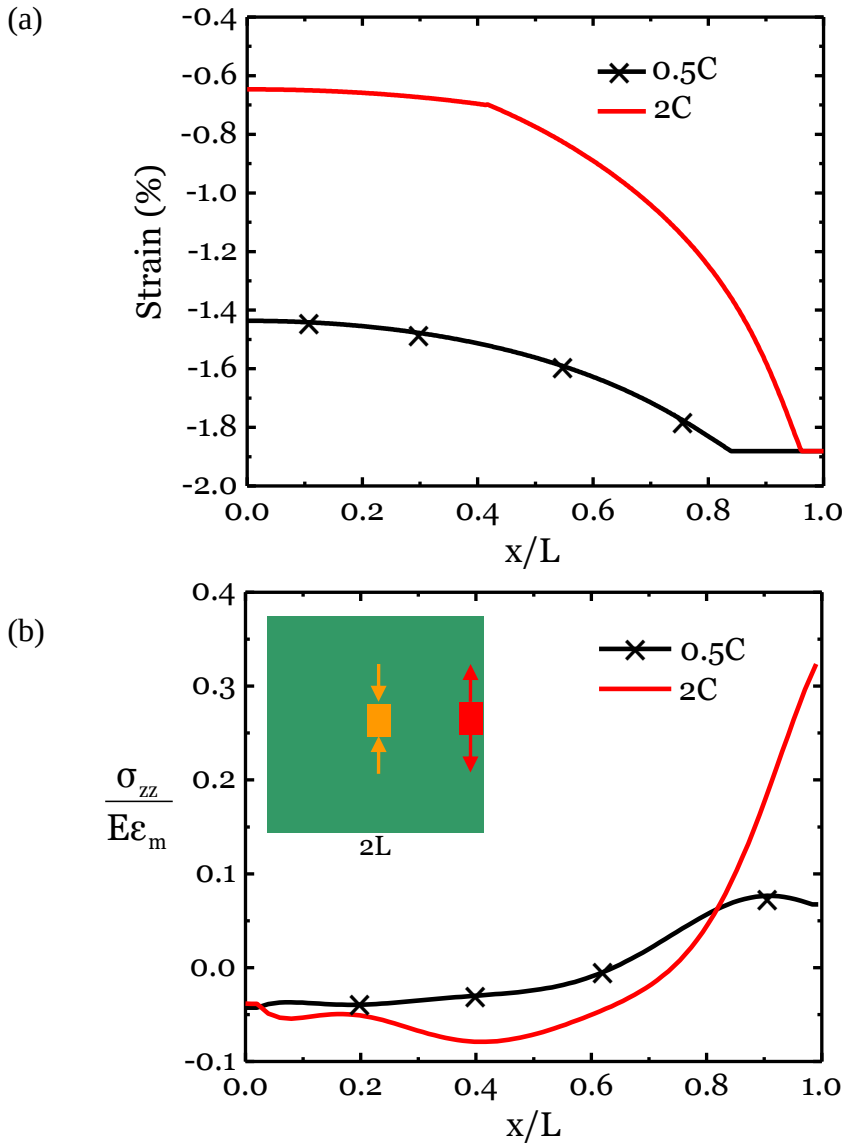

Figure 3.6. (a) Mismatch strain profile. (b) Normalized stress distribution at various discharge rates when the normalized lithium concentration at the outer surface reaches unity. The center of the particle is under compression, and the outside surface is under tension.

To calculate the energy release rate, a crack of length a is assumed to preexist inside the particle. In the simulation, we fix the particle size and the location of the preexisting crack, and we vary the preexisting crack length and discharge rate. In each case, we use the stress distribution at the end of discharge. The J-integral is used to calculate the energy release rate. Figure 3.7 gives the

normalized energy release rate dependence on the crack length to the particle size ratio, for discharge rates of 2C, 4C and 6C. The energy release rates are maximized at normalized lengths of 0.11, 0.09 and 0.07, respectively.

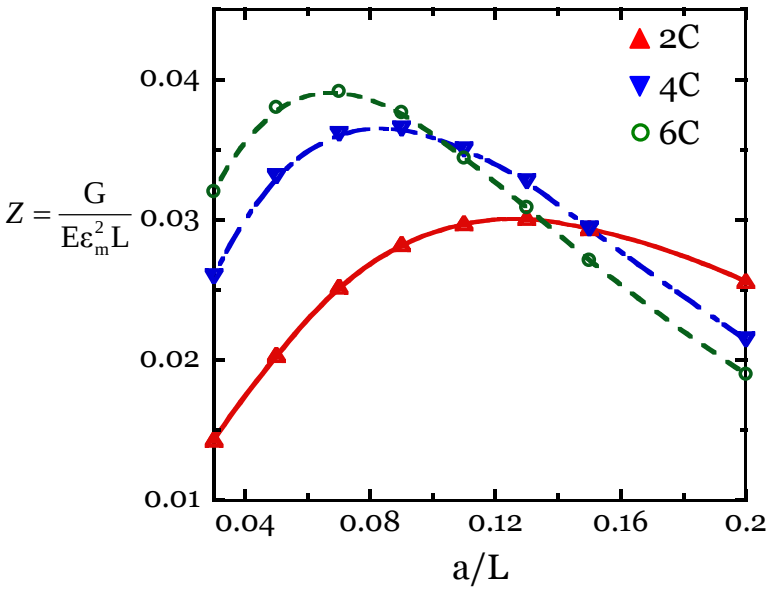

Figure 3.7. Energy release rate as a function of crack size at various discharge rates.

As pointed out in Section 3.2, no pre-existing crack can advance if the maximum energy release rate is smaller than the fracture energy. This condition defines a critical particle size

$$L_c = \frac{\Gamma}{Z_{\max} E \varepsilon_m^2}, \tag{3.10}$$

where Z is found from Figure 3.7. When the particle is smaller than the critical value, no preexisting crack in the particle can advance. The critical particle size as a function of discharge rate is illustrated in Figure 3.8. Here we have used an approximate value of the fracture energy of $1\,J/m^2$ for $LiCoO_2$. From the figure, decreasing the electrode particle size can effectively prevent fracture during fast charging.

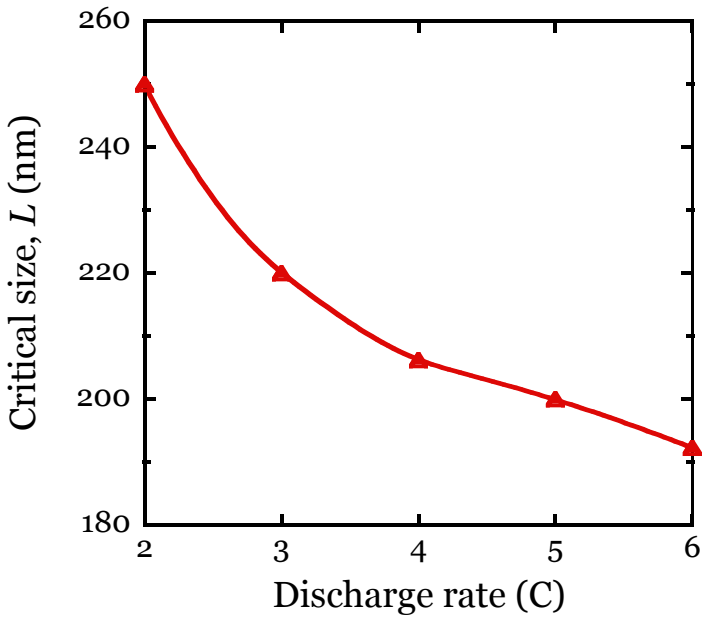

Figure 3.8. Critical $LiCoO_2$ particle size to avoid crack propagation as a function of discharge rate.

Experimental observations of cracked $LiCoO_2$ particles in the literature are limited. Crack damage is reported for an average particle size of 300 – 500 nm after 50 cycles.[13] The model presented here shows that fracture can be prevented by decreasing the electrode particle size and/or discharge rate. To further test the accuracy of the model, more data for fracture of particles of different sizes and for a range of discharge rates are needed. Finally, it should be noted we used stiffness coefficients derived from atomistic simulations and estimated fracture energy to calculate the critical particle size. These values may vary with lithium concentration,[78] and should be ascertained by further experiments.

3.4 Summary

Using a combination of diffusion kinetics and fracture mechanics, we have outlined a theory to study how material properties, particle size, and discharge rate

affect fracture of electrodes in lithium-ion batteries. We characterize the discharge rate relative to diffusion rate by a dimensionless parameter χ. We characterize the magnitude of the elastic energy relative to the fracture energy by a dimensionless parameter Λ. A "fracture map," demonstrating criteria for fracture, can be constructed in terms of the non-dimensional parameters Λ and χ. To illustrate the theory, a numerical example of a $LiCoO_2$ particle is presented. We calculate the distribution of lithium and stress at different discharge rates. We also calculate the energy release rates for preexisting flaws of different sizes. When the maximum energy release rate is smaller than the fracture energy, no pre-existing cracks can advance. This approach enables us to calculate the critical particle size and discharge rate necessary to avoid fracture.

Chapter 4

Inelastic Hosts as High-Capacity Electrodes

4.1 Introduction

Lithiation-induced deformation and fracture is a bottleneck in developing lithium-ion batteries of high capacity. For example, of all known materials for anodes, silicon offers the highest theoretical specific capacity—each Si atom can host up to 4.4 Li atoms. By comparison, in commercial anodes of graphite, every six carbon atoms can host up to one Li atom. Still, silicon is not used in anodes in commercial Li-ion batteries, mainly because after a small number of cycles the capacity fades, often attributed to lithiation-induced deformation and fracture.[17]

Recent experiments, however, have shown that the capacity can be maintained over many cycles for silicon anodes of small feature sizes, such as nanowires,[79] thin films,[80] and porous structures.[81] When silicon is fully lithiated, the volume of the material swells by ~300%. For anodes of small feature sizes, evidence has accumulated that this lithiation-induced strain can be accommodated by inelastic deformation. For instance, cyclic lithiation causes silicon thin films and silicon nanowires to develop undulations. [79],[80] Furthermore, the stress in a silicon thin film bonded on a wafer has been measured during charge and discharge, showing that the film deforms plastically upon reaching a yield strength.[82]

Existing models of lithiation-induced deformation and fracture have assumed that the electrodes are elastic.[11], [56], [61]-[68] Here we model inelastic electrodes by

considering diffusion, elastic-plastic deformation, and fracture. The model shows that fracture is averted for a small and soft host of lithium—an inelastic host of a small feature size and low yield strength.

4.2 Elastic versus inelastic hosts of lithium

We classify hosts of Li into two types: elastic and inelastic. For an elastic host, the host atoms recover their configurations after cycles of charge and discharge (Figure 4.1a). For example, for an electrode of a layered structure, within each layer the host atoms form strong bonds, while neighboring layers are held together by relatively weak bonds. Li diffuses in the plane between the layers, leaving the strong bonds within each layer intact. Elastic hosts are used in commercial Li-ion batteries for both cathodes (e.g., $LiCoO_2$) and anodes (e.g., graphite). By contrast, an inelastic host does not fully recover its structure after cycles of charge and discharge (Figure 4.1b). For example, when an electrode is an amorphous solid, such as amorphous silicon, the host atoms may change neighbors after a cycle of charge and discharge.

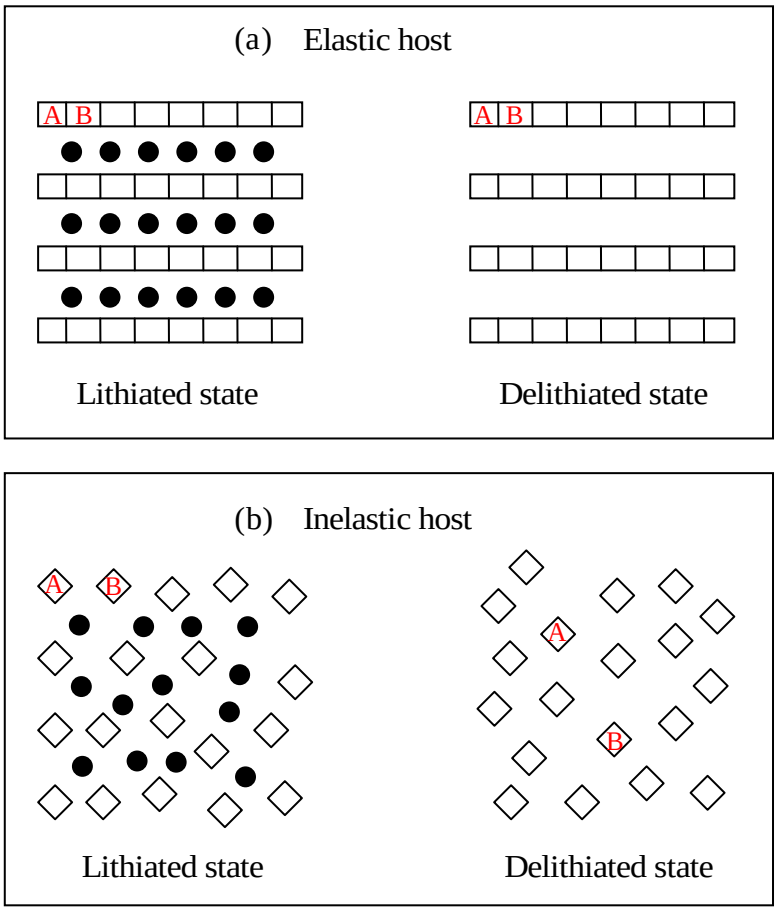

Figure 4.1. (a) For an elastic host of lithium, the host atoms recover their configurations after a cycle of lithiation. (b) For an inelastic host of lithium, the host atoms may change neighbors after a cycle of lithiation. Squares represent host atoms, and circles represent lithium atoms.

Whether lithiation-induced strain will cause an electrode to fracture depends on the feature size of the electrode.[50] The energy release rate, G, for a crack in a body of a small feature size takes the form $G = Z\sigma^2 h / E$, where h is the feature size, E is Young's modulus, σ is a representative stress in the body, and Z is a dimensionless number of order unity.[72] Fracture is averted if G is below the fracture energy of the material, Γ. Consequently, fracture is averted if the feature size is below the critical value

$$h_c = \frac{\Gamma E}{Z\sigma^2} \tag{4.1}$$

Representative values for silicon are $\Gamma = 10$ J/m^2 and $E = 80$ GPa.[83]

If silicon were an elastic host, the linear lithiation-induced strain of $\varepsilon \approx 100\%$ would cause stress on the order $\sigma \sim E\varepsilon$. Equation (4.1) would predict a subatomic critical size to avoid fracture. This prediction disagrees with the experimental observations—silicon anodes of feature sizes around 100 nm do survive many cycles of charge and discharge without fracture.[80]

By contrast, for an inelastic host, lithiation-induced strain can be accommodated by inelastic deformation. In this case, the generated stress will scale with the yield strength of the material. For a thin film of silicon bonded on a thick substrate, the measured yield strength is $\sigma_Y = 1.75$ GPa.[82] For a channel crack in the film, Z = 2 is a typical value.[72] Using these values, Equation (4.1) predicts a critical thickness of 130 nm. This prediction agrees well with available experimental observations: a 250 nm silicon thin film fractured after a few cycles,[84] while a 50 nm silicon film survived without fracture after 1000 cycles.[80] In general, for an inelastic electrode of a large capacity, fracture is averted if the feature size is small and the yield strength is low. One extreme is a liquid electrode, which accommodates the absorption-induced strain by flow, and can potentially provide ultra-high capacity.[85]-[87]

During charge and discharge, the stress in an electrode is a time-dependent field. Furthermore, the magnitude of the stress may exceed the yield strength at places under triaxial constraint. To explore these effects, we describe an inelastic

host of lithium by adapting an elastic and perfectly plastic model.[88] The increment of the strain is defined by $d\varepsilon_{ij} = \left(du_{i,j} + du_{j,i}\right)/2$, where du_i is the increment of the displacement. The stress σ_{ij} satisfies the equilibrium equation, $\sigma_{ij,j} = 0$. The increment of the strain is taken to be the sum of three contributions:

$$d\varepsilon_{ij} = d\varepsilon_{ij}^{E} + d\varepsilon_{ij}^{P} + d\varepsilon_{ij}^{L}, \tag{4.2}$$

where ε_{ij}^{E} is the elastic strain, ε_{ij}^{P} the plastic strain, and ε_{ij}^{L} the lithiation-induced strain. The elastic strain obeys Hooke's law:

$$d\varepsilon_{ij}^{E} = d\left(\frac{1}{E}\left[\left(1+\upsilon\right)\sigma_{ij} - \upsilon\sigma_{kk}\delta_{ij}\right]\right), \tag{4.3}$$

where ν is Poisson's ratio. $\delta_{ij} = 1$ when $i = j$, and $\delta_{ij} = 0$ otherwise. The increment of the plastic strain is taken to obey the J_2-flow rule:

$$d\varepsilon_{ij}^{P} = \begin{cases} 0, & \sigma_e < \sigma_Y \\ 0, & \sigma_e = \sigma_Y,\ d\sigma_e < d\sigma_Y \\ \lambda s_{ij}, & \sigma_e = \sigma_Y,\ d\sigma_e = d\sigma_Y \end{cases}, \tag{4.4}$$

where $s_{ij} = \sigma_{ij} - \sigma_{kk}\delta_{ij}/3$ is the deviatoric stress and $\sigma_e = \sqrt{3 s_{ij} s_{ij}/2}$ the equivalent stress. Within the perfectly plastic model, λ at each increment is a positive scalar to be determined by the boundary-value problem. In general, the yield strength σ_Y can be a function of the concentration of lithium. The lithiation-induced strain is proportional to the concentration of lithium:

$$d\varepsilon_{ij}^{L} = d\left(\frac{\beta c}{3}\right)\delta_{ij}, \tag{4.5}$$

where β is a constant analogous to the coefficient of thermal expansion, and c denotes the normalized lithium concentration in the host–the lithium concentration divided by the concentration of lithium in the fully lithiated state.

The concentration of Li in an electrode is a time-dependent field, taken to be governed by the diffusion equation, $\partial c/\partial t = D\nabla^2 c$. For simplicity, in this chapter, we assume that the diffusivity D is a constant independent of the concentration and stress, and that diffusion is driven solely by the gradient of concentration.

As an illustration of the model, consider a thin film of amorphous silicon bonded on a substrate. Let h be the thickness of the film, and τ the time used to complete charge or discharge. We consider the limit $h << \sqrt{D\tau}$, where the film is so thin that the concentration of Li is homogeneous throughout the thickness of the film during electrochemical cycling. The stresses in the film are given by $\sigma_{xx} = \sigma_{yy} = \sigma$, $\sigma_{zz} = 0$, where x and y represent the in-plane directions, and z represents the out-of-plane direction. The magnitude of the stress σ is homogenous in the film, but varies during the progression of lithiation. The increment of the elastic strain is $d\varepsilon^e_{xx} = d\varepsilon^e_{yy} = (1-\nu)d\sigma/E$. The in-plane deformation of the thin film is constrained by the substrate, namely, $d\varepsilon_{xx} = d\varepsilon_{yy} = 0$. In the elastic stage, the increment of the plastic strain vanishes, so that

$$\frac{d\sigma}{dc} = -\frac{\beta E}{3(1-\upsilon)}. \tag{4.6}$$

Figure 4.2 shows the stress evolution as a function of lithium concentration, c. When lithium is first inserted, the film initially deforms elastically, and develops a compressive stress, with the slope given by Equation (4.6). When the magnitude of compressive stress reaches the yield strength, σ_Y, the film deforms plastically. For simplicity, in this chapter, the yield strength is taken to be a constant, independent of the concentration of lithium. Upon delithiation, the film initially unloads elastically,

develops a tensile stress, and then deforms plastically in tension. The fully lithiated state causes a volume expansion about 300%,[6] so that $\beta = 3$. Using representative values for silicon of $E = 80$ GPa and $\upsilon = 0.22$,[83] Equation (4.6) predicts a slope $d\sigma / dc = -103$GPa , which may be compared to the measured value -75 GPa given in Reference [82].

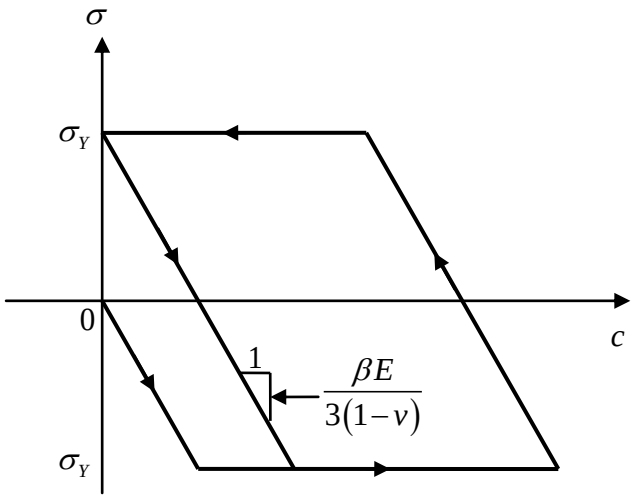

Figure 4.2. Evolution of stress in a thin film of an inelastic host during cyclic lithiation and delithiation.

4.3 Lithiation-induced stresses in a silicon particle

In a thin film, stresses can be induced by the constraint imposed by the substrate. By contrast, a particle, a nanowire, or a porous structure is almost unconstrained by other materials, and the stress is mainly induced by the inhomogeneous distribution of lithium.[12] Consequently, the stress is small when the feature size and charge rate are small.

To explore the effect of inelastic deformation, we study the evolution of the stress field in a spherical particle of silicon. We use the "Thermal-Structural Interaction" module in COMSOL to solve the coupled diffusion and elastic-plastic

problem. The lithiation-induced strain is simulated by imposing a thermal strain. Initially, the particle is taken as pure silicon, and is charged and discharged at a constant current. The dimensionless charge and discharge rate is set to be $i_n a / DC_{\max} = 0.206$, where a is the radius of the particle, i_n is the current density for charge and discharge, and $C_{\max}$ is the theoretical capacity of fully lithiated silicon. This dimensionless rate corresponds to $i_n = 0.176 \text{A/m}^2$ for representative values $a = 1\ \mu\text{m}$, $D = 1\times10^{-16}\ \text{m}^2/\text{s}$ [89] and $C_{\max} = 8.52\times10^{9}\ \text{Coulomb/m}^3$. [90] At this rate, silicon would be lithiated to its full theoretical capacity in about 4.5 hours.

Figure 4.3a shows the distribution of lithium at several times during lithiation, and Figures 4.3b-d show the corresponding distributions of the equivalent, radial, and hoop stresses. The equivalent stress is bounded by the limits $0 \le \sigma_e \le \sigma_Y$. The traction-free boundary-condition requires the radial stress at the surface of the particle to vanish at all times. As more lithium is inserted, the particle expands more near the surface than it does near its center, resulting in tensile radial stresses. The hoop stress is compressive near the surface and tensile near the center. For the spherical particle, the yield condition takes the form $|\sigma_{\theta\theta} - \sigma_{rr}| = \sigma_Y$. Due to the triaxial constraint at the center of the particle, the radial stress and hoop stress can exceed the yield strength. Additional calculations (not shown here) indicate that faster charging rates result in even larger values of the radial and hoop stresses. These large tensile stresses may cause fracture. Also, large values of hydrostatic stress may cause an inelastic material to grow cavities,[88] although we are unaware of any experimental observation of lithiation-induced cavitation.

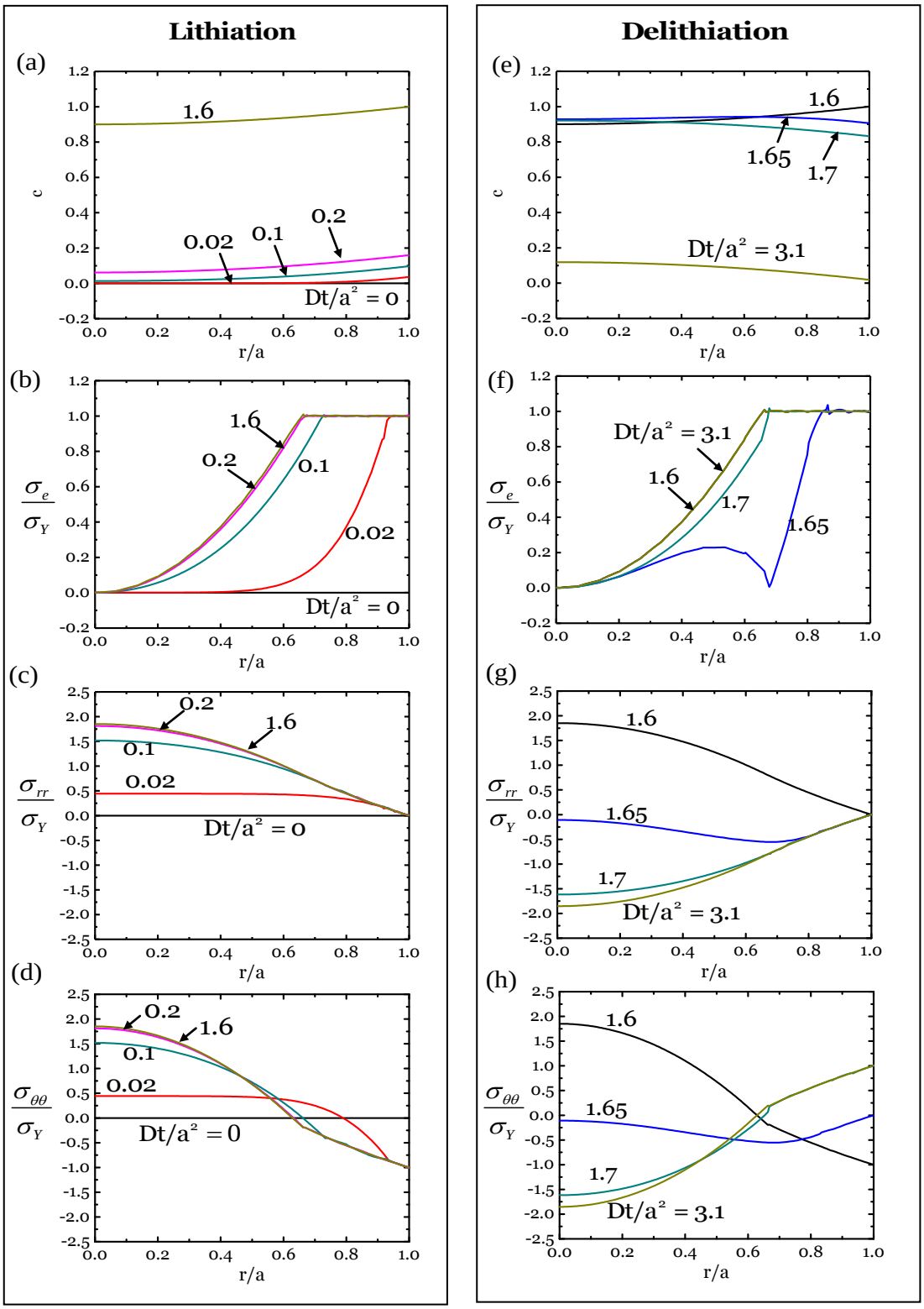

Figure 4.3. Time evolution of (a) concentration of lithium, (b) equivalent stress, (c) radial stress, and (d) hoop stress in a spherical particle of silicon during lithiation. Time evolution of (e) concentration of lithium, (f) equivalent stress, (g) radial stress, and (h) hoop stress during delithiation.

The lithium concentration at the surface reaches a value of unity at time $Dt/a^2 = 1.6$. At this point, we reverse the electric current and start delithiation. Figure 4.3e shows the distribution of lithium at several times during delithiation, and Figs. 4.3f-h show the corresponding distributions of the equivalent, radial, and hoop stresses. As lithium is extracted, the radial stress evolves from tension to compression. Also, the hoop stress at the surface becomes tensile with magnitude σ_Y. This tensile stress may result in the propagation of surface flaws. Similar to a thin film, the sphere can avert fracture if the radius is small and the yield strength is low.

4.4 Summary

We have modeled diffusion and elastic-plastic deformation in an inelastic host of lithium. The model allows us to simulate the distribution of lithium and stress in the host electrode during charge and discharge. For an electrode of a small feature size and low yield strength, inelastic deformation helps prevent fracture.

Chapter 5

Fracture and Debonding in Coated Hollow Electrodes

5.1 Introduction

Silicon can host a large amount of lithium, making it one of the most promising materials to replace the conventional carbon-based anodes. However, the commercialization of silicon anodes has been limited by mechanical failure and chemical degradation.[93] Mechanical failure results from the dramatic swelling and stress generated during cyclic lithiation and delithiation. The stress may cause fracture of the conductive matrix and active particles, leading to the loss of the conduction path for electrons, as shown in Figure 5.1a. As a result, rapid capacity fading of silicon often occurs in the first few cycles.[50] Chemical degradation is attributed mainly to the formation of solid electrolyte interphase (SEI) resulting from the reactions between the electrode and the electrolyte.[93] The formation of the SEI consumes active materials and results in irreversible capacity loss in the first cycle, as shown in Figure 5.1b. Furthermore, the repeated swelling and de-swelling can cause continual shedding and re-forming of the SEI during cycling, resulting in a persistent decrease in the long-term coulombic efficiency.[10]

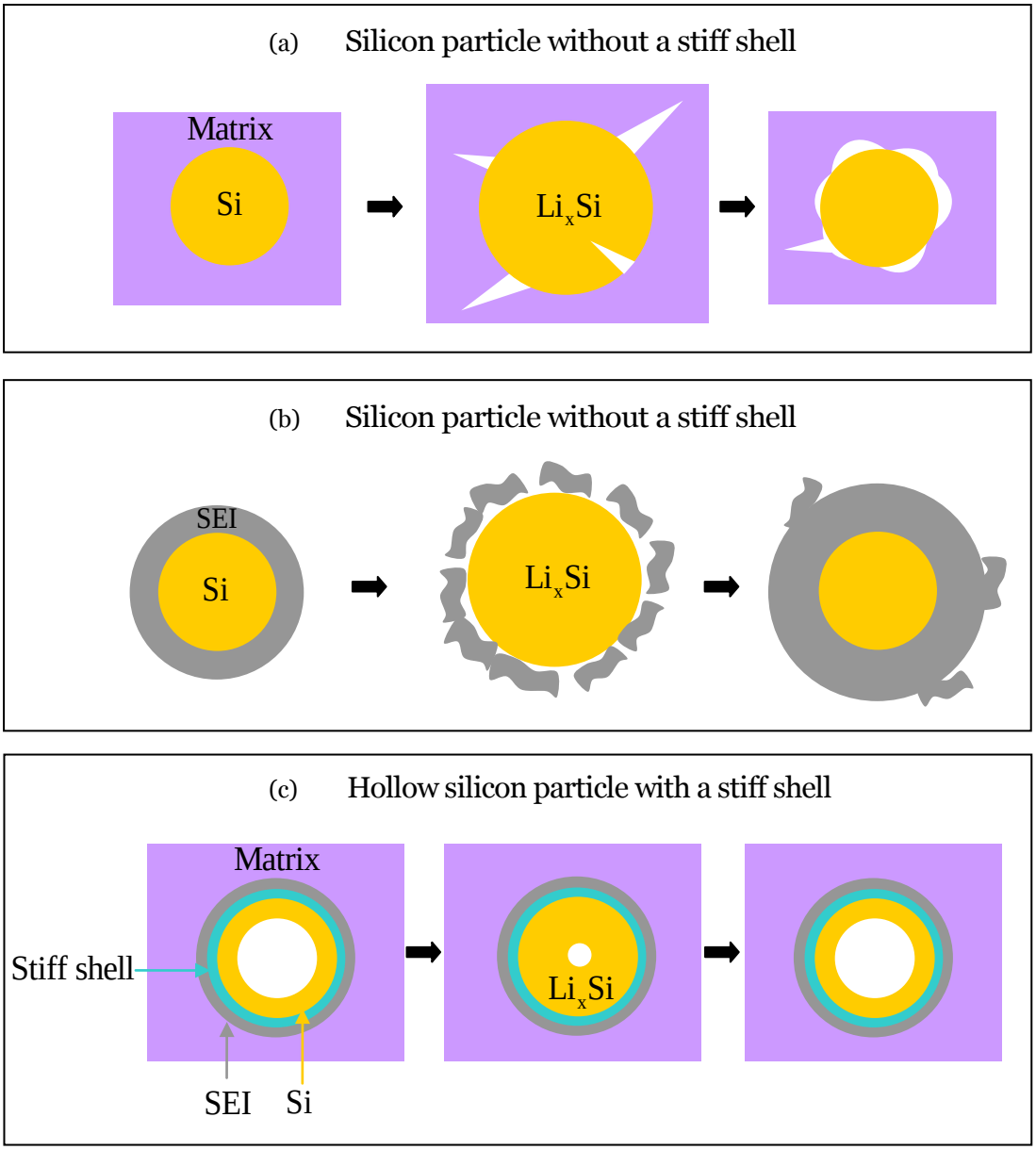

Figure 5.1. (a) For a silicon particle without a stiff shell, the stress induced by lithiation and delithiation may cause fracture of the active particle or debonding between the active particle and the matrix, leading to the loss of the conduction path for electrons. (b) Also for a silicon particle without a stiff shell, the deformation associated with lithiation and delithiation may cause the shedding and re-forming of the solid-electrolyte interphase (SEI), consuming active materials. (c) For a hollow silicon particle with a stiff shell, the deformation of silicon is accommodated by inward swelling, so that electric contact is maintained, and the shedding of SEI avoided.

Recent experiments show that mechanical failure can be mitigated by using nanostructured silicon anodes, such as nanowires,[79] thin films,[94]-[96] hollow nanoparticles,[97] and nanoporous structures.[81] These structures alleviate the stress

by managing the deformation through shape optimization and geometric restrictions. Furthermore, intense efforts are being dedicated to stabilizing the SEI layer during lithiation cycles. Current methods include coating a thin artificial SEI layer on the surface of silicon[98]-[104] and using additives in the electrolyte to avoid the continual consumption of active materials.[105]-[109]

A recent design of electrodes involves hollow core-shell nanostructures, which can enhance the mechanical and chemical stability of silicon anodes simultaneously, as shown in Figure 5.1c. Such structures enable silicon electrodes to sustain over six thousand cycles with high coulombic efficiency.[110] In a hollow core-shell nanostructure, the shell separates the electrolyte and the electrode (core), and forces the core to swell into the hollow space in the interior of the structure. Because the shell restricts outward swelling of the core, the continual SEI shedding and re-forming is suppressed, and the electric contact between the electrode and the matrix is maintained. Similar designs based on encapsulating silicon nanoparticles within hollow carbon shells show promise for high-capacity electrodes with long cycle life of hundreds of cycles. [111]-[113]

Constrained lithiation and delithiation, however, induce stress in the hollow core-shell structures. During lithiation, Figure 5.2a, the core is under compressive stresses, and the shell is under tensile hoop stress. Such tensile stress can initiate fracture in the shell. During delithiation, Figure 5.2b, the radial stress can be tensile in both the core and the shell. Such stress may cause interfacial debonding.

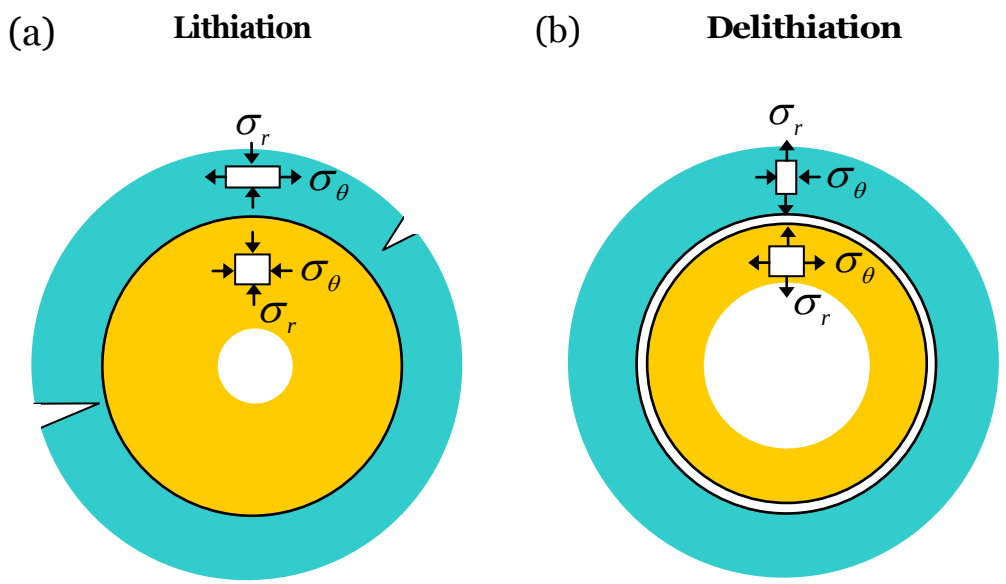

Figure 5.2. Two potential modes of failure in a hollow silicon particle coated with a stiff shell. (a) The lithiation of the silicon particle induces tensile hoop stress in the shell, which may cause the shell to fracture. (b) The delithiation of the silicon particle induces tensile radial stress, which may cause debonding between the core and the shell.

To facilitate lithium diffusion and reduce overall weight, the ideal shell should be thin. However, an extremely thin shell is unable to constrain the outward expansion of the core. The insertion reaction causes large deformation in the core, but the magnitude of the stress is kept manageable by plastic flow. In this chapter, we calculate the stress field resulting from the concurrent insertion reaction and plastic flow in hollow spherical nanoparticles and nanowires of silicon coated with stiff shells. We identify conditions to avoid fracture and debonding in terms of the radius of the core, the thickness of the shell, and the state of charge. We further identify the driving forces for the lithiation reaction and discuss the effect of the stress field on the electrochemical reaction.

5.2 Stresses in a coated hollow spherical particle of silicon

In a hollow core-shell structure, the stiff shell forces the core to swell into the inner hollow space (Figure 5.3). Before absorbing any lithium, the inner radius of the hollow particle is *A*, and the outer radius is *B*. The particle is coated by a stiff shell of outer radius *C*. We consider the case where the rate of lithiation is slow relative to diffusion of lithium through the core, so that lithium atoms have enough time to homogenize in the core. For efficiency, to completely fill the hollow space upon full lithiation, the structure should satisfy the geometric relation:

$$\frac{A}{B}=\left(\frac{\beta-1}{\beta}\right)^{1/3}, \tag{5.1}$$

where β is the volumetric swelling ratio $\beta=V_f/V_i$, with V_f representing the fully lithiated volume of the core and V_i the initial volume of the lithium-free state of the core. Lithiation of silicon causes a volumetric swelling $\beta=4$, so that $A/B=(3/4)^{1/3}$.[17]

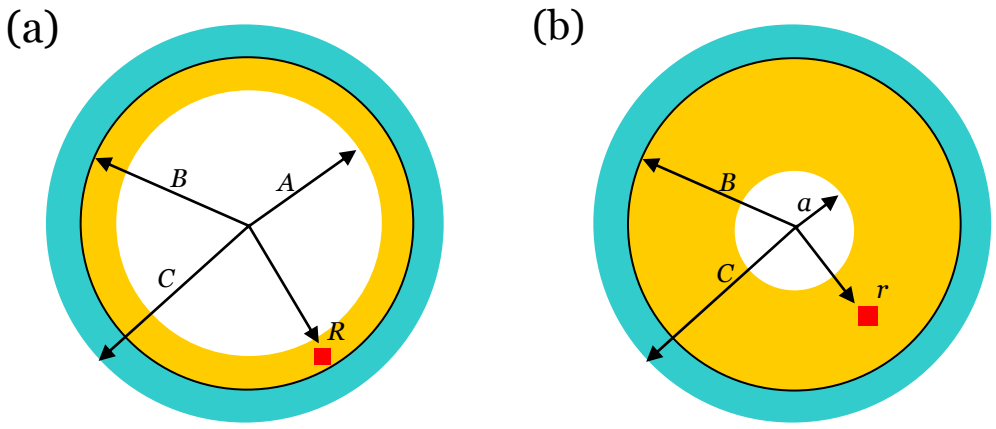

Figure 5.3. (a) In the reference state, a hollow particle of an electrode is stress-free and lithium-free. (b) In the current state, the particle is partially lithiated. The deformation of the core is accommodated by the inner hollow space. Outward deformation is restricted by the shell.

We take the stress-free and lithium-free state as the reference state, Figure 5.3a. At time *t*, the hollow particle absorbs some lithium, retaining its spherical symmetry. We assume that the outward expansion of the core is completely constrained by the stiff shell. Note that the elastic deformation of the shell, typically less than 1%, is much less than the lithiation-induced strain in the silicon core. With this assumption, lithiation changes only the inner radius a, and we neglect any deformation of the shell, Figure 5.3b. We represent a material element in the reference state by its distance *R* from the center of the particle. At time *t*, the material element moves to a place a distance *r* from the center. The function *r(R, t)* specifies the kinematics of the deformation. Each material element in the hollow core is subject to a state of triaxial stresses, $(\sigma_r, \sigma_\theta, \sigma_\theta)$, where σ_r is the radial stress and σ_θ is the hoop stress. The stresses are inhomogeneous, represented by functions $\sigma_r(r,t)$ and $\sigma_\theta(r,t)$. The balance of forces acting on a material element requires that

$$\frac{\partial \sigma_r(r,t)}{\partial r} + 2\frac{\sigma_r(r,t) - \sigma_\theta(r,t)}{r} = 0. \tag{5.2}$$

We adopt the commonly used idealization that plastic deformation is unaffected when a hydrostatic stress is superimposed. Furthermore, the yield strength of the lithiated silicon, σ_Y, is taken to be constant and independent of the amount of deformation and the concentration of lithium. Because the elastic strain is negligible compared to the lithiation-induced strain, the elasticity of the hollow core is neglected. During lithiation, a material element of silicon is under compression in the hoop direction and is in the state $\sigma_r - \sigma_\theta = \sigma_Y$. Setting $\sigma_r - \sigma_\theta = \sigma_Y$ in Equation

(5.2) and integrating over r with the traction-free boundary condition, $\sigma_r(a, t)=0$, the radial stress in the hollow core is given by

$$\sigma_r = -2\sigma_Y \log\frac{r}{a}, \qquad a \le r \le B \tag{5.3}$$

The hoop stress in the hollow core is determined by $\sigma_r - \sigma_\theta = \sigma_Y$, giving

$$\sigma_\theta = -\sigma_Y\left(2\log\frac{r}{a}+1\right), \qquad a \le r \le B. \tag{5.4}$$

The stress fields in the elastic shell take the familiar solutions of Lamé problems,[114] with the radial stress

$$\sigma_r = -2\sigma_Y\left(\log\frac{B}{a}\right)\left(\frac{B^3}{C^3-B^3}\right)\left(\frac{C^3}{r^3}-1\right), \quad B < r \le C, \tag{5.5}$$

and the hoop stress

$$\sigma_\theta = 2\sigma_Y\left(\log\frac{B}{a}\right)\left(\frac{B^3}{C^3-B^3}\right)\left(\frac{C^3}{2r^3}+1\right), \quad B < r \le C. \tag{5.6}$$

During delithiation, a material element of the hollow core is under tension in the hoop direction, and is in the state $\sigma_r - \sigma_\theta = -\sigma_Y$. Setting $\sigma_r - \sigma_\theta = -\sigma_Y$ in Eq. (5.2) we obtain the radial stress in the hollow core by integrating over r,

$$\sigma_r = 2\sigma_Y \log\frac{r}{a}, \quad a \le r \le B, \tag{5.7}$$

and the hoop stress,

$$\sigma_\theta = \sigma_Y\left(2\log\frac{r}{a}+1\right), \quad a \le r < B. \tag{5.8}$$

A comparison of the stress fields indicates a jump in both the radial and hoop stresses from lithiation to delithiation as is shown in Figure 5.4. These jumps are caused due to our neglecting the elastic strain. Should we include the elastic strain, the stresses would make this transition from compressive to tensile yielding after the removal of a

very small amount of lithium.

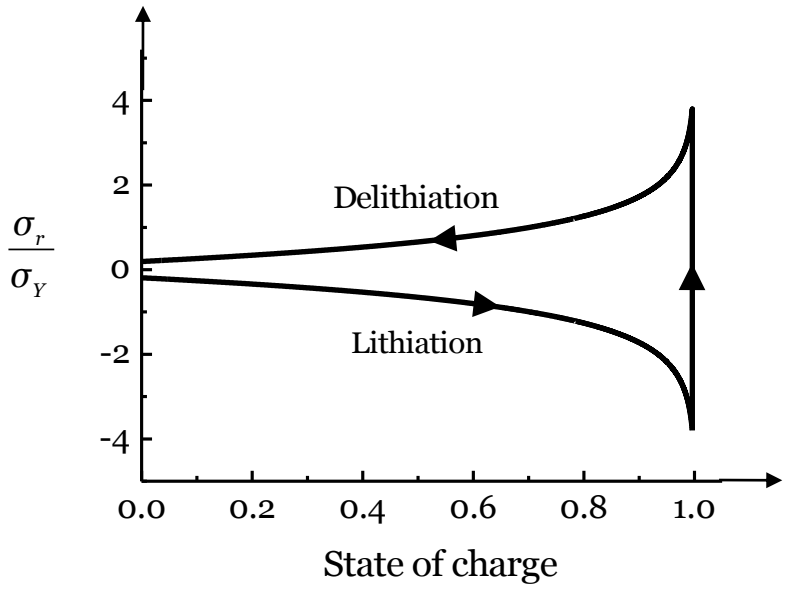

Figure 5.4. Evolution of the radial stress at the interface between the particle and the shell during lithiation and delithiation.

Mechanical failure is mainly due to the stress at the interface between the core and shell. Figure 5.4 shows the evolution of the radial stress at the interface of the hollow core during lithiation and delithiation. The stress is plotted as a function of the state of charge (SOC) – 0 represents the lithium-free state, and 1 represents the fully lithiated state. Given the geometric condition in Eq. (5.1), the state of charge is calculated by using the inner radius a at a given state,

$$SOC = \frac{A^3 - a^3}{A^3}. \tag{5.9}$$

As expected, the hollow core is under compression in the radial direction during lithiation. The compressive stress increases logarithmically with the state of lithiation, Eq.(5.3). Because of the triaxial state of stress, the magnitudes of the components of the stress readily exceed the yield strength of lithiated silicon.[115] Such large compressive stresses in the core can cause a large tensile hoop stress in the

outer shell, which may lead to fracture of the shell. During delithiation, the core-shell interface is under tensile stress in both the radial and hoop directions. The magnitudes of the stress components are maximized at the beginning of the delithiation, and gradually decrease with the state of delithiation. The tensile stress in the radial direction may initiate interfacial debonding, resulting in a loss of electrical contact between the core and the shell.

5.3 Fracture and debonding analysis

We now analyze fracture of the coating using an approach similar to that described in several recent papers.[11]-[12] We focus on fracture of the coating caused by the tensile hoop stress during lithiation. Linear elastic fracture mechanics is adopted. The reduction in the elastic energy associated with a crack advancing a unit area defines the energy release rate, G_f. Dimensional analysis dictates that the energy release rate should take the form

$$G_f = Z\frac{\sigma_\theta^{\,2}}{E_s}(C-B), \tag{5.10}$$

where E_s is Young's modulus of the shell, Z is a dimensionless parameter to be determined by solving the elastic boundary-value problem, σ_θ is the stress in the hoop direction given by Equation (5.6), and $C-B$ is the thickness of the surface coating. In the case of a channel crack in the thin shell, $Z=2$ is a typical value.[72] Inserting this value of Z and Equation (5.6) into Equation (5.10) gives an analytical solution for the energy release rate:

$$G_f = \frac{8\sigma_Y^{\,2}}{E_s}\left(\log\frac{B}{a}\right)^2\left(\frac{B^3}{C^3-B^3}\right)^2\left(1+\frac{C^3}{2B^3}\right)^2(C-B), \tag{5.11}$$

where we have approximated $r \approx B$ since $B \gg C-B$. In this limit, Equation (5.11) can be further approximated as

$$G_f \approx 2\frac{\sigma_Y^{\,2}}{E_s}\left(\log\frac{B}{a}\right)^2\frac{B^2}{C-B}. \tag{5.12}$$

The energy release rate is proportional to the square of the yield strength of lithiated silicon, the compliance of the surface coating, the ratio of the sizes of core and shell, and the size of the core. Therefore, to minimize the energy release rate, it is desired to have a small and soft hollow core and a thick and stiff surface shell. However, the shell also needs to be thin to minimize weight and to allow for fast diffusion of lithium through its thickness.

We take the same approach for the analysis of interfacial debonding. Here we consider that the energy release rate of debonding is mainly attributed to mode I fracture caused by the tensile radial stress. We assume a pre-existing crack of a size comparable to the thickness of the shell, $C-B$. As such, the energy release rate may be reduced to a simple form,

$$G_d = \pi\frac{\sigma_r^{\,2}}{E_e}(C-B). \tag{5.13}$$

The value of the numerical pre-factor in (5.13) is approximate, which changes somewhat with the elastic mismatch between the shell and the core and with the relative length of the crack to the thickness of the shell. Accurate values of the factor can be calculated by solving the boundary-value problem using the finite-element method.[91] In this work, however, a particular value is used to illustrate the main

ideas and the scaling relations. The radial stress during delithiation is given by Equation (5. 7), and thus

$$G_d = 4\pi \frac{{\sigma_Y}^2}{E_e}\left(\log\frac{B}{a}\right)^2 (C-B). \tag{5.14}$$

Here E_e is the effective modulus that accounts for the effects of inhomogeneous properties of the core and shell. A typical relation is represented by

$$\frac{1}{E_e} = \left(\frac{1}{E_c} + \frac{1}{E_s}\right)/2. \tag{5.15}$$

where E_c is the modulus of the core, and E_s is the modulus of the shell.[72] Comparing Equations (5.12) and (5.14), we can see some interesting differences. Namely, the energy release rate for interfacial debonding scales directly with the shell thickness while the energy release rate for fracture of the shell scales inversely with the shell thickness. Furthermore, the energy release rate for debonding scales much more slowly with the core radius, B, than does the energy release rate for fracture of the shell.

Let Γ_f be the fracture energy of the shell, and Γ_d the interfacial energy between the core and the shell. No preexisting flaws will advance if the maximum energy release rate is less than the fracture energy. Therefore, $G_f = \Gamma_f$ defines the critical condition for initiation of fracture of the shell, and $G_d = \Gamma_d$ defines the critical condition for initiation of interfacial debonding.

Recent experiments indicate that a thin layer of Al_2O_3 deposited on silicon anodes by atomic layer deposition provides excellent improvement of the cycling stability of silicon anodes.[100], [102] Here we take the example of a hollow spherical

particle of silicon coated with a thin shell of Al_2O_3 to illustrate the above analysis. Representative values of lithiated silicon and Al_2O_3 are taken, $\sigma_Y = 1$ GPa [82] and $E_c = 12$ GPa for lithiated silicon,[116], [117] $E_s = 300$ GPa , $\Gamma_f = 40$ J/m^2 ,[118] and $\Gamma_d = 1$ J/m^2. We first construct a phase diagram to show the effects of the thickness of the shell and the state of charge, Figure 5.5a. We take a typical value of the silicon core size, $B = 200$ nm and $A/B = \sqrt[3]{3/4}$. The thickness of Al_2O_3, $C - B$, is varied. The state of charge is calculated from Equation (5.9). The solid black line represents the critical conditions for fracture of the shell, corresponding to the condition $G_f = \Gamma_f$, and the red dashed line represents the critical conditions of interfacial debonding, corresponding to the condition $G_d = \Gamma_d$. These two lines delineate an upper boundary to the safe regime in which no fracture of the surface coating or interfacial debonding would occur. Figure 5.5b further shows a phase diagram to demonstrate the effects of core size and state of charge. In this case, the thickness of the Al_2O_3 shell is fixed, $C - B = 5$ nm , and the core size B is varied while maintaining the geometric relation $A/B = \sqrt[3]{3/4}$. Given the analytical solutions of Equations (5.11) and (5.14), phase diagrams for other experimental conditions can be readily constructed.

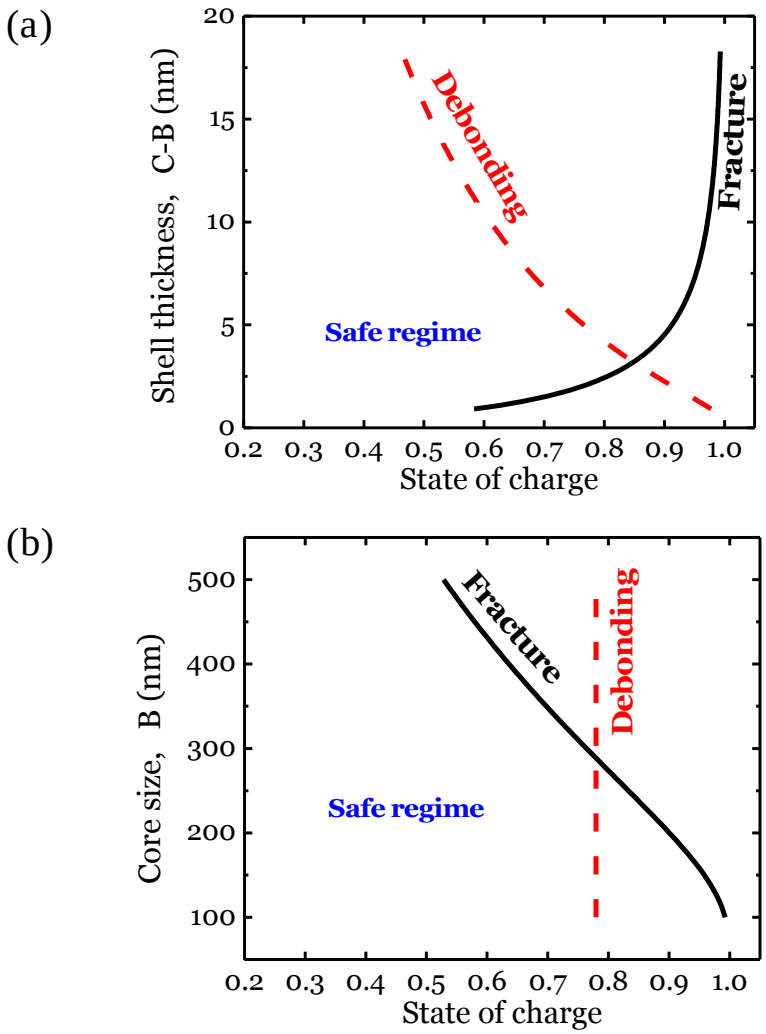

Figure 5.5. Conditions for fracture and debonding of a spherical hollow particle plotted in the plane of (a) the thickness of the shell and the state of charge, and (b) the radius of the particle and the state of charge.

5.4 Analysis of coated hollow silicon nanowires

One dimensional nanowires and nanotubes are emerging designs that can mitigate the mechanical failure of silicon electrodes. In particular, Y. Cui and co-workers illustrate that coated hollow nanowires enable silicon anodes to sustain over six thousands cycles with high coulombic efficiencies.[110] Such excellent performance would ultimately meet the requirement of commercializing silicon into

electric vehicles. In this section, we analyze fracture and debonding of a hollow nanowire. The cross-section is as shown in Figure 5.3. For complete utilization of the available hollow volume upon full lithiation, we must satisfy the geometric relation:

$$\frac{A}{B}=\left(\frac{\beta-1}{\beta}\right)^{1/2}, \tag{5.16}$$

where for silicon $\beta=4$ and $A/B=(3/4)^{1/2}$.

Similar to the case of spherical particles, lithiation of silicon causes a tensile hoop stress in the shell, which may fracture the coating material. Furthermore, a large tensile radial stress is developed at the beginning of delithiation, which may initiate interfacial debonding. We derive the stress field in the Appendix A. Since the deformation of the core along the axial direction is constrained by the shell, lithiated silicon is assumed to deform under plane-strain conditions. The analytical solution of fracture energy release rate of the shell during lithiation is given by

$$G_f=\frac{8}{3}\frac{\sigma_Y^{\,2}}{E_s}\left(\log\frac{B}{a}\right)^2\left(\frac{B^2}{C^2-B^2}\right)^2\left(1+\frac{C^2}{B^2}\right)^2(C-B). \tag{5.17}$$

In the case of $C\approx B$, Equation (5. 17) can be further approximated as

$$G_f\approx\frac{8}{3}\frac{\sigma_Y^{\,2}}{E_s}\left(\log\frac{B}{a}\right)^2\frac{B^2}{C-B}. \tag{5.18}$$

And the interfacial fracture energy during delithiation is given by

$$G_d=\frac{4\pi}{3}\frac{\sigma_Y^{\,2}}{E_e}\left(\log\frac{B}{a}\right)^2(C-B). \tag{5.19}$$

Comparing the fracture energies in the spherical particle and the nanowire, we find that the energy release rate for fracture of the shell is a factor of 4/3 larger for the nanowire than for the sphere. In contrast, the energy release rate for interfacial

debonding is 3 times larger in the sphere than in the nanowire.

We now consider the practical example of a hollow silicon nanowire coated with a thin layer of Al_2O_3. A phase diagram showing the effects of the thickness of the shell and the state of charge is given in Figure 5.6a.

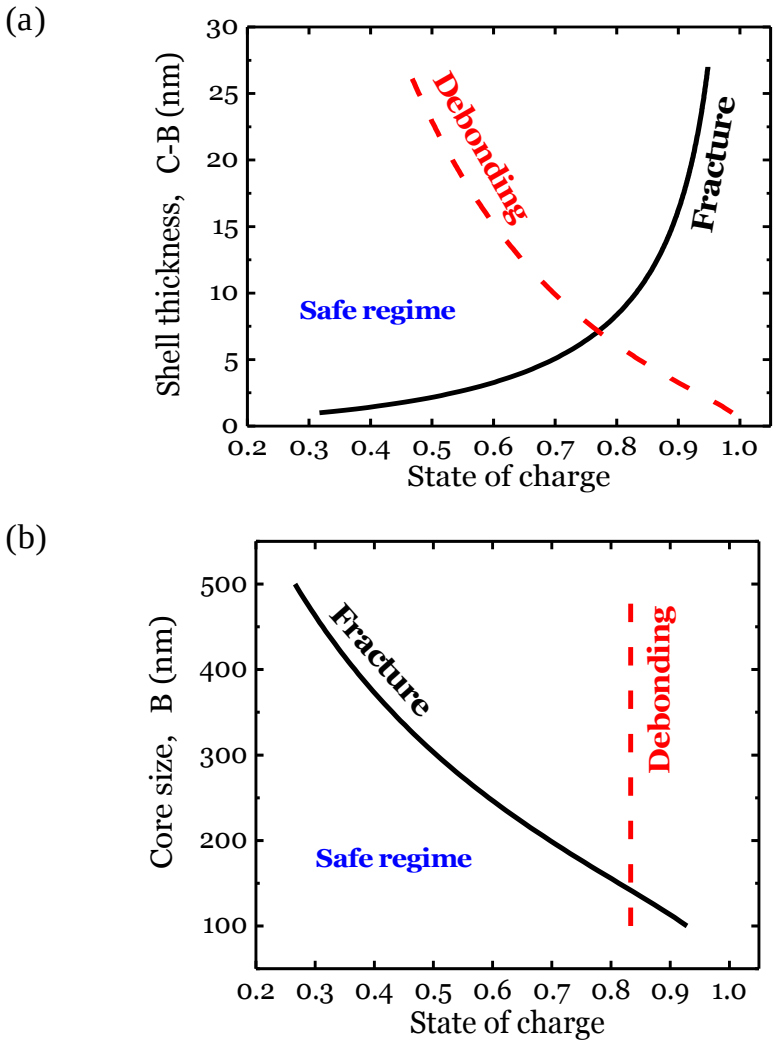

Figure 5.6. Conditions of fracture and debonding for a hollow nanowire plotted in the plane of (a) the thickness of the shell and the state of charge, and (b) the radius of the particle and the state of charge.

In the nanowires, the state of charge is calculated by

$$SOC = \frac{A^2 - a^2}{A^2}. \tag{5.20}$$

The silicon core size is taken as $B = 200$ nm and $A/B = (3/4)^{1/2}$. The thickness of

Al_2O_3, $C-B$, is varied. The solid black line corresponds to the critical conditions for fracture of the shell, given by $G_f = \Gamma_f$, and the red dashed line corresponds to the critical conditions for interfacial debonding, given by $G_d = \Gamma_d$. Figure 5.6b shows a phase diagram demonstrating the effects of the core size and state of charge. In this case, the thickness of the Al_2O_3 shell is taken as $C-B=5$ nm, and the core size B is varied while maintaining the geometric relation $A/B=\sqrt{3/4}$. More accurate measurements of Γ_d are needed to produce a more accurate plot. In the case where the interfacial fracture energy Γ_d is less than the value we have used here, the red dashed lines in Figures 5.5 and 5.6 would shift to a lower state of charge limit.

5.5 Stress effect on the lithiation reaction

We now identify the driving forces for the lithiation reaction of silicon, namely, the change of free energy associated with the reaction. Let ΔG_r be the free energy of the lithiation reaction of silicon when both the stress and the applied voltage vanish. Assume the silicon anode is connected to a cathode by a conducting wire through a voltage source. Associated with converting one Li atom and Si into lithiated silicon, one electron passes through the external wire, so that the voltage source does work $e\Phi$, where Φ is the voltage, and e the elementary charge (a positive quantity). The driving force is further modified when the effects of stress are included. During lithiation of the coated hollow silicon particle, Li atoms migrate into Si by overcoming an energy barrier induced by the compressive stress in the core. Thus, when one Li atom is incorporated into lithiated silicon, the stress does work $-\Omega\sigma_m$, where σ_m is

the mean stress in the core, and Ω is the change in volume caused by insertion of one Li atom. Here we assume an isotropic swelling of Si caused by Li insertion such that only the contribution from the mean stress is included. We also consider small elastic deformation of lithiated silicon such that stress terms of higher orders can be neglected.[119] Combining the above contributions, we find that, when the reaction advances, the net change in the free energy is

$$\Delta G = \Delta G_r - e\Phi - \Omega\sigma_m . \tag{5.21}$$

We have neglected the dissipation at the electrolyte/electrode interfaces, as well as inside the electrodes and electrolytes. In our sign convention, a negative ΔG drives lithiation, and a more negative value represents a larger driving force. The free energy of reaction ΔG_r takes a negative value. The sign of $e\Phi$ depends on the polarity. We consider Φ being positive in the direction that drives lithiation. As expected, a compressive mean stress in silicon retards lithiation.

For both the spherical silicon particles and nanowires, the analytical solutions of the stress fields are given in the prior sections. Inserting the stresses into Equation (5.21), we can quantify the effect of stress on the lithiation reaction. We note that the compressive stress is maximized at the core-shell interface. Thus, the retarding effect of stress on the lithiation reaction is most significant at this interface. The contribution due to the stresses at the interface is plotted in Figure 5.7. In making this plot, we have adopted the value $\Omega = 1.36\times10^{-29}\,\mathrm{m}^3$.[92] As expected, the magnitude of the contribution from the stress increases with the state of charge. Recall that the free energy of formation of lithiated silicon is small; for example,

$\Delta G_r = -0.18$ eV for amorphous $Li_{2.1}Si$.[120] Consequently, the reaction can readily generate a large enough stress to counteract the electrochemical driving force, stalling the surface reaction prior to complete lithiation. In fact, a lower lithiation capacity due to an incomplete surface reaction has been observed in recent experiments.[121]

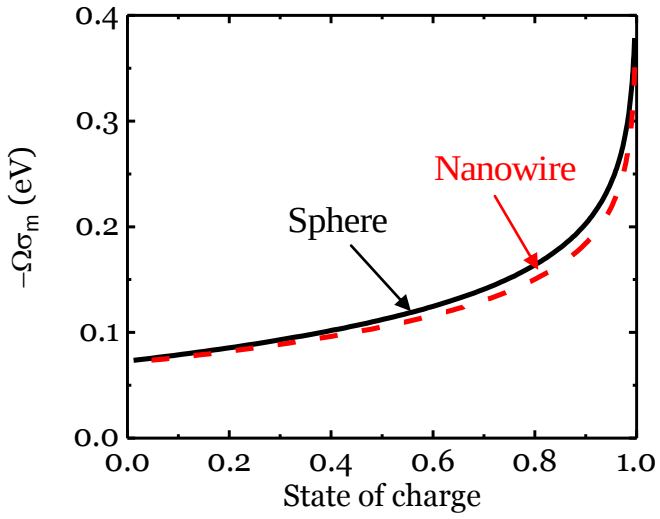

Figure 5.7. The effect of the stress on the driving force for the lithiation reaction is plotted as a function of the state of charge.

5.6 Summary

We present an analysis of fracture and debonding failure in coated hollow spherical particles and nanowires of silicon anodes. A phase diagram describing the critical structural parameters and operating conditions is constructed, outlining how to avoid fracture of the coating and debonding between the coating and the active material. We further explore the effect of the stress field on the lithiation reaction of silicon. The large compressive stress at the core-shell interface may counteract the electrochemical driving force, leading to a low lithiation capacity. The present

results and associated analysis provide insightful guidelines for a viable design of coated hollow nanostructures.

Chapter 6

Concurrent Reaction and Plasticity during the Intiial Lithiation of Crystalline Silicon Electrodes

6.1 Introduction

Nanostructured electrodes of silicon are often fabricated with crystalline silicon. In an electrochemical cell, crystalline Si and Li react at room temperature, forming an amorphous phase of lithiated silicon (Figure 6.1).[79],[120],[122],[137] The reaction front is atomically sharp—the phase boundary between the crystalline silicon and the lithiated silicon has a thickness of ~1 nm.[124] Evidence has accumulated recently that, in the nanostructured electrodes, the velocity of the reaction front is not limited by the diffusion of lithium through the amorphous phase, but by the reaction of Li and Si at the front. For example, it has been observed that under a constant voltage the displacement of the reaction front is linear in time.[125] This observation indicates that the rate of lithiation is limited by short-range processes at the reaction front, such as breaking and forming atomic bonds.

That the reaction is the rate-limiting step is perhaps most dramatically demonstrated by lithiated silicon of anisotropic morphologies. Recent experiments have shown that lithiated silicon grows preferentially in a direction perpendicular to the (110) planes of crystalline silicon.[125]-[127] It has been suggested that the anisotropic morphologies are due to the difference in diffusivities along various crystalline orientations of silicon. However, it is well established that the tensor of

diffusivity of a species in a cubic crystal is isotropic.[128] We propose that the observed anisotropic morphologies are due to the variation in the short-range atomic processes at the reaction fronts in different crystallographic orientations.

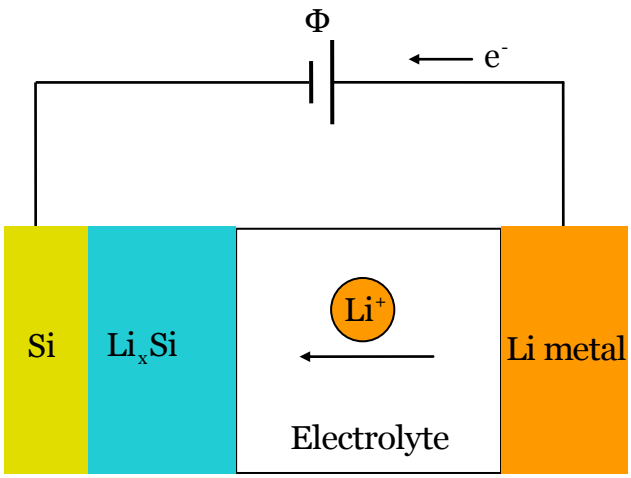

Figure 6.1. Schematic of an electrochemical test cell composed of a lithium metal anode and a crystalline silicon cathode. Crystalline silicon and lithium react at room temperature, forming an amorphous phase of lithiated silicon. The reaction front—the boundary between the crystalline silicon and the lithiated silicon—is atomically sharp.

We further note that, to accommodate the large volumetric expansion associated with the phase transition, the lithiated silicon must deform plastically. It is instructive to compare a flat reaction front with a curved one. When the reaction front is flat (Figure 6.2a), the large volumetric expansion associated with the reaction is accommodated by elongating the lithiated silicon in the direction normal to the reaction front, while maintaining the geometric compatibility between the two phases in the directions tangential to the reaction front. As the reaction front advances, freshly lithiated silicon is added at the front, and previously lithiated silicon recedes by rigid-body translation, with no deformation. The biaxial stresses in the lithiated silicon remain at the compressive yield strength. When the reaction front is flat,

reaction and plasticity are concurrent and co-locate—right at the reaction front. Indeed, the two processes may not be differentiated without ambiguity.

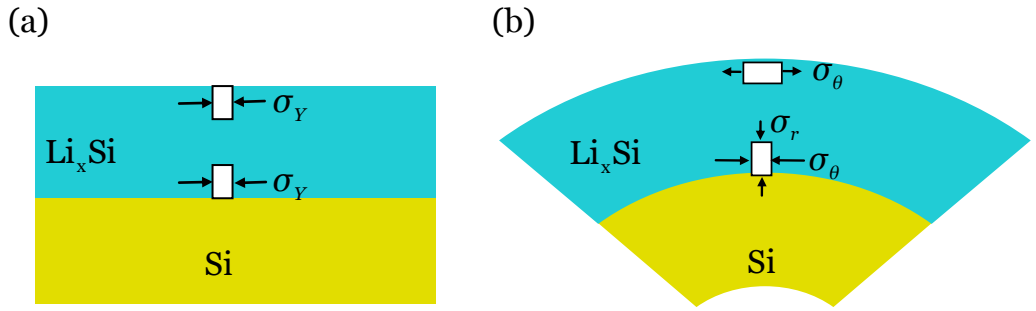

Figure 6.2. The lithiation of silicon causes a large volumetric expansion, which is accommodated by plastic deformation. (a) In a thin film with no curvature, as the reaction front advances, freshly lithiated silicon is added at the front, and previously lithiated silicon recedes by rigid-body translation, with no deformation. The biaxial stresses in the lithiated silicon remain at the compressive yield strength. (b) At a curved reaction front, an element of newly lithiated silicon undergoes compressive plastic deformation in the directions tangent to the reaction front. As the reaction front advances, the element is pushed away from the front, unloads elastically, and then undergoes tensile plastic deformation in the directions tangential to the reaction front. The external surface of the lithiated silicon is subject to tensile hoop stress, possibly leading to fracture.

When the reaction front is curved, the crystalline silicon and the lithiated silicon form a core-shell structure (Figure 6.2b). As the reaction front advances, freshly lithiated silicon is added at the front, previously lithiated silicon recedes, and the shell enlarges. An element of lithiated silicon at the curved front initially undergoes compressive plastic deformation in the hoop directions. Upon subsequent lithiation of the core, the element is pushed away from the front, unloads elastically, and then deforms plastically in *tension* in the hoop directions. This process results in tensile hoop stress at the surface of the particle, possibly causing fracture. When the reaction front is curved, reaction and plasticity are concurrent,

but can occur at different places. There is no ambiguity in differentiating processes at the reaction front and plastic deformation inside the lithiated silicon.

We present a model of concurrent reaction and plasticity. Existing analyses of lithiation-induced deformation and fracture have assumed diffusion-limited lithiation.[91],[115],[129]-[136] In this chapter, motivated by experimental observations, we assume that the velocity of the reaction front is limited by the rate of the reaction of lithium and silicon at the front, rather than by the diffusion of lithium through the amorphous phase. We identify the driving force for the movement of the phase boundary, and accommodate the reaction-induced volumetric expansion by plastic deformation of lithiated silicon. The model is illustrated by an analytical solution of the co-evolving reaction and plasticity in a spherical particle. We show that lithiation may induce high enough stress to stall the reaction, and that fracture is averted if the particle is small and the yield strength of lithiated silicon is low.

6.2 A model of concurrent reaction and plasticity

Figure 6.1 illustrates an electrochemical cell, in which crystalline silicon and lithium react and form an amorphous phase of lithiated silicon:

$$\mathrm{Li} + \frac{1}{x}\mathrm{Si} = \frac{1}{x}\mathrm{Li}_x\mathrm{Si} \tag{6.1}$$

The two electrodes are connected through a conducting wire and an electrolyte. The conducting wire may be connected to an external voltage source. At the interface between the lithium electrode and the electrolyte, lithium atoms dissociate into lithium ions and electrons. Lithium ions pass through the electrolyte, and electrons

pass through the conducting wire. Since lithiated silicon is an electron conductor,[137] lithium ions and electrons recombine into lithium atoms upon reaching the silicon electrode. Lithium atoms then diffuse through the lithiated silicon, and react with the crystalline silicon—at the reaction front—to form fresh lithiated silicon. The reaction causes the lithiated silicon to grow at the expense of the crystalline silicon and metallic lithium.

Migration of lithium ions in the electrolyte is relatively fast, so that the diffusion of lithium through the lithiated silicon and the reaction between lithium and silicon at the front may limit the velocity of the reaction front. Let D be the diffusivity of lithium in the lithiated silicon, V the velocity of the reaction front, and L the thickness of the lithiated silicon. These quantities form a dimensionless group:

$$\chi = \frac{D}{VL}. \tag{6.2}$$

The parameter χ characterizes the relative rate of diffusion and reaction. If χ is large, the diffusion of lithium is fast, and lithiation is limited by the reaction. A representative value of diffusivity of lithium at room temperature in lithiated silicon is $D = 10^{-16} \text{m}^2/\text{s}$.[89] A reported velocity of the reaction front of the lithiation of a (100)-Si wafer is $V = 1.2 \times 10^{-11} \text{m/s}$.[124] We note that the reaction velocity may be dependent on the crystallographic directions.[125], [127] A systematic experimental study of such dependence will be discussed in Chapter 7. For rates of diffusion and reaction to be comparable, $\chi = 1$, and the thickness of the lithiated silicon is calculated to be $L = 8\mu m$. In typical nanostructured electrodes of silicon, the

feature size is less than a few hundreds of nanometers.[125]-[127] Thus, for electrodes at such size scales, the velocity of the reaction front is limited by the reaction of silicon and lithium at the front, rather than by the diffusion of lithium through the amorphous phase.

We next identify the driving force for the reaction, namely, the change in the free energy associated with the reaction that converts one lithium atom and $1/x$ silicon atoms into lithiated silicon. Let ΔG_r be the free energy of reaction (6.1) when both the stress and the applied voltage vanish. When the conducting wire is connected through a voltage source, associated with converting one lithium atom into lithiated silicon, one electron passes through the conducting wire, so that the external voltage source does work $e\Phi$, where Φ is the voltage, and e is the elementary charge (a positive quantity). The driving force is further modified when the two phases, the crystalline silicon and the lithiated silicon, are stressed. (The metallic lithium electrode is taken to be stress-free.) Associated with converting one lithium atom into lithiated silicon, the crystalline silicon phase loses $1/x$ number of silicon atoms, and the stress in silicon does work $-\sigma_m^{\mathrm{Si}}\Omega^{\mathrm{Si}}/x$, where σ_m^{Si} is the mean stress in the silicon at the reaction front, and Ω^{Si} is the volume per Si atom. The amorphous phase gains $1/x$ silicon atoms and one lithium atom, so that the stress in the amorphous phase does work $\sigma_m^{\mathrm{Li_xSi}}\Omega^{\mathrm{Li_xSi}}/x$, where $\sigma_m^{\mathrm{Li_xSi}}$ is the mean stress in the amorphous phase at the reaction front, and $\Omega^{\mathrm{Li_xSi}}$ is the volume per unit of $\mathrm{Li_xSi}$.

Combining the above contributions, we find that, when the reaction advances

by converting one lithium atom and $1/x$ silicon atoms into lithiated silicon, the net change in the free energy is

$$\Delta G = \Delta G_r - e\Phi + \frac{1}{x}\left(\sigma_m^{\mathrm{Si}}\Omega^{\mathrm{Si}} - \sigma_m^{\mathrm{Li_xSi}}\Omega^{\mathrm{Li_xSi}}\right). \tag{6.3}$$

We have neglected the dissipation at electrolyte/electrode interfaces, as well as inside the electrodes and electrolytes. In our sign convention, a negative ΔG drives lithiation, and a more negative value represents a larger driving force. The free energy of reaction ΔG_r takes a negative value. In Figure 6.1, we have drawn the polarity of the voltage source in the direction that drives lithiation. As expected, a compressive mean stress in the crystalline silicon promotes lithiation, whereas a compressive mean stress in the lithiated silicon retards lithiation.

This net change in the free energy is the driving force for the movement of the reaction front. The velocity of the reaction front will increase as the magnitude of the driving force increases. The reaction is taken to be thermally-activated, described by the familiar kinetic model:[138]

$$V = V_0 \exp\left(-\frac{Q}{kT}\right)\left[\exp\left(-\frac{\Delta G}{kT}\right) - 1\right], \tag{6.4}$$

where kT is the temperature in the unit of energy, Q is the activation energy, and V_0 is a parameter analogous to the exchange current density in a redox process. The velocity of the reaction is taken to be positive when the crystalline silicon is consumed and the lithiated silicon grows. When $\Delta G = 0$, the electrochemical cell is in equilibrium, and the reaction halts, $V = 0$. When $\Delta G < 0$, the reaction front advances in the direction that consumes crystalline silicon, $V > 0$. When $\Delta G > 0$, it may seem that the reverse reaction would take place—the lithiated phase would be

consumed, silicon re-deposited at the reaction front, and lithium redeposited as lithium metal. The reaction front would move in the direction opposite as that during lithiation. However, experiments have suggested that during delithiation ($\Delta G > 0$), the phase boundary remains stationary as lithium is removed from the amorphous layer.[124] Thus, the forward and backward reactions seem to involve distinct kinetic processes. Such complication should be considered in describing an accurate kinetic model. Nevertheless, in the case of $|\Delta G| >> kT$, as is common in these systems at room temperature, the forward reaction is more prominent than the backward one. Thus, the kinetics model of Equation (6.4), based on transition state theory, is still approximately valid. In the following sections, we calculate the stress field and simulate the morphology of lithiated silicon with a prescribed velocity field. The considerations in Equations (6.3) and (6.4) may aid the planning of future experiments.

Associated with the reaction (6.1), the volume of the silicon electrode expands by the ratio

$$\beta = \frac{\Omega^{Li_xSi}}{\Omega^{Si}}. \tag{6.5}$$

The lithiation-induced expansion is too large to be accommodated by elastic deformation; rather, the large lithiated-induced expansion is accommodated by plastic deformation of the lithiated silicon.[91], [115] The concurrent reaction and plasticity evolve a field of stress in both crystalline and lithiated silicon. The reaction front is atomically sharp, the amorphous phase attains the fully lithiated state, and the crystalline silicon core remains free of lithium. The crystalline silicon is

modeled as an elastic material, and the lithiated silicon is modeled as an elastic-plastic material. The elastic-plastic model can be found in the classic text of Hill.[88]

The models of reaction kinetics and elastic-plastic deformation, in combination, co-evolve the reaction front and elastic-plastic field. At a given time, the location of the reaction front and the elastic-plastic field are known. For a small increment in time, advance the reaction front by an amount following the kinetic model, and then accommodate the reaction-induced volumetric expansion by updating the elastic-plastic field. Repeat the procedure to trace the co-evolution incrementally in time.

6.3 Lithiation of a spherical particle of crystalline silicon

To illustrate the salient features of the model, we derive an analytical solution for a spherical particle. A particle of pristine crystalline silicon, radius *B*, is taken to be the reference configuration (Figure 6.3a). The velocity of the reaction front is taken to be the same everywhere on the front, so that the front remains to be a spherical surface as it advances, and the spherical symmetry is retained. The magnitude of the velocity, however, may change as the reaction progresses. At time *t*, Figure 6.3b, the particle becomes a core-shell structure, with the radius of the crystalline core being A, and the outer radius of the amorphous shell being $b(t)$. The function $A(t)$ specifies the extent of reaction, and the velocity of the reaction front is $V = -dA(t)/dt$. In the reference configuration, an element of crystalline

silicon is identified by the radius R. At time t, this element is lithiated and moves to a place of radius r. The function $r(R,t)$ specifies the field of deformation. In representing a field, we may choose either R or r as an independent variable. One variable can be changed to the other by using the function $r(R,t)$. We will indicate our choice in each field explicitly when the distinction is important.

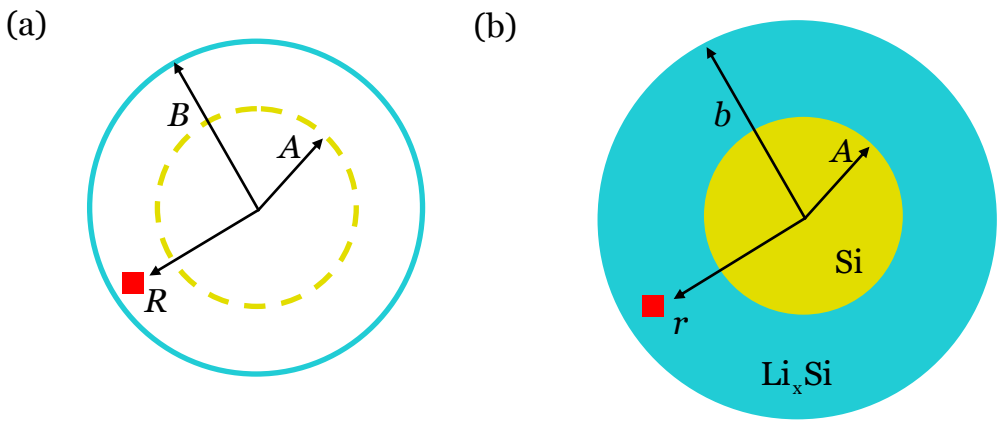

Figure 6.3. Lithiation of a spherical particle of crystalline silicon. (a) The pristine crystalline silicon, radius B, is taken as the reference configuration, in which a spherical surface is marked by the radius A, and an element of silicon by the radius R. (b) At time t, silicon in the shell outside the radius A is lithiated, and the element R moves to a new position of radius r.

Elastic strain is much smaller than the volumetric strain associated with the phase transition. To focus on the main ideas, we neglect elastic strains of both phases, and model the crystalline silicon as a rigid material, and the lithiated silicon as a rigid-plastic material. Consequently, the expansion of the particle is entirely due to lithiation. Consider the shell of the lithiated silicon between the radii A and r. This shell is lithiated from a shell of the pristine crystalline silicon between the radii A and R. The ratio of the volume of the lithiated shell over the volume of the crystalline shell is β, so that

$$r^3 - A^3 = \beta\left(R^3 - A^3\right). \tag{6.6}$$

This equation gives the function $r(R,t)$ once the function $A(t)$ is given. That is, $A(t)$ fully specifies the kinematics of the spherical particle. In particular, the outer radius of the lithiated silicon is obtained by setting $R = B$ in (6.6):

$$b = \left[A^3 + \beta\left(B^3 - A^3\right)\right]^{1/3}. \tag{6.7}$$

The radial and hoop stretches can be calculated from

$$\lambda_r = \frac{\partial r(R,t)}{\partial R}, \quad \lambda_\theta = \frac{r(R,t)}{R}. \tag{6.8}$$

The crystalline core is in a state of homogeneous hydrostatic compression. The stress field in the amorphous shell, however, is inhomogeneous. Each material element in the shell is subject to a state of triaxial stresses. Let σ_r be the radial stress, and σ_θ the hoop stress (Figure 6.4a). We adopt a commonly used idealization that plastic deformation is unaffected when a hydrostatic stress is superposed. Superposing a hydrostatic stress of magnitude σ_r, we observe that the state of plastic deformation of the element subject to the triaxial stresses is the same as the state of the plastic deformation of the element subject to equal biaxial stresses, $\sigma_\theta - \sigma_r$.

Figure 6.4b sketches the stress-stretch relation in terms of the stress $\sigma_\theta - \sigma_r$ and the strain $\log\lambda_\theta$. For simplicity, the yield strength of the lithiated phase, σ_Y, is taken to be constant, independent of the amount of deformation and the concentration of lithium. An element of newly lithiated silicon is compressed in the hoop directions, and is in the state $\sigma_\theta - \sigma_r = -\sigma_Y$. Subsequently, this material element is pushed outward by even newer lithiated silicon, and undergoes elastic

unloading. Because the elastic strain is negligible compared to lithiation-induced strain, the elastic unloading is represented by the vertical line in Figure 6.4b. After elastic unloading, an element plastically deforms under $\sigma_\theta - \sigma_r = +\sigma_Y$.

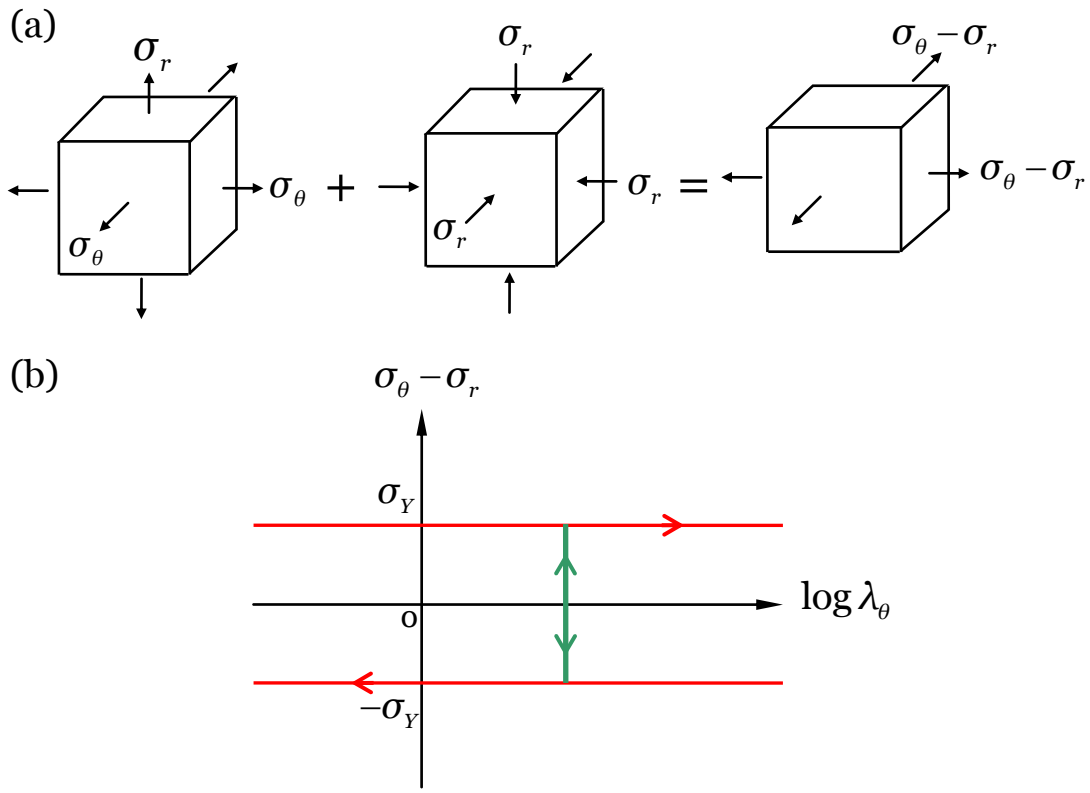

Figure 6.4. (a) The state of plastic deformation of an element subject to the triaxial stresses $(\sigma_r, \sigma_\theta, \sigma_\theta)$ is the same as that of an element subject to equal-biaxial stresses $\sigma_\theta - \sigma_r$. (b) The stress-strain relation in terms of the stress $\sigma_\theta - \sigma_r$ and the strain $\log \lambda_\theta$. When $\sigma_\theta - \sigma_r = +\sigma_Y$, the plastic deformation is tensile in the hoop direction. When $\sigma_\theta - \sigma_r = -\sigma_Y$, the plastic deformation is compressive in the hoop direction. The elastic strain is negligible compared to lithiated strain, so that elastic part of the stress-strain relation is represented by a vertical line.

The balance of forces acting on a material element requires that

$$\frac{\partial \sigma_r(r,t)}{\partial r} + 2\frac{\sigma_r(r,t) - \sigma_\theta(r,t)}{r} = 0. \tag{6.9}$$

Setting $\sigma_\theta - \sigma_r = \sigma_Y$ in (6.9) and integrating over r with the traction-free boundary

condition, $\sigma_r(b,t)=0$, we obtain the radial stress in the shell:

$$\sigma_r = -2\sigma_Y \log(b/r), \quad A \le r \le b. \tag{6.10}$$

The hoop stress inside the shell, away from the reaction front, is determined from $\sigma_\theta - \sigma_r = \sigma_Y$, giving

$$\sigma_\theta = \sigma_Y - 2\sigma_Y \log(b/r), \quad A < r \le b. \tag{6.11}$$

As discussed above in connection with Figure 6.2, in the shell at the reaction front, the element of the freshly lithiated silicon undergoes plastic deformation, which elongates the element in the radial direction. The hoop stress in the element of freshly lithiated silicon is determined from $\sigma_\theta - \sigma_r = -\sigma_Y$, giving

$$\sigma_\theta = -\sigma_Y - 2\sigma_Y \log(b/A), \quad r = A. \tag{6.12}$$

A comparison of (6.11) and (6.12) indicates a jump in the hoop stress by magnitude $2\sigma_Y$. This jump is caused by our neglecting the elastic strain. Should we include elastic strain, the hoop stress would make a transition from (6.12) to (6.11) within a very thin shell.

As mentioned above, the core is in a state of homogeneous and hydrostatic compression. In order to balance forces, the radial stress is continuous across the reaction front. Setting $r = A$ in (6.10), we obtain the stress field in the crystalline core:

$$\sigma_r = \sigma_\theta = -2\sigma_Y \log(b/A), \quad r \le A. \tag{6.13}$$

For illustration, Figure 6.5 plots the stress field when the reaction front is at $A/b = 0.4$. As expected, the core is in a homogeneous state of hydrostatic compression, but the stress field in the shell is triaxial and inhomogeneous. The

radial stress in the shell is compressive, with $\sigma_r(b,t)=0$ prescribed as the boundary condition. Because of the triaxial state of stress, the magnitude of the stress component readily exceeds the yield strength. The hoop stress is tensile at the external surface of the particle, $\sigma_\theta(b,t)=\sigma_Y$, and gradually becomes compressive inside the shell. Near the reaction front, the hoop stress jumps by amplitude $2\sigma_Y$, as previously discussed.

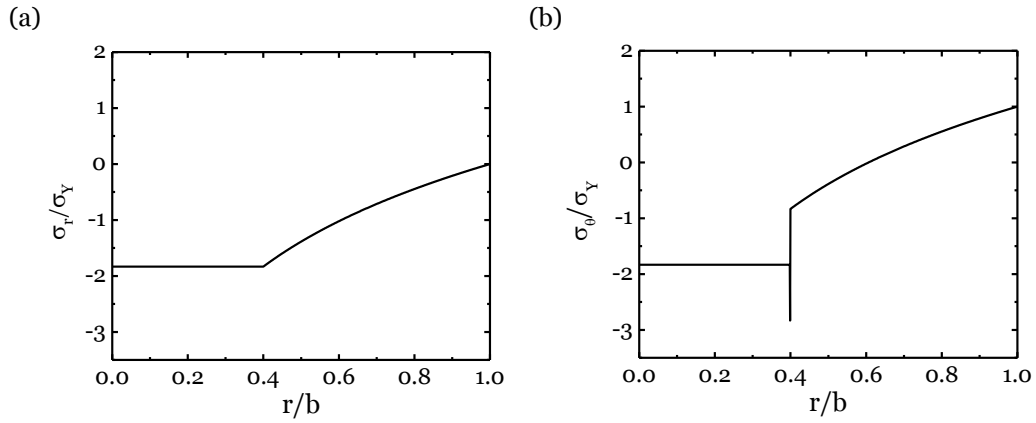

Figure 6.5. Stress field in a spherical particle when the reaction front is at $A/b=0.4$. (a) radial stress, (b) hoop stress.

For the spherical particle, the field of stress and the field of deformation are fully determined once the radius of the core *A* is specified. We now examine how the stress affects the movement of the reaction front. The mean stress in the crystalline silicon is $\sigma_m^{\mathrm{Si}}=-2\sigma_Y\log(b/A)$. At the reaction front, the mean stress in the lithiated silicon is $\sigma_m^{\mathrm{Li_xSi}}=-2\sigma_Y\log(b/A)-2\sigma_Y/3$. Inserting these expressions into (6.3), we obtain the driving force for the movement of the reaction front:

$$\Delta G=\Delta G_r-e\Phi+\frac{2\sigma_Y\Omega^{\mathrm{Si}}}{x}\left[(\beta-1)\log\left(\frac{b}{A}\right)+\frac{\beta}{3}\right]. \tag{6.14}$$

The contribution due to the stresses is plotted in Figure 6.6, where the horizontal axis

is the normalized radius of the crystalline core A/b. In making this plot, we have adopted the following values: $\beta = 4$,[17] $x = 3.75$,[124] $\sigma_Y = 1\text{GPa}$,[117] and $\Omega^{\text{Si}} = 2.0\times10^{-29}\,\text{m}^3$.[92] As expected, the contribution due to the stresses is positive and retards lithiation. The magnitude of the contribution increases as the crystalline core shrinks. Recall that the free energy of formation of lithiated silicon is small; for example, $\Delta G_r = -0.18\text{eV}$ for amorphous $Li_{2.1}Si$.[120] Consequently, the reaction can readily generate large enough stress to completely counteract the electrochemical driving force, stalling the reaction. We note that the free energy of reaction, ΔG_r, differs for amorphous Li-Si phases with various Li concentrations; the experimental data on such functional dependence is unavailable to date.

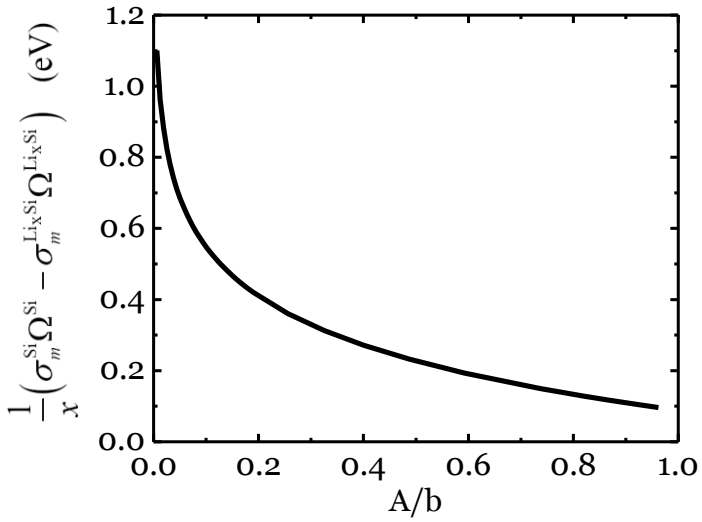

Figure 6.6. The contribution of the stress to the driving force of lithiation is plotted as a function of the normalized radius of the core.

The curvature of the electrode plays a key role in this contribution of the stress to the free energy. To illustrate this point, consider a flat crystalline silicon electrode. In the initial stages of lithiation, the amorphous phase exists as a thin

film on a crystalline silicon substrate. As previously mentioned, the biaxial stress in the freshly lithiated silicon is at the compressive yield strength. The stress in the crystalline silicon is zero. Using the same representative values as for the spherical particle, the contribution from the stress to the free energy in (6.3) is 0.089eV. As with the spherical particle, in a thin film, the stresses retard lithiation. However, the value of this contribution is small compared to the values found for the spherical particle (Figure 6.6) and does not vary with the extent of lithiation. Hence, we predict that the curvature can greatly influence the rate of lithiation of crystalline silicon.

6.4 Reaction-induced fracture

We now analyze reaction-induced fracture using an approach similar to that described in several recent papers.[11], [12], [91] We focus on fracture caused by the tensile hoop stress during the lithiation of a spherical particle of crystalline silicon. A circumferential crack, depth d, is assumed to preexist in the particle, as illustrated in Figure 6.7. We ask if the lithiation-induced stress will cause the crack to grow. The propagation of the crack, should it occur, is assumed to be a much faster process than the plastic flow. Consequently, in analyzing fracture, we assume that no further plastic deformation occurs during the propagation of the crack, and we adopt linear elastic fracture mechanics. The reduction in the elastic energy associated with the crack advancing a unit area defines the energy release rate, G. Dimensional analysis dictates that the energy release rate should take the form

$$G = Z\frac{\sigma_Y^2}{E}b, \tag{6.15}$$

where E is Young's modulus, and Z is a dimensionless number to be determined by solving the elastic boundary-value problem. At a given time, once the location and the depth of the crack are given, Z is uniquely determined. For the lithiation of a spherical particle, the energy release reaches the maximum value when the particle is fully lithiated, and the length of the crack equals the size of the regime where the hoop stress is tensile, $d/b = 0.395$. Therefore, the calculation gives a conservative critical particle size to avoid fracture. We use the commercial finite-element software ABAQUS to calculate the energy release rate. In the simulation, we input the stress distribution at the fully lithiated state, and the J-integral is used to calculate the energy release rate. Our calculation gives $Z = 0.91$.

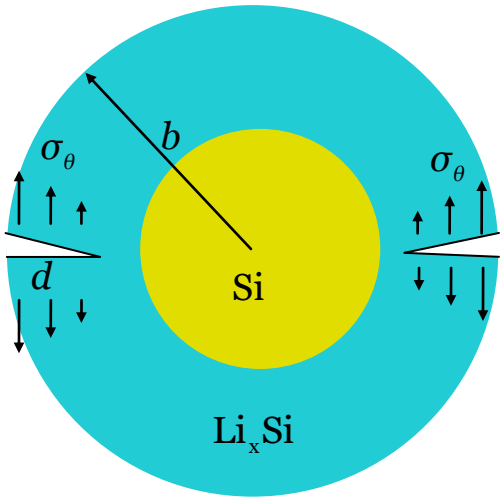

Figure 6.7. A pre-existing circumferential crack in a spherical particle of electrode.

Let Γ be the fracture energy of the particle. No pre-existing flaws will advance if the maximum energy release rate is less than the fracture energy. Thus, (6.15) defines a critical particle size:

$$b_{cr} = \frac{\Gamma E}{Z\sigma_Y^2}. \tag{6.16}$$

When the size of the particle is below this critical value, fracture is averted. As a result, fracture is averted if the particle is small and the yield strength is low. Taking representative values, $\Gamma = 10\ \mathrm{J/m^2}$,[91] $E = 35\ \mathrm{GPa}$, and $\sigma_Y = 1\ \mathrm{GPa}$,[82] we find that the critical radius for fully lithiated silicon is $b_{cr} = 380\ \mathrm{nm}$. The corresponding critical radius of the pristine crystalline silicon is thus $B_{cr} = 239\ \mathrm{nm}$.

6.5 Summary

Crystalline silicon and lithium react to form lithiated silicon. The reaction front is located at the atomically sharp phase boundary between the crystalline silicon and lithiated silicon. The reaction generates a large volumetric expansion, which is accommodated by plastic deformation in the lithiated silicon. This chapter describes a model that co-evolves the reaction front and plastic deformation. The velocity of the reaction front is related to the change in the free energy through a kinetic model, while the stress field is evolved according to the elastic-plastic theory. The model is illustrated with the lithiation of a spherical particle of crystalline silicon. We show that fracture is averted when the particle is small and the yield strength of lithiated silicon is low. It is hoped that model will aid in the planning of future experiments and atomistic simulations.

Chapter 7

Kinetics of the Initial Lithiation of Crystalline Silicon Electrodes

7.1 Introduction

As mentioned in Chapter 6, numerous nanostructured electrodes have been fabricated from crystalline silicon. During the initial lithiation process, crystalline silicon and lithium react at room temperature, forming an amorphous phase of lithiated silicon.[79],[122],[124]-[127],[137],[139]-[142] First-principles calculations have revealed many atomic details of this phase transformation.[137],[139] Likewise, various experimental techniques have provided insight into this amorphization process.[122],[140]-[142] For example, Chon, et al. have demonstrated that the phase boundary between {100} crystalline silicon and amorphous lithiated silicon is atomically sharp.[124] Additionally, Liu, et al. have observed that under a constant potential the motion of the phase boundary between crystalline silicon and amorphous lithiated silicon is linear in time along the [112] direction.[125] This latter experiment indicates that the rate of lithiation is not limited by diffusion through the lithiated phase but instead by short-range atomic processes at the phase boundary. These processes include breaking Si-Si bonds and forming Li-Si bonds. Further evidence of this phenomenon was provided by the observation of lithiated silicon of anisotropic morphologies, which suggest that the reaction at the phase boundary is fastest in the <110> direction of crystalline silicon.[125]-[127] In Chapter 6, we

proposed that the observed anisotropic morphologies are due to the variation in the short-range atomic processes at the reaction fronts in different crystallographic orientations.[143] A similar theoretical analysis was proposed by Yang et al.[144] In general, any of a number of kinetic processes may be rate-limiting or multiple kinetic processes can significantly contribute to the overall kinetics of lithiation. Moreover, experimental measurements of varying phase boundary velocities for different crystallographic orientations are lacking.

To provide insight into the pertinent kinetic processes, in this chapter, we present an experimental study quantifying the kinetics of the initial lithiation of crystalline silicon. Crystalline silicon wafers of {100}, {110}, and {111} orientations were lithiated at various currents, and the response of the potential was measured. To interpret these data, we have constructed a kinetic model that considers three kinetic processes in series: the redox reaction at the electrolyte/lithiated silicon interface, the diffusion of lithium through the lithiated phase, and the chemical reaction at the lithiated silicon/crystalline silicon interface. Using this model and experimental data, we can determine which kinetic processes are the most important. In particular, from our experiments, we can quantify the rates of reactions at the interfaces as a function of crystal orientation. Additionally, we can provide a lower bound on the diffusivity of lithium through the lithiated silicon phase. Using the measured reaction rates, we have implemented a model of concurrent reaction and plasticity into the finite element software ABAQUS. This simulation accurately predicts anisotropic morphological evolution and anisotropic fracture during initial

lithiation of crystalline silicon nanopillars of various axial orientations.

7.2 Experimental procedure

Silicon wafers of three orientations – {100}, {110}, and {111} – were used as the working electrodes. The wafers were all doped with phosphorous and had similar and low resistivity $(5-10\ \Omega-\text{cm})$. Due to the low resistivity, the maximum Ohmic drop in potential through the thickness of the wafer was calculated to be less than $50\ \mu\text{V}$ for the current densities used in these experiments. The {100} and {110} wafers were $500\ \mu\text{m}$ thick, and the {111} wafer was $250\ \mu\text{m}$ thick. The wafers were cut into $6\text{cm} \times 1\text{cm}$ sections.

The samples were cleaned with acetone and isopropanol. Next, they were placed into a sputter deposition system (AJA Int. ATC 1800). All sputtering targets used had a $50.8\ \text{mm}$ diameter, and depositions were performed at room temperature $\left(22^{\circ}\text{C}\right)$. First, the samples were plasma-cleaned in Ar at 20 mTorr and 24 W (RF) for 5 minutes. Then, a 50 nm thick layer of Ti was deposited – 3 mTorr of Ar at 100 W (DC) for 5 minutes, followed by a 250 nm layer of Cu – 5 mTorr of Ar at 200 W (DC) for 12.5 minutes. These layers serve as the current collector. On top of these layers, 500 nm of Si_3N_4 was deposited using plasma-enhanced chemical vapor deposition (Nexx Cirrus 150 PECVD) to prevent electrochemical reaction of Li with the Cu and Ti layers. During PECVD, a small region of the Cu layer was masked to allow for electrical contact with the electrode. It was observed in control experiments that no significant electrochemical signal was produced for an

electrode coated with 500 nm of Si_3N_4; thus, the nitride served its purpose as a passivating layer.

Electrochemical cells were assembled in a glove box (Vacuum Atmospheres HE-43) in an ultra-high purity Ar atmosphere with less than 0.1 ppm moisture content. The Si wafer was incorporated as the working electrode into a homemade three-electrode electrochemical cell with lithium foil used as the counter and reference electrodes. 1 M $LiPF_6$ in 1:1 (vol%) ethylene carbonate (EC) : diethyl carbonate (DEC) was used as the electrolyte (Novolyte Technologies). The cells were hermetically sealed inside the glove box using paraffin wax and tested using a VersaSTAT 3 potentiostat (Princeton Applied Research) outside of the glove box. The wafers were initially lithiated at a constant current density of $12.5\ \mu A/cm^2$ for five hours followed by four other current densities: $6.25\ \mu A/cm^2$, $25\ \mu A/cm^2$, $50\ \mu A/cm^2$, and $100\ \mu A/cm^2$ applied in random order for one hour each with a 30 minute open-circuit segment between each imposed current density. To observe time-dependent effects in the experiments, all five current densities were then applied again (also in random order) for 30 minutes each. Finally, an open-circuit segment was applied for 30 minutes. For each sample, the two values of the measured potential corresponding to each current density were observed to be quite similar (usually within 1 mV), demonstrating that the results are quite reproducible. In other words, it does not seem that a time-dependent process such as continuous growth of the solid electrolyte interphase affects the measured potentials in a time-dependent manner. It is possible that the effect of the SEI is minimized

because most of the growth may occur during the initial five-hour current segment. Still, it is important to note that the SEI will form during this experiment. This growth process may be different from cell to cell and may be one source of variation in the measured potentials from sample to sample. Additionally, it has been shown that below a potential of about 50 mV vs. Li/Li+, amorphous $Li_{\eta}Si$ transforms to crystalline $Li_{3.75}Si$.[145] Thus, in an attempt to avoid this amorphous to crystalline phase transformation, the applied currents were selected such that the potential is maintained above 50 mV vs. Li/Li^{+}.

To image the phase boundary, the samples were removed from the cell in the glove box, rinsed in DEC, dried, and broken into fragments. These fragments were sealed in a container in the glove box and immediately transferred to the SEM chamber. It was estimated that they were exposed to air for less than two minutes during the transfer process.

7.3 Experimental results

Figure 7.1 shows a typical response of the potential to a series of applied currents for a {110} Si wafer. When a certain constant level of current density is applied for some duration of time, the measured potential of Si vs. Li/Li^{+} reaches a particular value very quickly and remains at this value for the remainder of the time. The measured potential provides information about the concentration of lithium in the electrode at the interface with the electrolyte. For two-phase coexistence, lithium insertion is accommodated by the growth of the lithium-rich phase at the

expense of the lithium-poor phase. As a result, the concentration in the electrode at the interface with the electrolyte is fixed, rendering the potential constant in time for a constant current density. These two-phase plateaus are evident for all three tested orientations (Figure 7.1, B.1, B.2), suggesting the coexistence of crystalline silicon $\left(\text{c-Si}\right)$ and amorphous lithiated silicon $\left(\text{a-Li}_{\eta}\text{Si}\right)$ for all three orientations. This result agrees in part with a previous work, in which the boundary separating these two phases has been found to be atomically sharp for a {100} wafer.[124]

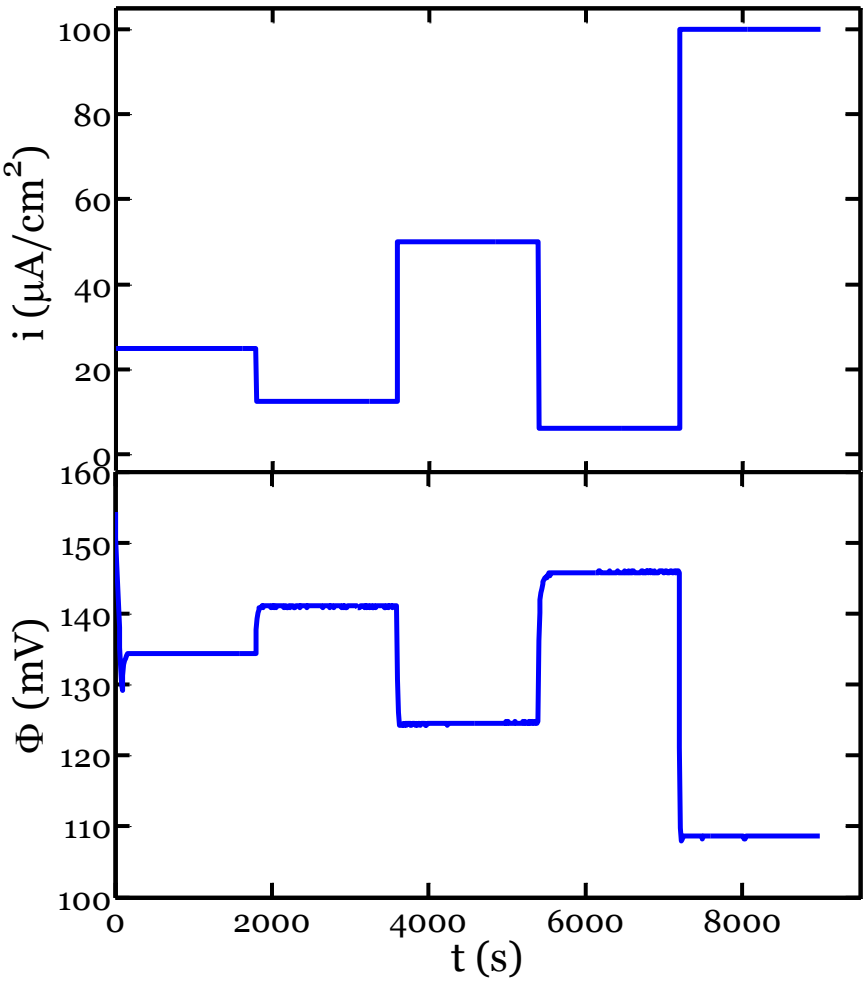

Figure 7.1. Typical sequence of applied current density, i, and measured response of the potential vs. Li/Li$^+$, Φ, for a {110} Si wafer.

Figure 7.2 shows the measured plateau potentials as a function of the applied current density for all of the samples. The solid symbols represent the mean of three samples for the given crystallographic orientation, and the error bars represent ± 1 standard deviation from the mean. The variation from sample to sample is quite small, demonstrating the reproducibility of the experiment.

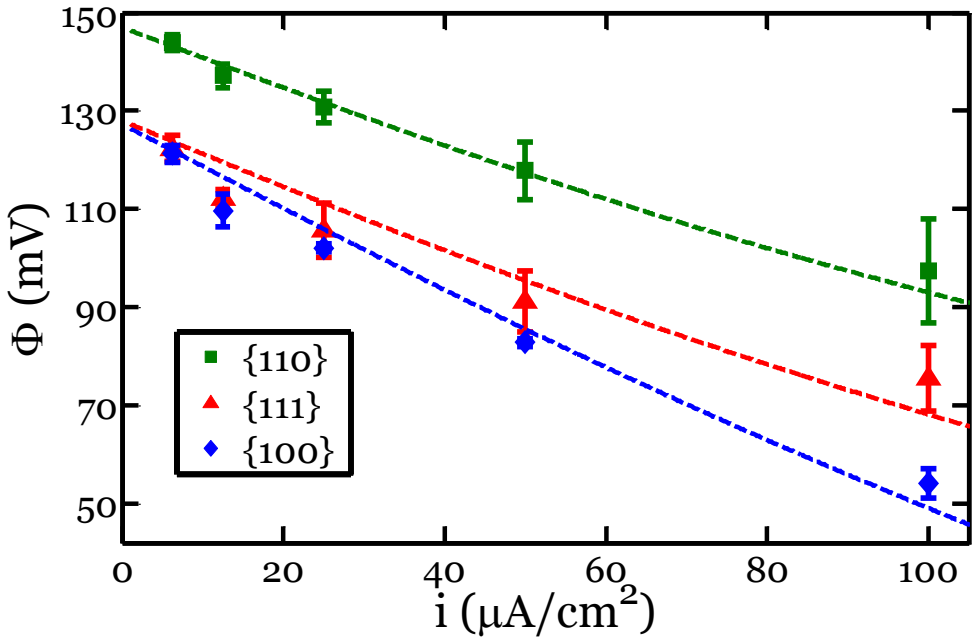

Figure 7.2. Measured potential vs. Li/Li^+, Φ, as a function of applied current density, i for all three orientations. The solid symbols represent the mean of the tested samples, and the error bars represent ± 1 standard deviation from the mean. The dashed lines represent fits from the kinetic model.

Although Si transforms to numerous Li-Si crystalline phases at elevated temperatures,[90] it has been shown that electrochemical lithiation of Si at room temperature results in a metastable amorphous $Li_\eta Si$ phase, where $\eta \approx 3.5$.[145] It is likely that this phase exists over a finite range of lithium concentrations depending on the applied potential. However, assuming a composition of $Li_{3.5}Si$ and

accounting for the corresponding volume expansion $\beta = \Omega_{Li_{3.5}Si} / \Omega_{Si} = 3.21$,[146] we have calculated the expected thickness for the current history corresponding to these experiments. These predicted thicknesses were then compared to the measured thicknesses using the SEM, and the values were in good agreement. Evidently, the velocity of the phase boundary is directly correlated with the applied current density. Hence, in our experiments one can think of the current density, e.g. the horizontal axis in Figure 7.2, as the velocity of the moving phase boundary. Thus, Figure 7.2 shows that the {110} Si wafers are the "fastest" for a given potential. For instance, at 120 mV vs. Li/Li^+, the interpolated average current densities for the {110}, {100}, and {111} Si wafers are $47.1\ \mu A/cm^2$, $7.4\ \mu A/cm^2$, and $7.7\ \mu A/cm^2$, respectively. Such discrepancy in the velocities has important ramifications for lithiation of crystalline silicon structures with various crystal facets exposed. For instance, these measurements of varying phase boundary velocities can accurately account for anisotropic morphologies and fracture patterns developed in crystalline silicon nanopillars of various axial orientations, as will be discussed in Section 7.6.

7.4 A kinetic model of coupled redox reaction, diffusion, and chemical reaction

Figure 7.3 illustrates an electrochemical cell, in which crystalline silicon and metallic lithium react and form an amorphous phase of lithiated silicon:

$$(\eta + \delta)\mathrm{Li} + \mathrm{Si} = \mathrm{Li}_{\eta+\delta}\mathrm{Si}. \tag{7.1}$$

The two electrodes are connected through a conducting wire and an electrolyte. The

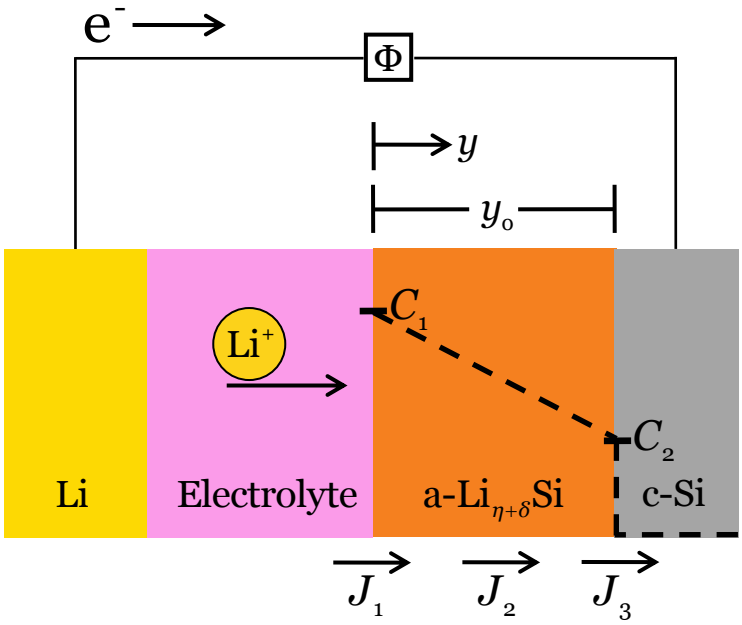

Figure 7.3. In an electrochemical cell, crystalline silicon and lithium react at room temperature, forming an amorphous phase of lithiated silicon. The concentrations C_1 and C_2 represent the concentration of lithium in the lithiated silicon phase at the given interfaces. The dashed line represents the variation of the concentration of lithium as a function of position in the Si electrode. The position in the lithiated phase is denoted by y and the total thickness of the layer by y_0. The J_i denote the fluxes of lithium at various positions: J_1 at the interface between the electrolyte and the lithiated silicon phase, J_2 in the lithiated silicon phase, J_3 at the phase boundary between lithiated silicon and crystalline silicon.

conducting wire may be connected to an external voltage source. At the interface between the metallic lithium electrode and the electrolyte, lithium atoms dissociate into lithium ions and electrons. Lithium ions pass through the electrolyte while electrons pass through the conducting wire. Upon reaching the silicon electrode, lithium ions and electrons recombine into lithium atoms. We expect that this latter process occurs at the interface between the electrolyte and the a-$Li_\eta Si$, as the silicon samples have fairly large electric conductivity (Section 7.2) and lithiated silicon has even larger conductivity because of its metallic-like properties.[137],[146] Lithium atoms then diffuse through the lithiated silicon and react with the crystalline

silicon—at the reaction front—to form fresh lithiated silicon, $\text{a-Li}_\eta\text{Si}$. This process at the $\text{c-Si} / \text{a-Li}_\eta\text{Si}$ interface involves breaking of silicon-silicon bonds and formation of lithium-silicon bonds. Overall, this lithiation process causes lithiated silicon to grow at the expense of the crystalline silicon and metallic lithium.

We now propose a model to quantify the relationship between the measured potential and the applied current density, accounting for the motion of the phase boundary. To do so, we adopt a modified version of the Deal-Grove model for thermal oxidation of c-Si.[147] In the model, the concentration of lithium in the lithiated phase is a function of position, y (Figure 7.3). We take the reference state as that of amorphous lithiated silicon of a given composition— Li_ηSi —in metastable "equilibrium" with crystalline silicon. In the current state, the composition becomes $\text{Li}_{\eta+\delta}\text{Si}$, where δ is a function of position y in the silicon electrode.

Lithiation is driven by the externally applied voltage or current density, and involves three kinetic processes: the redox reaction at the electrolyte/ $\text{a-Li}_\eta\text{Si}$ interface, the diffusion of lithium through the $\text{a-Li}_\eta\text{Si}$ phase, and the reaction at the $\text{a-Li}_\eta\text{Si}$ /c-Si interface. The three kinetic processes are concomitant and are in series: any of these processes may be rate-limiting or they may occur at comparable rates such that multiple processes govern the lithiation process.

Associated with the redox reaction, $\text{Li}^+ + e^- = \text{Li}$, we take the flux through the electrolyte/ $\text{a-Li}_\eta\text{Si}$ interface, J_1, as given by the Butler-Volmer equation:

$$J_1 = \frac{i_0}{q}\left[\exp\left(-\frac{\alpha F}{RT}\left[\Phi - \Phi_{eq}{}^{curr}\right]\right) - \exp\left(\frac{[1-\alpha]F}{RT}\left[\Phi - \Phi_{eq}{}^{curr}\right]\right)\right], \qquad (7.2)$$

where i_0 is the exchange current density, q is the elementary charge, α is the

charge transfer coefficient, F is Faraday's constant, R is the ideal gas constant, T is the temperature, Φ is the potential of the electrode (i.e., the measured voltage), and Φ_{eq}^{curr} is the equilibrium potential in the current state, corresponding to the lithium concentration in the electrode near the electrolyte/ a-$Li_\eta Si$ interface. Henceforth, we will use $\alpha = 1/2$ for simplicity.

In the lithiated phase, $\eta + \delta$ is the number of lithium atoms hosted by each silicon atom. We regard η as a constant and δ as a small deviation, $\delta << \eta$. As a result, the diffusion of lithium atoms in the lithiated silicon phase is driven by the position-dependence of the composition, $\delta(y)$. Let C be the concentration of lithium in the lithiated phase (i.e., the amount of lithium per unit volume of the lithiated phase). The concentration of lithium in this phase relates to the composition by $C = (\eta + \delta)/\Omega_{Li_\eta Si}$, where $\Omega_{Li_\eta Si}$ is the atomic volume of the lithiated phase. We take the flux, J_2, to be driven by the gradient in the concentration of lithium through the thickness of the lithiated silicon:

$$J_2 = -D\frac{\partial C}{\partial y}, \tag{7.3}$$

where D is the diffusivity of lithium in the lithiated silicon. Because $\delta << \eta$, D is taken to be a constant, independent of the concentration. In the steady state, the flux is independent of the position, and the concentration varies linearly in the position, so that $J_2 = D(C_1 - C_2)/y_0$, where C_1 is the concentration of lithium in the lithiated silicon at the interface between the electrolyte and the lithiated silicon, C_2 is the concentration of lithium in the lithiated silicon at the interface between the lithiated silicon and crystalline silicon phases, and y_0 is the thickness of the

lithiated silicon.

At the interface between the lithiated silicon and the crystalline silicon phases, a chemical reaction occurs, as given by Equation (7.1). The reaction is driven by the excess lithium δ_2 in the lithiated silicon at this interface. The rate of reaction controls the flux of lithium across the interface, and we take the corresponding lithium flux to be given by the first-order relation:

$$J_3 = k\frac{\delta_2}{\Omega_{\mathrm{Li}_\eta\mathrm{Si}}}, \tag{7.4}$$

where k is the rate of the reaction.

Using the Nernst equation, we can relate the equilibrium potential $\Phi_{eq}^{\ curr}$ to the excess lithium δ_1 in the lithiated silicon at the interface with the electrolyte:

$$\Phi - \Phi_{eq}^{\ curr} = \Phi - \Phi_{eq}^{\ ref} + \frac{RT}{F}\left[\frac{\delta_1}{\eta(\eta+1)}\right], \tag{7.5}$$

where $\Phi_{eq}^{\ ref}$ is the equilibrium potential of a-$\mathrm{Li}_\eta\mathrm{Si}$ in the reference state $(\delta = 0)$.

With Equations (7.2) – (7.5), we can derive a relation between the applied current density, i, and the measured potential, Φ, in the steady state. For the full derivation of this relation, please see Appendix B.2. The result of this derivation is:

$$\frac{i}{i_0} = 2\sinh\left\{-\frac{F}{2RT}\left(\Phi - \Phi_{eq}^{\ ref} + \frac{RT}{F}\left[\frac{\Omega_{\mathrm{Li}_\eta\mathrm{Si}}}{q\eta(\eta+1)}\left(1+\frac{ky_0}{D}\right)\frac{1}{k}i\right]\right)\right\}. \tag{7.6}$$

It is important to note that there are three intrinsic time scales in this model: $qy_0\eta/i_0\Omega_{\mathrm{Li}_\eta\mathrm{Si}}$, $y_0^{\,2}/D$, and y_0/k, associated with the electrolyte/electrode surface reaction, the diffusion through the a-$\mathrm{Li}_\eta\mathrm{Si}$ layer, and the reaction at the a-$\mathrm{Li}_\eta\mathrm{Si}$/c-Si interface. There is also a time scale $qy_0\eta/i\Omega_{\mathrm{Li}_\eta\mathrm{Si}}$ associated with the applied current density. These four time scales form three dimensionless groups:

$i_o\Omega_{Li_\eta Si}/kq\eta$, ky_o/D, and i/i_o. The parameter ky_o/D characterizes the relative rates of reaction at the a-$Li_\eta Si$/c-Si interface and diffusion through the a-$Li_\eta Si$ phase. If $ky_o/D \gg 1$, the reaction at the a-$Li_\eta Si$/c-Si interface is fast, and Equation (7.6) becomes:

$$\frac{i}{i_o} = 2\sinh\left\{-\frac{F}{2RT}\left(\Phi - \Phi_{eq}^{\ ref} + \frac{RT}{F}\left[\frac{\Omega_{Li_\eta Si}}{q\eta(\eta+1)}\frac{y_o}{D}i\right]\right)\right\}. \tag{7.7}$$

During a segment where the current density is prescribed as a constant, the thickness of the lithiated layer, y_o, increases with time. As a result, the potential, Φ, decreases with time. Such behavior is indeed observed in numerous electrochemical experiments, including the lithiation of amorphous sputtered silicon, and is indicative of a diffusion-limited process.

In contrast, if $ky_o/D \ll 1$, the diffusion of lithium through the lithiated phase is fast, and Equation (7.6) becomes:

$$\frac{i}{i_o} = 2\sinh\left\{-\frac{F}{2RT}\left(\Phi - \Phi_{eq}^{\ ref} + \frac{RT}{F}\left[\frac{\Omega_{Li_\eta Si}}{q\eta(\eta+1)}\frac{1}{k}i\right]\right)\right\}. \tag{7.8}$$

Here, we take the reaction-rate, k, along a given crystal direction as a constant. In this limit, during a segment where the current density is prescribed as a constant, the potential, Φ, is likewise a constant. This observation is consistent with the previous discussion concerning our observed plateaus in potential, i.e. this reaction-limited situation corresponds to a moving phase boundary.

Another possible limit of Equation (7.6) occurs when the applied current density is very small such that $\frac{\Omega_{Li_\eta Si}}{q\eta(\eta+1)}\left(1+\frac{ky_o}{D}\right)\frac{1}{k}i \ll 1$, giving

$$\frac{i}{i_o} = 2\sinh\left[-\frac{F}{2RT}\left(\Phi - \Phi_{eq}^{\ ref}\right)\right], \tag{7.9}$$

which recovers the Butler-Volmer equation. It should be noted that the relative rates of diffusion and reaction at the a-$Li_\eta Si$/c-Si interface are irrelevant in this limit. Instead, both of these rates must be fast compared to the applied rate of insertion. Once again, during a segment where the current density is prescribed as a constant, the potential, Φ, is likewise a constant. This limit is known in literature as a process limited by the rate of the "surface reaction".[148]

Figure 7.4 demonstrates the effects of varying the intrinsic dimensionless parameters ky_o/D and $i_o\Omega_{Li_\eta Si}/kq\eta$ for a fixed value $i/i_o = 1$. To produce this figure, we have solved Equation (7.6) for the potential, Φ, for given values of the dimensionless constants. The various curves represent different values of the dimensionless constant $i_o\Omega_{Li_\eta Si}/kq\eta$. During an electrochemical experiment at a constant current density, the thickness of the lithiated layer, y_o, will increase in time. Thus, the horizontal axis is representative of time during such an experiment. The transition from a reaction-controlled to a diffusion-controlled process can clearly be seen as ky_o/D increases. Also, larger values of $i_o\Omega_{Li_\eta Si}/kq\eta$ indicate a slower rate of reaction at the interface between the lithiated silicon and the crystalline silicon, which results in larger values of overpotential, $\left|\Phi - \Phi_{eq}^{\ ref}\right|$.

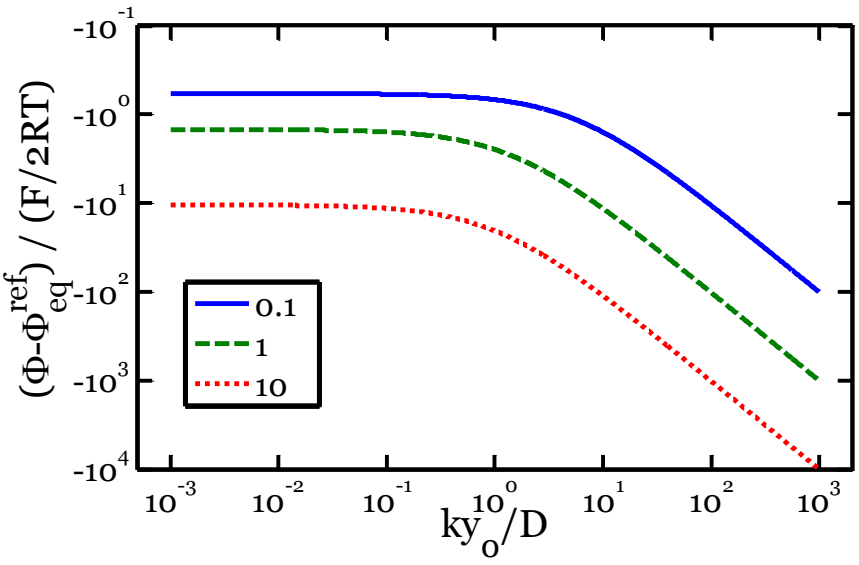

Figure 7.4. Potential predicted from kinetic model as a function of the dimensionless constant ky_o/D. The various curves represent different values of the dimensionless constant $i_o\Omega_{Li_\eta Si}/kq\eta$. In this simulation, $i/i_o = 1$.

We should also remark that within this model it is impossible to separate the contributions of the reactions at each interface from a single experiment. This is evident if we take the further limit of Equation (7.6) for which $i << i_o$:

$$\Phi - \Phi_{eq}^{\ ref} = -\frac{RT}{F}\left[\frac{\Omega_{Li_\eta Si}}{q\eta(\eta+1)}\frac{1}{k} + \frac{1}{i_o}\right] i. \qquad (7.10)$$

From Equation (7.10), it is clear that if one reaction is much faster than the other, the measured relation between i and Φ gives information on the slower process. If both contributions in brackets are comparable, a single measurement relating i and Φ does not give distinct information on both i_o and k. It may be possible, however, to quantify the individual contributions of the reactions at these interfaces from a set of multiple experiments in which one of these parameters is constant (or does not exist). For instance, one could measure the velocity of the phase boundary

in lithium-silicon diffusion couples for silicon wafers of various orientations. This experiment would give information on the parameter k, as the parameter i_o associated with the redox reaction is unimportant. In another experiment, amorphous silicon samples could be examined. In these amorphous silicon samples, the electrode is a single phase with a continuous variation in the lithium concentration during lithiation. Hence, only diffusion and the redox reaction at the electrolyte/electrode contribute to the kinetics of the insertion process. Thus, experiments could be performed to carefully characterize $i_o(C)$ near the compositions of interest. Furthermore, a set of multiple experiments in which i_o is a constant but k varies would give information on both parameters. We believe this latter situation applies to our experiments, as k depends on the crystallographic orientation, while i_o is the same during each experiment.

7.5 Comparison of kinetic model to experimental results

We now apply the kinetic model to our experimental data. Upon close examination of all of our data, we have found that the majority of the non-zero constant current segments produce extremely flat profiles in potential with time (see for instance, Figure 7.1). The only exception to flat potential profiles occurred in some of the {100} and {111} samples during the largest current density used, $100\ \mu A/cm^2$. In these anomalous segments, the potential increased with time (Figure B.1, B.2). As mentioned in the previous section, if the lithiation process were controlled by diffusion through the lithiated silicon phase, the potential would

decrease with time. Thus, we do not believe that the lithiation process is controlled by diffusion during these segments. We are uncertain about the precise origin of these upward sloping potentials, although they may correspond to some lithium from $a\text{-}Li_{\eta}Si$ being consumed by the formation of solid electrolyte interphase (SEI).

The data in Figure 7.2 and other experiments also suggest anisotropy in lithiation of crystalline silicon.[125]-[127] Recalling that the lithiated phase is amorphous, it is difficult to imagine a source of anisotropy if the kinetics of the lithiation process were dominated by the reduction reaction at the electrolyte/$a\text{-}Li_{\eta}Si$ interface. One may argue that the redox reaction depends on the nature of the SEI that forms between the electrolyte and the specific electrode, potentially leading to anisotropy. However, it seems improbable that the structure and composition of this SEI are strongly affected by the crystal orientation of the silicon, as the lithiated silicon side of this interface becomes amorphous during the early stages of the lithiation process. In contrast, anisotropy seems natural if the reaction at the $a\text{-}Li_{\eta}Si/c\text{-}Si$ interface contributes to the overall kinetics of the lithiation process. For this reaction to advance, cooperative rearrangement of atoms must occur, involving breaking and re-forming bonds. Surfaces of silicon in various crystallographic orientations have drastically different atomic structures, which can readily result in different rates of reaction on these different surfaces. For instance, such anisotropy has been observed in the rate of thermal oxidation of silicon of various crystal orientations.[149],[150] Thus, we believe that the reaction at the $a\text{-}Li_{\eta}Si/c\text{-}Si$ interface must contribute to the observed relationship between current

density and potential as shown in Figure 7.2.

As previously mentioned, it is impossible to separate the contributions of the reactions at each interface from a single experiment. However, we believe that i_o is independent of crystal orientation, while k is a function of crystal orientation. Since we have experiments for various crystal orientations of the silicon, we can fit both i_o and k. To do so, we have written in a program in Matlab to solve Equation (7.8) for a given k and i_o to produce a relationship between the applied current densities and predicted potentials. We have then performed a least-squares fit between the measured and predicted potentials to find the appropriate values of k for each orientation and i_o. The parameters used in this simulation are given in Table 7.1. The value used for η is a representative value found in other experiments under similar conditions.[145] Although this number may not be entirely accurate for our experiments, changing the value of η will only scale the predicted value of k by some constant numerical factor and will not affect the relative values of k for the various orientations. Also, the equilibrium potentials used in the simulation are the instantaneous values measured during the open circuit voltage segments in our experiments. It is important to note that the equilibrium potential associated with the {110} Si is approximately $20\ \text{mV}$ larger than the other two orientations.

The results of this fit are shown in Table 7.1. Using these values, the predicted relationships between potential and current density are shown as dashed lines in Figure 7.2. The predictions from the fit agree well with the data. Both the

calculated reaction rate at the a-$Li_\eta Si$/c-Si interface and the measured equilibrium potential are largest for {110} Si. Each of these characteristics contributes to the phase boundary moving "fastest" in the <110> direction for a given potential.

Parameter	**Value**
T	20°C
η	3.5 [145]
$\Omega_{Li_{3.5}Si}$	6.91×10^{-29} m^3 [146]
Φ_{eq}^{ref} : <110>	149.2±2.33 mV
Φ_{eq}^{ref} : <111>	129.4±2.41 mV
Φ_{eq}^{ref} : <100>	128.3±3.05 mV
$\beta = \Omega_{Li_\eta Si} / \Omega_{Si}$	3.21 [146]
σ_Y	1 GPa [82]
E_{Si}	160 GPa [154]
$E_{Li_\eta Si}$	12 GPa [116]
$\nu_{Si} = \nu_{Li_\eta Si}$	0.22 [154]
i_o *	0.45 A/m^2
k: <110> *	1.63×10^{-10} m/s
k: <111> *	7.05×10^{-11} m/s
k: <100> *	2.54×10^{-11} m/s

Table 7.1. Parameters used in simulations and calculated results. Results calculated from a fit of the model to the experimental data are denoted by *.

In the model, we have assumed a metastable equilibrium state, $Li_{3.5}Si$, as motivated by the observations of Li, et al.[145] For small deviations from this composition, we can treat the quantities γ, D, i_o, and k as constants, independent of the concentration of lithium in the lithiated silicon phase. As a particular example, with the assumption that the lithiated phase is $Li_{3.5}Si$, we would expect the measured equilibrium potentials during open-circuit segments to be independent of the crystal orientation of the silicon. It was found, however, that the equilibrium potential for {110} Si was about $20\,mV$ larger than for the other two orientations. It is possible that this discrepancy is due to a slightly different composition existing in the amorphous phase during the experiments on {110} Si. For instance, if the rate of the reaction at the $a\text{-}Li_\eta Si/c\text{-}Si$ interface for {110} Si is fast compared to the insertion rate (i.e. applied current density), then the concentration of lithium in the lithiated phase may be slightly smaller than that of the {100} and {111} orientations. This effect would result in a larger measured equilibrium potential, Φ_{eq}^{ref}, for {110} Si compared to the other orientations, which is consistent with the experiments. Such dependence of the composition of the metastable phase on the orientation of the crystalline phase is not considered in our model; Φ_{eq}^{ref} is simply taken as an input parameter measured from our experiments. This interplay may be important for the lithiation process, however, as it further amplifies the anisotropy along different crystal directions. Thus, once functions such as $\gamma(C)$, $D(C)$, $i_o(C)$, etc. are more carefully characterized, they can be incorporated into the kinetic model to make it more complete. Still, we

believe that the important physics associated with the initial lithiation of crystalline silicon have been captured in our kinetic model.

The model also provides some information of the value of the diffusivity of lithium in amorphous silicon. As discussed previously, it is evident from the flat potential profiles that diffusion through the lithiated phase is not the rate-limiting step. Using the values from the fit for i_0 and k, however, we can substitute various values of D into Equation (7.6) and evaluate the effect on the potential profiles. The results are shown in Figure 7.5, where it is evident that the potential profiles would look drastically different if the diffusivity were as slow as 2×10^{-17} m^2/s. In comparison to the reaction-limited case, the measured potentials would be much smaller and would create profiles decreasing with time. Moreover, these slopes would increase in absolute value with current density, as given by Equation (7.6). If we applied our kinetic model to a system that is rate-limited by diffusion through the electrode, we could fit Equation (7.6) to the data to measure the value of diffusivity but as previously discussed, the overall kinetic process does not seem to be limited by diffusion through the amorphous layer during the initial lithiation of crystalline silicon. Still, the results in Figure 7.5 can be used to estimate a lower bound on the diffusivity. Bearing in mind that the actual data are similar to the solid gray line in Figure 7.5, a reasonable estimate of the lower bound for the diffusivity of lithium in a-$Li_{3.5}Si$ is $D=2\times10^{-16}$ m^2/s. In comparison to values in the literature, Ding, et al. found a value of 1×10^{-16} m^2/s for nano-crystalline silicon particles using the galvanostatic intermittent titration technique (GITT), cyclic

voltammetry (CV), and electrochemical impedance spectroscopy (EIS) at room temperature.[89] Similarly, Xie, et al. found a value of $3\times10^{-17} - 3\times10^{-16}$ m^2/s for sputtered amorphous silicon films using EIS at 20°C .[151]

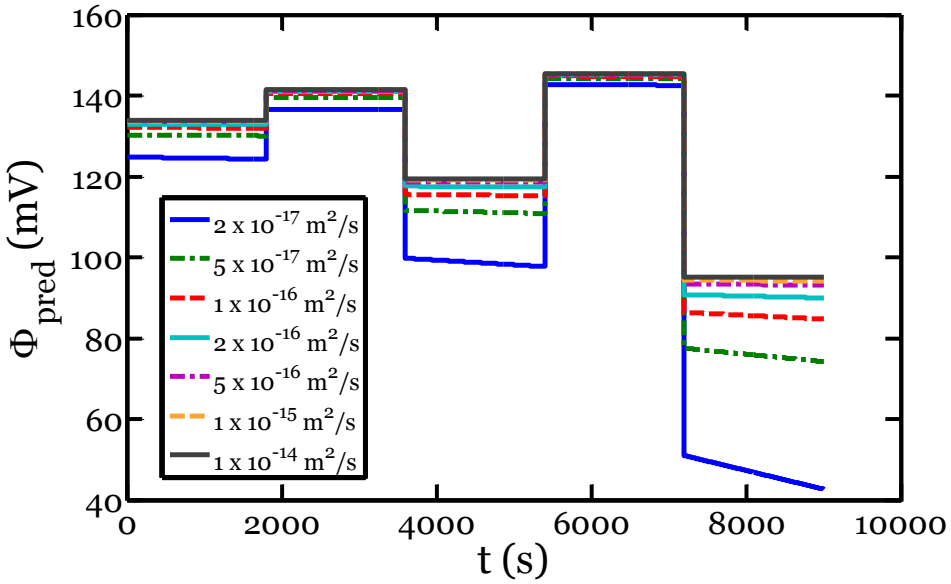

Figure 7.5. Predicted response in potential vs. Li/Li$^+$, Φ_{pred}, for a {110} Si wafer with initial lithiated thickness of $1\ \mu m$ subject to the current loading shown in Figure 7.1. The various curves represent different hypothetical values of the diffusivity of lithium through the lithiated silicon phase.

As a final comment, we have seen no evidence of diffusion-limited kinetics despite having lithiated samples to thicknesses on the order of microns. In contrast, typical nanostructured electrodes of silicon have feature sizes less than a few hundred nanometers.[80],[79],[97],[152],[153] Thus, under normal operating conditions, lithiation of crystalline silicon will be limited by the reaction of silicon and lithium at the reaction front, rather than by the diffusion of lithium through the amorphous phase.

7.6 Finite element modeling of the initial lithiation of crystalline silicon

We now use the measured velocities of the reaction fronts to quantify recent experimental observations. This analysis is performed under the framework of a previously developed model of concurrent reaction and plasticity (Chapter 6). The concurrent reaction and plasticity are simulated using the finite element program ABAQUS. Within the context of the program, the lithiation-induced volumetric expansion is simulated as thermal expansion, while deformation in the lithiated silicon is modeled by the elastic-plastic theory (J_2 plasticity).[88] The crystalline silicon is modeled as an elastic material. To simulate the movements of the reaction fronts, we prescribe a moving temperature field. To avoid computational singularity, the temperature front, which simulates the reaction front, is located within a thin shell, whose size is much smaller than the feature size of the nanopillar but is sufficiently larger than the mesh size. Such regularization is used to afford a compromise between computational cost and accuracy.

To illustrate this model in combination with our experimental data, we simulate the morphological evolution and stress development during the lithiation of crystalline silicon nanopillars of various axial orientations.[126] The black lines in the second column of Figure 7.6 show the crystal orientations of the sidewalls of these silicon nanopillars. The velocities of the fronts depend on the crystallographic orientation, with values given by our experiments at 120 mV (so-called "partial lithiation" by Lee, et al.[126]). In particular, at this potential, the relative velocities

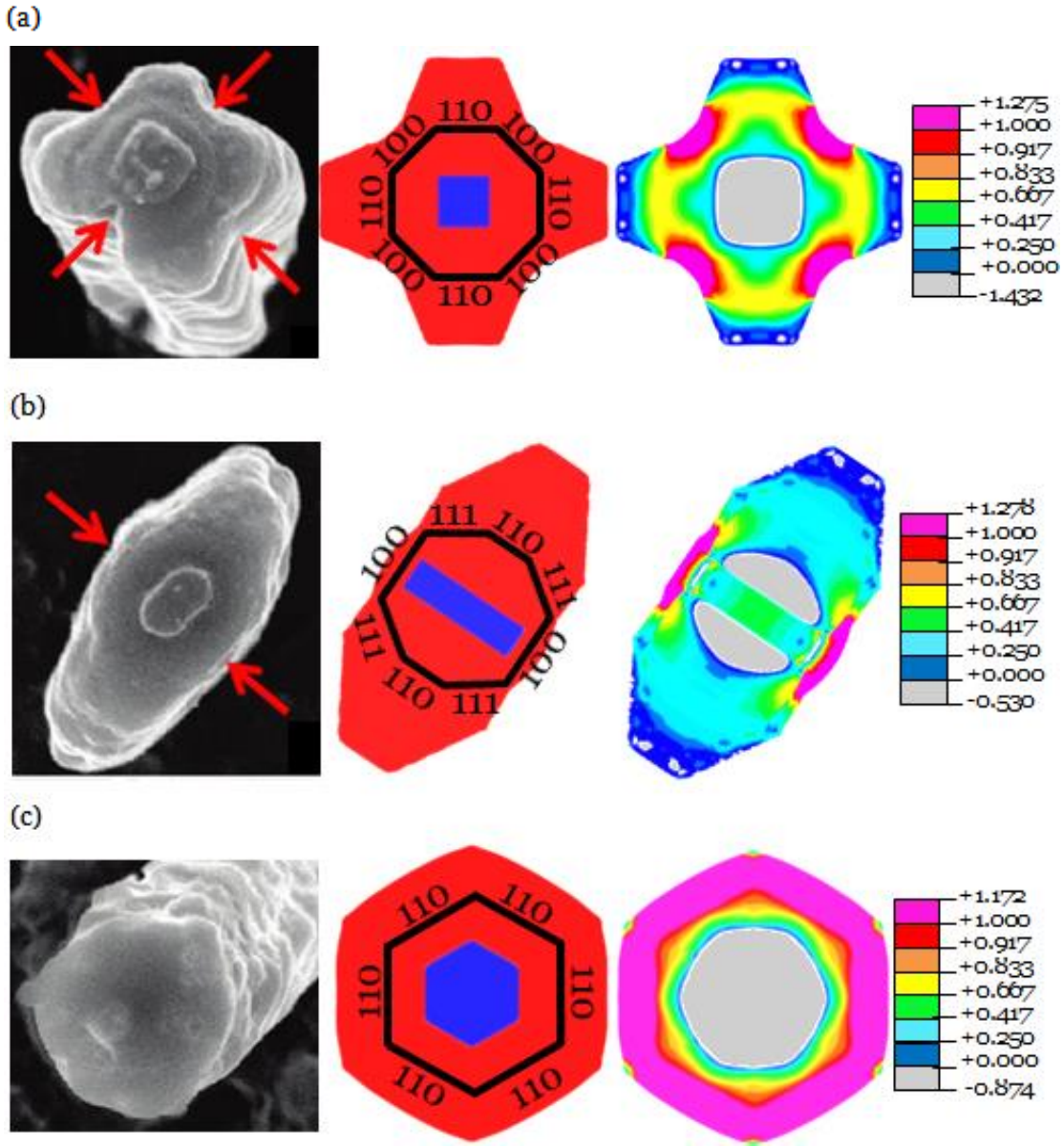

Figure 7.6. Comparison between experiments and finite element simulation of lithiation of crystalline silicon nanopillars of various axial orientations: (a) <100>, (b) <110>, and (c) <111>. The first column shows the experimentally observed morphology after lithiation from Lee et al.[126] The red arrows indicate the fracture sites observed most frequently in experiments.[155] The second column shows simulated morphology at a certain stage of lithiation. The fully lithiated phase is given in red while the crystalline silicon phase is shown in blue. The black outline shows the initial shape in the simulation and the corresponding orientations of the crystal facets. The third column shows the maximum in plane stress at the same stage of lithiation. The pink regions have stresses exceeding the yield strength. The legend shows the stress in units of GPa .

were found to be $V_{<110>} = 6.4V_{<100>} = 6.1V_{<111>}$. It is important to note that within this model, the absolute velocities of the reaction fronts are not important in developing the stress and deformation fields; only the relative velocities matter. In this simulation, we have used the following parameters: $\beta = \Omega_{\mathrm{Li}_\eta\mathrm{Si}} / \Omega_{\mathrm{Si}} = 3.21$,[146] $\sigma_Y = 1\mathrm{GPa}$,[82] $E_{\mathrm{Si}} = 160\mathrm{GPa}$,[154] $E_{\mathrm{Li}_\eta\mathrm{Si}} = 12\mathrm{GPa}$,[116] $\nu_{\mathrm{Si}} = \nu_{\mathrm{Li}_\eta\mathrm{Si}} = 0.22$.[154] It should be noted that the modulus and Poisson's ratio of the crystalline Si phase are taken as independent of orientation. This approximation is made for simplicity of implementation into the ABAQUS model. The modulus used for the crystalline phase is that of polycrystalline silicon, which is a representative modulus of the core in an average sense. The pillars are modeled using plane-strain conditions, as motivated by experimental observations of a lack of growth in the axial direction.[126] Figure 7.6 shows the stress and morphology of the nanopillars after partial lithiation simulated using the procedure described above. The simulated anisotropic patterns agree extremely well with the experimental observations.[126]

Recently, it has been observed that under certain conditions these nanopillars will fracture anisotropically.[155] Moreover, Lee, et al. surmised that this anisotropic fracture results from stress concentrations due to the anisotropic expansion of the nanopillars.[155] Here, we quantify this idea using ABAQUS and our experimentally measured reaction front velocities. In Figure 7.6, we observe that for the <100> and <111> nanopillars the maximum principal tensile stress occurs at the locations midway between neighboring {110} planes. These locations are consistent with the fracture locations most frequently observed in the work of Lee et al.[155]

Furthermore, we observe that the maximum tensile stress can exceed the yield strength due to the triaxiality of the state of stress at these locations. In the simulation of the <111> nanopillar, the state of stress was found to be approximately axisymmetric, implying that there should be little anisotropy in the locations of fracture. In the work of Lee, et al. fracture was indeed observed at arbitrary locations albeit with a slightly higher incidence at locations between the {110} planes.[155] Thus, our simulations agree quite well with their experiments.

7.7 Summary

In this chapter, we have performed electrochemical experiments on {100}, {110}, and {111} crystalline silicon wafers. These experiments indicate the existence of a moving phase boundary for all three orientations, indicating that short-range processes at the $a\text{-}Li_{\eta}Si/c\text{-}Si$ interface significantly contribute to the kinetics of the lithiation process. The velocity of this phase boundary was found to be faster for {110} silicon than for the other orientations. Using the measured velocities, we have implemented a model of concurrent reaction and plasticity into ABAQUS. This simulation accurately accounts for anisotropic morphologies and fracture patterns developed in crystalline silicon nanopillars of various axial orientations. Furthermore, we have presented a kinetic model accounting for the redox reaction at the electrolyte/$a\text{-}Li_{\eta}Si$ interface, diffusion through the $a\text{-}Li_{\eta}Si$, and the chemical reaction at the $a\text{-}Li_{\eta}Si$/crystalline silicon interface. From this model, we have quantified the rates of reactions at the interfaces and have provided a lower bound for

the diffusivity through the lithiated silicon phase. We believe that this model accounts for the pertinent physics in electrodes that undergo two-phase coexistence and will have further value beyond the silicon system. Thus, we hope this model will provide guidance for the design of future experiments and atomistic simulations.

Chapter 8

Measurements of the Fracture Energy of Lithiated Silicon Electrodes

8.1 Introduction

A number of recent experimental studies have measured mechanical properties of silicon electrodes. For instance, Sethuraman et al. used the substrate curvature method to measure the stress in thin-film silicon electrodes as a function of lithium concentration. They found that lithiated silicon flows plastically at a stress of ~1.7 GPa for $Li_{0.3}Si$, with this stress decreasing to ~1 GPa for Li_2Si.[82] Soni et al. and Zhao et al. performed similar measurements and have found comparable results.[146], [156] Hertzberg et al. used nanoindentation methods to measure the hardness and elastic modulus of lithiated nano-crystalline thin-film silicon electrodes as a function of lithium concentration. They found that the hardness decreases from 5 to 1.5 GPa and the elastic modulus decreases from 92 to 12 GPa in transitioning from the pure nano-crystalline silicon phase to the fully lithiated phase ($Li_{15}Si_4$).[116] Sethuraman et al. measured the biaxial elastic modulus of thin-film silicon electrodes as a function of lithium concentration using the substrate curvature method, finding a biaxial modulus of 70 GPa for $Li_{0.32}Si$ and 35 GPa for Li_3Si.[117] Kushima et al. measured the tensile strength of single-crystal silicon nanowires, finding a strength of 3.6 GPa for unlithiated silicon nanowires and a strength of 0.72 GPa for lithiated silicon nanowires ($Li_{15}Si_4$).[157] In addition to these experimental studies, a number of

theoretical works, including those of Chapters 4-6 in this thesis, have examined the fracture of silicon electrodes.[50],[68],[91],[94],[143],[158]-[160] An important parameter in these analyses is the fracture energy of the lithiated phase. Thus far, in these theoretical works, the values of the fracture energy are merely educated guesses since no quantitative measurements have been performed. Moreover, a single number is usually assigned, despite the possibility of the fracture energy varying with lithium concentration.

In this chapter, we devise a method to measure the fracture energy of lithiated silicon thin-film electrodes. To achieve this goal, we have constructed an electrochemical cell with an array of parallel electrodes allowing us to lithiate/delithiate the electrodes to different states of charge, while performing in-situ stress measurements. The electrodes were then examined by microscopy both to observe the morphological development of the cracks and to construct a bound on the critical state of charge corresponding to the formation of cracks. By determining this critical state of charge and knowing the corresponding state of stress, we quantify the fracture energy through an analysis from fracture mechanics. From the same set of experiments, we can obtain an additional measurement of the fracture energy at a second state of charge – at small concentrations of lithium – by determining the maximum value of the substrate curvature during delithiation.

8.2 Experimental technique to measure the fracture energy of lithium-ion battery electrodes

Silicon electrodes typically have features on the order of 100 nanometers and include nanowires,[79],[161] nano-porous structures,[152] nano-particles,[97],[110] and thin-films.[80],[94]-[96],[156] Of these options, quantitative electrochemical characterization of individual nanowires and nanoparticles proves prohibitively difficult. Thus, in this study, thin films were selected as the working electrodes. Glass substrates with a thickness of 1 mm were cleaned with acetone and isopropanol and placed into a sputter deposition system (AJA Int. ATC 1800) with a base pressure of $<10^{-8}$ Torr. All sputtering targets had a 50.8 mm diameter and depositions were performed at room temperature (22°C). First, the samples were plasma-cleaned in Ar at 20 mTorr and an RF power of 24 W for 5 minutes. Next, 15 nm of Ti was sputtered onto the substrates using a pressure of 3 mTorr of Ar and a DC power of 100 W for 5 minutes. A 300 nm layer of Cu was then deposited on the Ti underlayer using a pressure of 5 mTorr of Ar and a DC power of 100 W for 15 minutes. The Cu film serves as current collector, while the Ti underlayer is used to improve the adhesion between the Cu film and the glass substrate. Finally, a 300 nm Si film was deposited on the Cu current collector using a pressure of 5 mTorr of Ar and a DC power of 100 W for 78 minutes. The working area of each silicon electrode was 8 mm by 20 mm. After deposition, x-ray diffraction was used to verify the amorphous structure of the sputtered Si thin-films.

Electrochemical experiments were conducted in a custom-fabricated hermetic Teflon electrochemical cell with a glass window (Figure 8.1). The cell employs a Li reference electrode, seven Si working electrodes, and seven Li counter electrodes. In

essence, it is a three-electrode configuration but with multiple working and counter electrodes operating in parallel. A schematic of the cell is shown in Figure 8.1; only three working and reference electrodes are shown for simplicity whereas seven of each are actually used in the experiments. This arrangement resulted in a total resistance from the galvanostat to the electrodes (including contact resistance with the electrode) of less than $2\,\Omega$ for each connection, which resulted in a voltage drop of less than $400\,\mu V$ in these experiments. The cell was assembled in a glovebox maintained at <0.1 ppm moisture and used a 1M solution of $LiPF_6$ in 1:1:1 (weight %) ethylene carbonate: diethyl carbonate : dimethyl carbonate as the electrolyte. Electrochemical measurements were performed with a VersaSTAT 3 galvanostat from Princeton Applied Research. The seven silicon electrodes were lithiated simultaneously at a constant current density of $15\,\mu A/cm^2$ (a C/16 rate assuming a capacity of $3579\,mAh/g$) to a cutoff potential of $0.01\,V$. Although not pursued in this study, this cutoff potential in principle can be varied to examine properties as a function of lithium concentration. The relatively slow rate of lithiation was selected to allow enough time for diffusive equilibrium through the films.[78],[156] The electrodes were then delithiated at the same current density $\left(15\,\mu A/cm^2\right)$. At various stages of delithiation (as marked by red arrows in Figure 8.2), the electrodes were disconnected one by one from the cell such that they were only partially delithiated. Delithiation then resumed with a new current such that the current density remained constant during the entire delithiation sequence. One electrode in each test was fully delithiated to a cutoff potential of 2V.

For the electrode that was fully delithiated, the stress in the film was measured by monitoring the substrate curvature in situ during lithiation/delithiation. The average stress in the film was deduced from the curvature of the substrate using Stoney's equation[162],[163]:

$$\sigma = \sigma_r + \frac{E_s h_s^2}{6h_f\left(1-\nu_s\right)}\Delta K\,, \tag{8.1}$$

where σ is the average stress in the film, E_s is the elastic modulus of the substrate, h_s is the thickness of the substrate, h_f is the thickness of the film, ν_s is Poisson's ratio of the substrate, and ΔK is the change in curvature of the substrate that results from the stress in the film. σ_r denotes the initial residual stress in the film, i.e., the stress that developed during sputter deposition. This stress was determined by measuring the curvature of the substrate before and after silicon deposition. It is important to note that knowledge of the properties of the film other than the thickness is not required to evaluate the stress using Stoney's equation. In the calculations, values of E_s=77 GPa and $\nu_s = 0.22$ were used for the glass substrates.

We should also note that SEI growth during the initial lithiation may contribute to the measured stress. To address this point, we have performed additional experiments (not included here) on electrodes with identical surface areas but with different initial film thicknesses of 100 nm and 300 nm. Due to the smaller film thickness, the SEI will have a larger relative contribution to the measured stresses in the 100 nm film. However, the stresses (not accounting for SEI formation) that we measure in the two experiments are almost identical. Hence, it appears that the stresses we measure in our experiments are primarily due to those

that develop in the silicon film, and we have thus neglected any contribution of the SEI to the measured stress.

The volume of the film, V_f, is taken to be linear in the state of charge,

$$V_f = V_f^o(1+\beta s), \tag{8.2}$$

where V_f^o is the initial volume of the film, β is related to the atomic volumes (Ω) by $\beta = (\Omega_{Li3.75Si} - \Omega_{Si})/\Omega_{Si}$, and s is the state of charge of the silicon electrode, with a value of 0 representing pure silicon and a value of 1 representing the fully lithiated state (assumed to be $Li_{3.75}Si$ with a capacity of 3579 mAh/g).[164] According to Obrovac et al., Si will undergo a 280% increase in volume upon reaching the fully lithiated state of $Li_{3.75}Si$, i.e., $\beta = 2.8$.[164] Using atomic force microscopy, He et al. and Beaulieu et al. measured similar values in patterned amorphous silicon films.[165],[166] Moreover, both groups found that the volume increased linearly with lithium concentration.[165],[166] For a thin-film geometry, lithium insertion is accommodated entirely by growth in the thickness direction due to the constraint in the in-plane directions placed by the relatively thick substrate. Thus, the thickness of the film, h_f, takes the same form as in Equation (8.2):

$$h_f = h_f^o(1+\beta s), \tag{8.3}$$

where h_f^o is the initial thickness of the film. The initial thicknesses of the Si electrodes were measured by profilometry and were approximately 300 nm $(\pm 15\text{nm})$ for all of the sputtered films.

The curvature of the substrate was monitored with a multi-beam optical sensor (MOS) from k-Space Associates (Figure 8.1). The MOS employs an array of

parallel laser beams to measure the curvature of the substrate. The array of laser beams allows simultaneous illumination and detection, which in turn greatly reduces noise in the measurements caused by fluid motion in the electrochemical cell or by ambient vibrations. The cell is also placed on an anti-vibration table during testing.

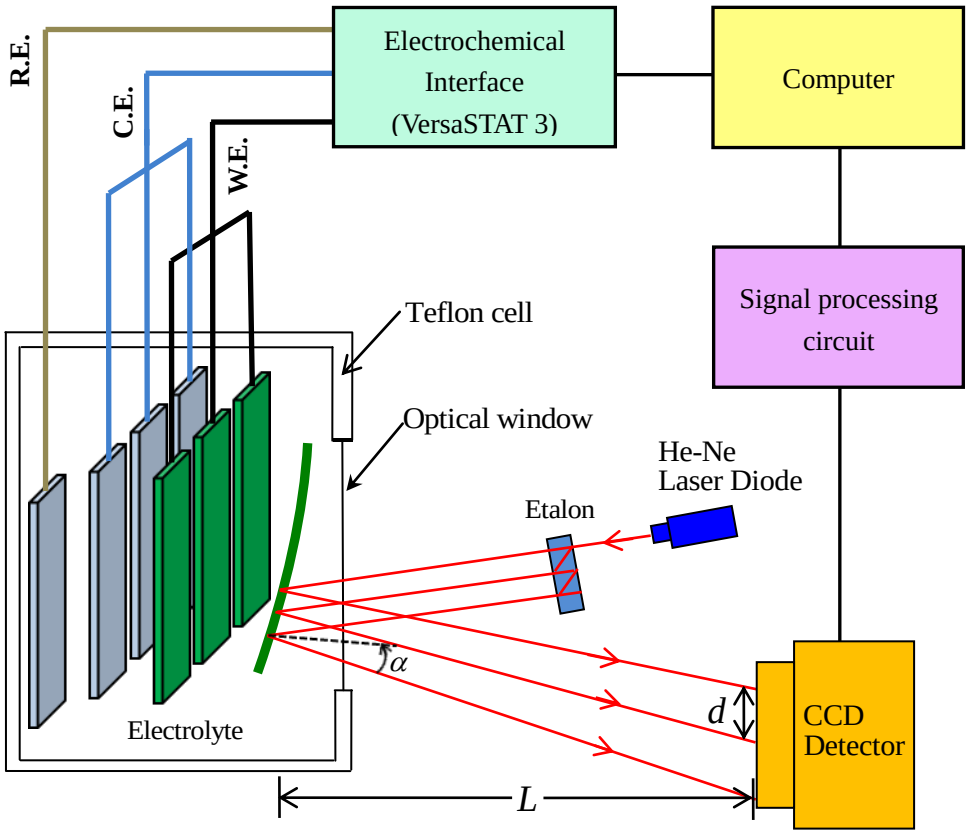

R. E. - reference electrode C. E. - counter electrode. W. E. - working electrode

Figure 8.1. A schematic representation of the custom-made electrochemical cell with in-situ multi-beam optical sensor. Only three working electrodes and counter electrodes are drawn; there are seven working electrodes and counter electrodes in the actual cell. The stress is measured in one of the working electrodes, as depicted by the right-most green line, which shows the electrode after bending due to lithium insertion.

The change in the curvature of the substrate (see Figure 8.1) is calculated from the geometric relation

$$\Delta K = \frac{d_o - d}{d_o}\left[\frac{\cos\alpha}{2L}\right]\frac{n_a}{n_e}, \tag{8.4}$$

where d is the distance between two adjacent laser spots measured on the CCD camera, d_o is the initial distance between the laser spots, α is the angle of reflection of the laser beams, L is the distance between the electrochemical cell and the CCD camera, and n_a and n_e are the indices of refraction of air and the electrolyte, respectively. Since the laser passes through air, the electrolyte, and an optical window, refraction of the laser beams at these corresponding interfaces must be taken into account, which is the source of the quantity n_a/n_e. In the calculation of the stress, we took n_e=1.42 for the electrolyte[167] and n_a=1 for air. Neglecting refraction of the laser beams would result in a substantial error in the curvature measurement of approximately 40%.

The biaxial elastic modulus of the lithiated silicon is determined by measuring the stresses during the initial stage of delithiation. In this stage, the in-plane strain associated with lithium extraction from the electrode is accommodated entirely by elastic deformation. At a particular state of charge, s, the volume of the electrode is given by Equation (8.2). At a state of charge, $s+\Delta s$, where Δs is sufficiently small to ensure elastic deformation of the film, the volume of the film is $V_f = V_f^o\left[1+\beta\left(s+\Delta s\right)\right]$, and thus the volumetric strain is $\left[V_f\left(s+\Delta s\right)-V_f\left(s\right)\right]/V\left(s\right)=\beta\Delta s/\left(1+\beta s\right)$. Hence, in going from a state of charge, s, to a state of charge, $s+\Delta s$, the increment in the linear strain induced by lithiation, $\Delta\varepsilon^l$, is

$$\Delta\varepsilon^l = \frac{1}{3}\frac{\beta\Delta s}{1+\beta s}. \tag{8.5}$$

Due to the constraint placed by the substrate, the total in-plane strain vanishes and the lithiation strain necessarily results in an elastic strain $\Delta\varepsilon^e = -\Delta\varepsilon^l$, which in turn results in a stress given by Hooke's law. For a thin film, the stress state is equal biaxial and the increment in the stress $\Delta\sigma$ is

$$\Delta\sigma = \frac{E_f}{1-\upsilon_f}\Delta\varepsilon^e, \tag{8.6}$$

where ν_f is Poisson's ratio of the film and E_f is the elastic modulus of the film. Thus,

$$\frac{E_f}{1-\nu_f} = -3\frac{1+\beta s}{\beta}\frac{\Delta\sigma}{\Delta s}. \tag{8.7}$$

Using Equation (8.7), one can calculate the biaxial modulus of the film, $E_f/\left(1-\nu_f\right)$, by measuring the state of charge and stress during the elastic stage of delithiation.

To image the electrodes, they were removed from the cell in the glovebox, rinsed in dimethyl carbonate, and dried. Next, they were immersed in mineral oil and covered with a glass slide to prevent any exposure of lithiated silicon to air. The samples were then removed from the glovebox and examined using an optical microscope. This technique allowed us both to construct a bound on when cracks initially form and to examine the evolution of the crack morphology with further delithiation. The same goal could be achieved by direct monitoring of the surface of a single electrode during delithiation, but simultaneous integration of optical microscopy and stress measurements with the electrochemical cell is not straightforward. For observation in the scanning electron microscope (SEM), the

samples were sealed in an airtight container in the glovebox and immediately transferred to the SEM chamber. It was estimated that the samples were exposed to air for less than two minutes during transfer to the SEM.

8.3 Fracture energy of lithiated silicon electrodes

Figure 8.2 shows a typical response of the potential and stress measured during lithiation/delithiation. During delithiation, the electrodes are removed one by one at the points represented by red arrows in Figure 8.2. In Figure 8.2a, we can see that the voltage gradually decreases with the state of charge. This voltage profile can be contrasted with the extremely flat voltage profiles observed during the initial lithiation of crystalline silicon wafers (e.g. Figure 7.1).[124],[168] Such flat profiles indicate a two-phase reaction in crystalline silicon, while the sloping profiles observed here indicate a single-phase reaction. Recently, McDowell et al. and Wang et al. have performed in-situ transmission electron microscopy (TEM) observations during the initial lithiation of individual amorphous silicon nanoparticles.[169],[170] Both groups have identified a phase front separating amorphous silicon from amorphous lithiated silicon, i.e., the initial lithiation of amorphous silicon occurred by a two-phase mechanism in their experiments.[169],[170] We propose that the lithiation rate is the critical difference between our experiments and those performed on the individual amorphous nanoparticles. In the latter, full lithiation occurs in approximately 100 seconds, whereas in our work, full lithiation occurs over 16 hours. The relatively slow rates used in our experiments apparently engender lithiation

through a single-phase reaction mechanism.

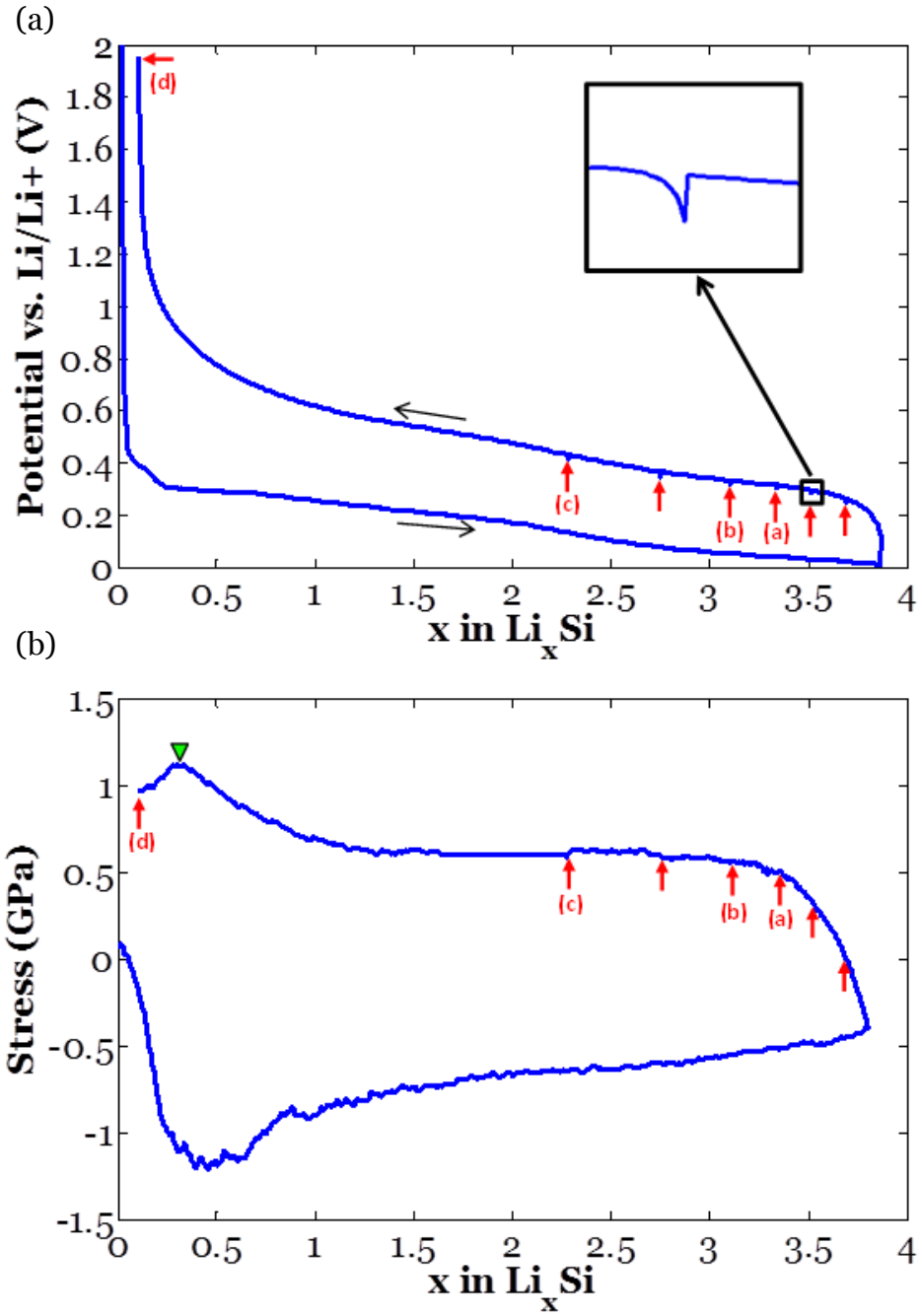

Figure 8.2. Representative responses in (a) potential vs. Li/Li+ and (b) stress as a function of lithium concentration from a galvanostatic test of a set of seven 300 nm a-Si thin films. During delithiation, the electrodes are disconnected at various concentrations of lithium, as indicated by the red arrows. The inset in (a) shows a zoomed-in view near one of these points. The letters near some of the arrows correspond to the images labeled in Figure 8.3. The green triangle in (b) indicates the location of the maximum tensile stress.

A typical sequence of the measured stress is shown in Figure 8.2b. The film initially is under residual tension ($70\,\text{MPa}$ in this case), which results from the sputtering process. The stress becomes more and more compressive as lithium is inserted into the electrode until it begins to flow plastically at a stress of $-1.2\,\text{GPa}$ and a concentration of $\text{Li}_{0.4}\text{Si}$. Upon further lithiation, the film continues to flow plastically with a continuous small reduction in the stress, reaching a value of $-450\,\text{MPa}$ at the fully lithiated concentration of $\text{Li}_{3.75}\text{Si}$. We note that these values compare quite well to the hardness values reported by Hertzberg, et al. In particular, using the relation $\sigma_Y = H/3$, where H is the indentation hardness, Hertzberg, et al. found values of $\sigma_Y = 1.1\,\text{GPa}$ for $\text{Li}_{0.6}\text{Si}$ and $\sigma_Y = 550\,\text{MPa}$ for $\text{Li}_{3.75}\text{Si}$.[116] During delithiation, the stress becomes more and more tensile until it begins to flow in tension at a stress of $500\,\text{MPa}$ and a concentration of $\text{Li}_{3.4}\text{Si}$. Additional delithiation results in further plastic flow with a continuous increase in stress, reaching a maximum value of $1.12\,\text{GPa}$ at a lithium concentration of $\text{Li}_{0.33}\text{Si}$. After this point, the measured value of the stress decreases with further delithiation.

We should also point out that in Figure 8.2, the horizontal axes are constructed by integrating the current during the experiment to get the total charge. However, the amount of charge does not necessarily represent the concentration of lithium in silicon, as SEI formation may consume some lithium. Recently, Nadimpalli, et al. quantified the capacity loss due to SEI formation.[18] In their experiments, they used the same electrodes, the same electrolyte, and very similar electrochemical loading conditions as in our experiments. They have found that the

charge lost per surface had an upper bound of 0.023 mAh/cm^2.[18] This loss corresponds to a capacity of 329 mAh/g in our experiments, which is less than 10% of the total capacity (3579 mAh/g). Thus, there may be a systematic error of at most 10% in the values of the lithium concentration reported in Figure 8.2.

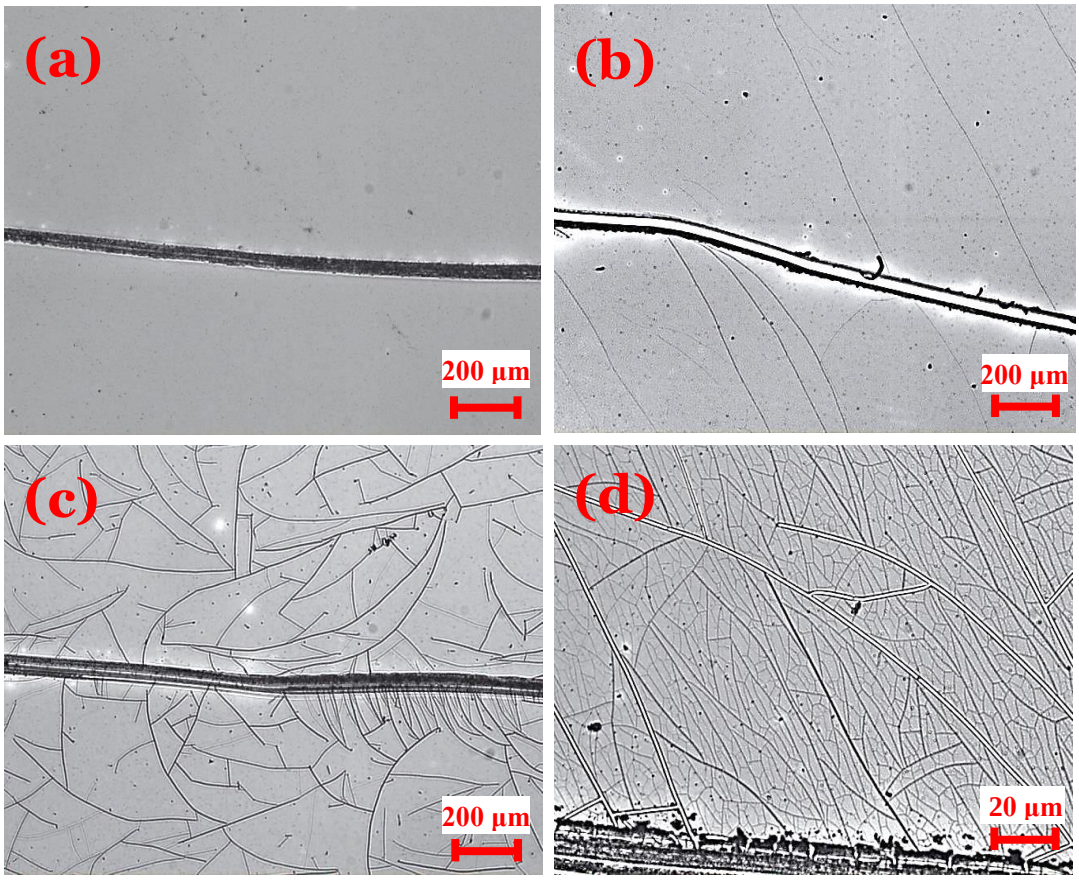

Figure 8.3: Optical micrographs of the electrodes tested in Figure 8.2. The labels (a)-(d) correspond to the point at which the electrode was disconnected from the cell, as indicated in Figure 8.2.

Figure 8.3 shows optical micrographs of the electrodes at various extents of delithiation. The images in this figure were taken at locations near scratches in the film introduced by a diamond scribe. The labels (a) – (d) in Figure 8.3 correspond

to the labeled red arrows shown in Figure 8.2, indicating the extent to which each of the electrodes was delithiated. The electrode in Figure 8.3a shows no evidence of fracture, whereas the electrode in Figure 8.3b does. From this observation, we can quantify a bound on the fracture energy by calculating the range of energy release rates between these two lithium concentrations (i.e., between the points labeled (a) and (b) in Figure 8.2b). Upon further delithiation, more cracks are formed, and the electrode develops a distribution of crack widths as illustrated in Figures 8.3d and 8.4a. The very wide cracks (Figure 8.4b) are formed during the earlier stages of delithiation (such as those seen in Figure 8.3b) and widen with subsequent delithiation. This process is most likely caused by an interfacial sliding mechanism as discussed in a number of previous works.[94],[96],[159] The narrower cracks (the majority of the cracks as seen in Figures 8.3d & 8.4a) are formed between the points indicated by arrows (c) and (d) in Figure 8.2, which allows us to calculate a value of the fracture energy at low concentrations of lithium (discussion to follow).

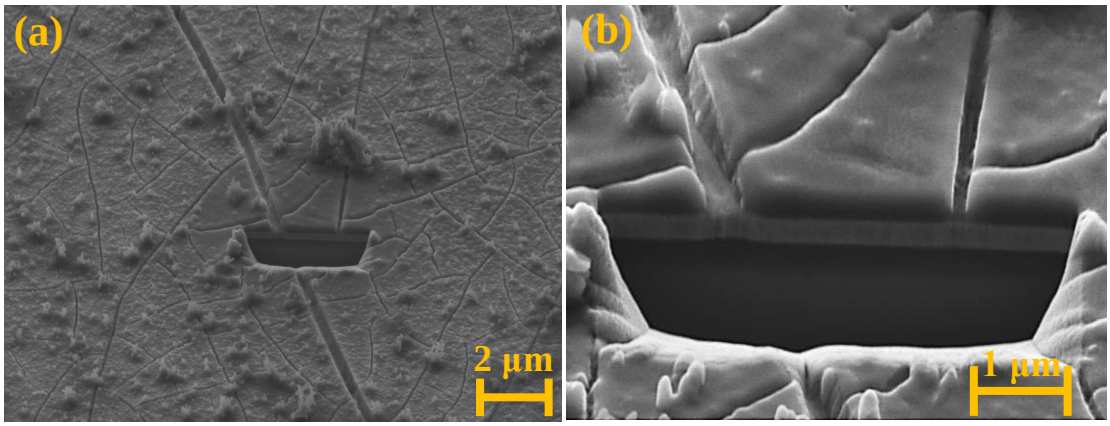

Figure 8.4. SEM images near a FIB cross-section of a 300 nm a-Si electrode after one cycle at (a) 10,000x magnification (b) 50,000x magnification.

To calculate these energy release rates, one has to be particularly careful due to the flow of the lithiated silicon during the experiments and the possibility of sliding at the interface between the lithiated silicon and copper. If the initial flaw size is small compared to the thickness of the film, the energy release rate, G, takes the form:

$$G = Z\frac{\sigma^2 a}{\bar{E}_f}, \tag{8.8}$$

where Z is a non-dimensional parameter and a is the length of the initial flaw. For instance, for a crack of length $2a$ in an infinite body, $Z = \pi$.[114] For a thin-film geometry, Nakamura and Kamath investigated the energy release rate as a function, a/h: the ratio of crack length to film thickness.[171] For $a/h \ll 1$, the analysis given by Equation (8.8) is appropriate. For $a/h \geq 1$, Nakamura and Kamath show that the energy release rate becomes independent of the flaw size such that a steady-state analysis performed by Beuth is appropriate.[171] Beuth's analysis is for a steady-state channeling crack in an elastic thin film bonded to an elastic substrate.[172] The energy release rate is given by

$$G = g(\alpha,\beta)\frac{\sigma^2 h_f}{\bar{E}_f}, \tag{8.9}$$

where $\bar{E}_f = E_f/\left(1-\nu_f^2\right)$ is the plane-strain modulus of the film, and $g(\alpha,\beta)$ is a function of the Dundurs parameters, α and β, which are defined by

$$\alpha = \frac{\bar{E}_f - \bar{E}_s}{\bar{E}_f + \bar{E}_s}, \qquad \beta = \frac{\mu_f\left(1-2\nu_s\right)-\mu_s\left(1-2\nu_f\right)}{2\mu_f\left(1-\nu_s\right)+2\mu_s\left(1-\nu_f\right)}, \tag{8.10}$$

where the $\bar{E}_i = E_i/\left(1-\nu_i^2\right)$ represent the respective plane-strain moduli, and the $\mu_i = E_i/\left[2\left(1+\nu_i\right)\right]$ represent the respective shear moduli.[172]

The analysis by Beuth does not take into account the effects of interfacial sliding, a phenomenon suggested to occur at the lithiated silicon/copper interface in a number of studies.[94],[96],[159] By allowing for interfacial sliding and using a shear lag approximation, Hu and Evans found that the energy release rate in the steady state takes the form

$$G = \left[\frac{\sigma}{3\tau_o} + F(\Sigma) \right] \frac{\sigma^2 h_f}{E_f}, \tag{8.11}$$

where τ_o is the interfacial sliding strength, $\Sigma = E_f / E_s$, and $F(\Sigma)$ is a function of the elastic mismatch between the film and the substrate, which is analogous to the function $g(\alpha, \beta)$ given in Equation (8.9).

To determine the form of the energy release rate applicable to our experiments, we must first consider the initial flaw size in our experiments. Unfortunately, we do not know the characteristic flaw size created during sputter deposition, and hence it is not possible to use Equation (8.8) directly. To circumvent this issue, each of the thin-film silicon electrodes was scratched with a diamond scribe to introduce imperfections with sizes on the order of the film thickness so that the analysis by Beuth is appropriate.[171] By comparison, the steady state implied in Equation (8.11) is reached only when the crack length approaches the characteristic size of the sliding zone, $l_p = \sigma h / \tau_o$. Using a representative value of $\tau_o = 40$ MPa [159], $l_p \approx 10 \mu m$ in our experiments. Thus, the energy release rate does not approach the expression given in Equation (8.11) until the crack length is much larger than the initial flaw size. Also, the first term in brackets in Equation (8.11) represents the contribution of interfacial sliding. Thus, interfacial sliding only increases the crack

driving force as compared to the analysis of Beuth[172], i.e., the more "difficult" step in the crack propagation process in our experiments is that associated with Equation (8.9).

Using the appropriate expression for the energy release rate (Equation 8.9), we can calculate a bound on the fracture energy of heavily lithiated silicon. Fracture initiates when the energy release rate reaches the fracture energy of the material, $G = \Gamma$, which is bounded by the points corresponding to Figures 8.3a and 8.3b. For the fracture energy measurements at these large concentrations of lithium, we have used the values of E_f measured from initial delithiation (Table 8.1), where a value of $\nu_f = 0.26$ has been assumed.[78] The value of the function $g(\alpha,\beta)$ was determined by interpolating the values reported by Beuth,[172] and was approximately 1.5 in all experiments. The results from four separate experiments are shown in Table 8.1. The quantity *x* in the table represents the range of lithium concentrations over which fracture initially occurred in each test. The mean and standard deviation were found to be $E_f = 32.9 \pm 9.7$ GPa for the modulus, and $\Gamma = 5.4 \pm 2.2 \text{J/m}^2$ to $\Gamma = 6.9 \pm 1.9 \text{ J/m}^2$ for the lower and upper bounds on the fracture energy.

Test #	x in Li_xSi	E (GPa)	Γ (J/m²)
1	3.0 - 3.2	46.1	7.6 – 9.4
2	2.8 - 3.0	23.0	2.4 – 5.6
3	2.4 – 2.6	29.4	6.5 – 7.5
4	2.4 - 2.7	33.0	5.0 – 5.2

Table 8.1. Results of four experiments to determine the fracture energy of lithiated silicon at large concentrations of lithium. The second column represents the range in concentration over which fracture first occurred. The third column is the elastic modulus calculated from initial delithiation of the electrodes. The final column is the calculated range of fracture energies corresponding to the concentration range in the second column.

We have also monitored the morphological development of the cracks in the electrodes (Figure 8.3). Cracks initially form with spacings that are much larger than the thickness of the film (Figures 8.3b, 8.3c). At later stages of delithiation, many more cracks are formed, and the crack spacing approaches the thickness of the film (Figures 8.3d, 8.4). Beuth[172] calculated the change in curvature of the substrate, δK, due to cracks with a characteristic spacing, p, and found

$$\delta K = -\frac{12(1-\nu_s)\sigma h_f^2}{E_s h_s^2 p} g(\alpha,\beta). \tag{8.12}$$

Dividing Equation (8.12) by the curvature calculated from Stoney's Equation (assuming zero curvature for zero stress) gives the relative contribution of the cracks to the curvature:

$$\frac{\delta K}{K} = -2g(\alpha,\beta)\frac{h_f}{p}. \tag{8.13}$$

From Equation (8.13) it is evident that cracks tend to decrease the curvature (we have taken a positive sign as indicating the curvature created by tension in the film). Also, the contribution from the cracks is insignificant until the crack spacing approaches a few times the thickness of the film. We note that the analysis presented in Equations (8.12-8.13) does not include the effects of sliding. However, such effects will not be significant until the crack spacing approaches the length of the sliding zone, $l_p = \sigma h/\tau_o$, which is approximately 10μm for our experiments.[159] The crack spacings shown in Figure 8.3c are on the order of hundreds of microns, much larger than the representative length of the sliding zone. Thus, we believe that cracks such as those in Figure 8.3c still do not significantly affect the curvature of the

substrate. Instead, only the cracks formed at the latest stages of delithiation (Figures 8.3d, 8.4), with spacings on the order of 1-2 μm, affect the stress measured from the substrate curvature technique. As a result, one can identify the lithium concentration at which extensive additional cracking occurs by locating the point at which the apparent tensile stress starts to decrease, i.e., the concentration marked by the green arrow in Figure 8.2b. From this point, we gain an additional measurement of the fracture energy of lithiated silicon at small concentrations of lithium from the same test. The results of these measurements are shown in Table 8.2 for the same four tests that were listed in Table 8.1. In these calculations, the values for the elastic moduli are taken from Reference [117] since we did not measure the moduli at these concentrations in our experiments.[117] The quantity x in Li_xSi in Table 8.2 represents the lithium concentration corresponding to the maximum curvature. Using this technique, the mean value of the fracture energy at this lower concentration of lithium is $\Gamma = 8.5 \pm 4.3$ J/m^2.

Test #	x in Li_xSi	E (GPa)	Γ (J/m²)
1	0.33	50	14.9
2	0.73	30	6.6
3	0.86	34	7.0
4	1.01	36	5.4

Table 8.2. Results of four experiments to determine the fracture energy of lithiated silicon at small concentrations of lithium. The second column lists the lithium concentrations corresponding to the maximum tensile stress (green arrow in Figure 8.2b). The third column is the elastic modulus taken from Reference [117]. The final column contains the fracture energies calculated corresponding to maximum tensile stress.

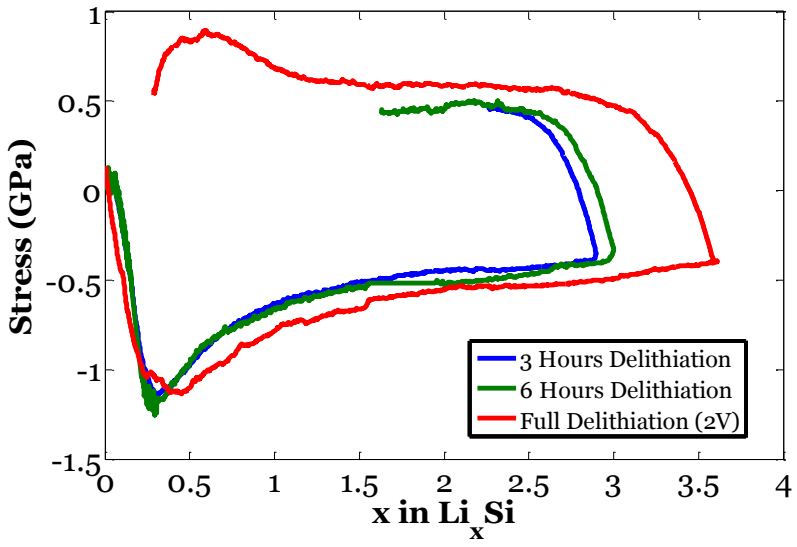

Figure 8.5. Responses in stress as a function of lithium concentration from galvanostatic tests of individual 325 nm silicon electrodes. The electrodes corresponding to each test are delithiated to different extents to determine the fracture energy.

In addition to these experiments, we performed a few tests on individual silicon electrodes in a standard three-electrode arrangement. The results of three such tests are shown in Figure 8.5. These tests were performed at the same conditions as previously discussed. In particular, the electrodes were lithiated galvanostatically at a current density of $15\,\mu A/cm^2$ to a cutoff potential of 0.01 V. The three tests vary in the extent to which they are allowed to delithiate. In the first test, the electrode is delithiated for three hours, and no fracture is observed (similar to Figure 8.3a). In the second test, the electrode is delithiated for six hours, and some fracture is seen (similar to Figure 8.3b). In the third test, the electrode is fully delithiated to a cutoff potential of 2 V, and extensive fracture is seen (similar to Figure 8.3d). Following the previously discussed procedure, we can quantify the fracture energy. This set of experiments yields a bound on the fracture energy of $\Gamma = 7.5 - 8.7\,J/m^2$ in the concentration range of $Li_{1.6}Si$-$Li_{2.3}Si$ and a fracture energy of $\Gamma = 14.7\,J/m^2$ for

$Li_{0.6}Si$. Although on the higher end of the spectrum, these values fall within the range of values shown in Tables 8.1 and 8.2 for the experiments performed on multiple electrodes.

It is important to note that Equation (8.9) invokes an analysis from elasticity, while Figure 8.2b suggests that lithiated silicon is capable of plastic flow. The applicability of linear elastic fracture mechanics to lithiated silicon is an open question. According to the theory established for metals, linear elastic fracture mechanics is applicable when the plastic zone at the front of the crack is much smaller than the feature size of the specimen.[173] The plastic zone size is estimated by[173]

$$r_p = \frac{1}{3\pi}\frac{\Gamma \bar{E}_f}{\sigma_Y^2}. \tag{8.14}$$

Using the average values measured from these experiments, we calculate plastic zone sizes of $r_p = 10\,\text{nm}$ for ~$Li_{2.8}Si$ and $r_p = 40\,\text{nm}$ for ~$Li_{0.7}Si$. The thicknesses at these concentrations are $900\,\text{nm}$ and $450\,\text{nm}$, respectively. Thus, the plastic zone size is significantly smaller than the thickness of the film. It is also interesting to note that the cracks in lithiated silicon show features typical of brittle fracture (Figures 8.3 and 8.4). In particular, Figure 8.4 shows that the faces of the cracks are quite flat and perpendicular to the substrate. These images of brittle fracture may be contrasted with those of a ductile copper film on a polymer substrate.[174],[175] In the latter case, large plastic deformation (e.g., local thinning of the film) is visible in the copper film, which resists the formation of brittle cracks. To reconcile the experimental observations of plastic flow during lithiation and brittleness during fracture in

lithiated silicon, we surmise that once the cracks begin propagating, they move fast relative to the mechanisms associated with plastic deformation in this system. That is, lithiated silicon is essentially elastic during the fracture process. Under this scenario, the analysis from linear fracture mechanics associated with Equation (8.9) is valid.

It is also interesting to compare the values measured in this study to those found in literature for pure silicon. For instance, Ballarini et al. found the critical stress intensity factor for amorphous silicon to be $K_{IC} = 1 \text{MPa}\sqrt{\text{m}}$.[176] This value was calculated assuming a value $E = 160 \text{GPa}$ in their finite element simulations.[176] Using this value for the modulus gives a fracture energy of $\Gamma = K_{IC}^2 / E = 6.3 \text{ J/m}^2$ for amorphous silicon. Likewise, values for fracture energy of single-crystal silicon are in the range of $3-9 \text{ J/m}^2$ [177] and comparable values can be found for bulk polycrystalline silicon.[178] Remarkably, the values for the fracture energy of pure silicon are quite comparable to the measured values for lithiated silicon at both small and large concentrations of lithium. Atomistic simulations have suggested that lithium insertion into silicon results in continuous breaking and re-forming of Si-Si bonds, resulting in a decrease in strength and an increase in ductility.[92] As a result, one might expect that lithium insertion into silicon may drastically alter the fracture energy. The current experimental study suggests, however, that the fracture energy of lithiated silicon is not very different from pure silicon and does not vary substantially with lithium concentration. This finding is consistent with the SEM observations, which show characteristics of brittle fracture. If the fractured surfaces in lithiated silicon had shown features typical of ductile fracture, we would expect the fracture

energy to be much larger than that of pure silicon. It appears that lithiated silicon has a peculiar ability to both flow plastically and fracture in a brittle manner. The mechanism causing this unique combination of properties warrants future investigation.

8.4 Summary

We have devised a novel method to electrochemically cycle multiple thin-film electrodes in parallel, while simultaneously measuring the film stress. We also monitored the morphological development of cracks by optical microscopy, which shows that cracks initially form and widen upon further delithiation, likely by a sliding mechanism as suggested in literature. This procedure allowed us to quantify the fracture energy of lithiated silicon. The fracture energy was determined to be $\Gamma = 8.5 \pm 4.3$ J/m^2 at small concentrations of lithium (~$Li_{0.7}Si$) and to have bounds of $\Gamma = 5.4 \pm 2.2$ J/m^2 and $\Gamma = 6.9 \pm 1.9$ J/m^2 at large concentrations of lithium (~$Li_{2.8}Si$). These numbers are essential for mechanical models and can enable practical design of silicon electrodes that avoid mechanical degradation. The fracture energy does not vary significantly with lithium concentration and is not very different from pure silicon. We hope this work will provide guidance for practical design of silicon electrodes as well as motivate future modeling of lithiated silicon's unique ability to flow plastically, but fracture in a brittle manner.

Chapter 9

Variation of Stress with Charging Rate due to Strain-Rate Sensitivity of Silicon Electrodes

9.1 Introduction

A number of questions remain in regards to the nature of plasticity in Li_xSi. For instance, in Chapter 8, we measured the fracture energy of lithiated silicon thin films, finding that lithiated silicon demonstrates a peculiar ability to both flow plastically and fracture in a brittle manner.[15] However, we did not speculate as to the physics governing this curious combination of properties. Also, Brassart and Suo have suggested that inelasticity in high-capacity lithium-ion batteries may occur by two processes: flow and reaction.[185] The authors define "flow" as a process driven by deviatoric stress that preserves lithium concentration and volume, similar to plastic flow in a metal. By comparison, the authors define "reaction" as lithium insertion/removal: a process that changes the composition and volume of the electrode.[185] One result of their theory is that lithium insertion (or removal) may enable flow at a lower stress than that needed for flow under pure mechanical loading. The applicability of this "reactive flow" theory to a-Li_xSi remains an open question. A study from first-principles calculations found the lithiation reaction to markedly reduce the flow stress of lithiated silicon,[146] while a molecular dynamics study found no such effects.[182] There are no experimental studies aimed at directly investigating these effects.

The purpose of this chapter is to provide experimental insight into the nature of plasticity in a-Li_xSi. To do so, we vary the charging rate in amorphous silicon thin-film electrodes, while simultaneously measuring stresses. The magnitude of the flow stress increases monotonically with the charging rate, indicating that rate-sensitive plasticity occurs at room temperature and at charging rates typical of lithium-ion batteries. These data fit well to a power law relationship between the plastic strain rate and the stress. Additionally, our results indicate no evidence of the "reactive-flow" effect in a-Li_xSi, as has been suggested in literature.[146],[185] They do, however, provide insight into the unusual ability of a-Li_xSi to flow plastically, while fracturing in a brittle manner.

9.2 Experimental procedure and results

Cover glass substrates with a thickness of 175 μm were cleaned with acetone and isopropanol and placed into a sputter deposition system (AJA Int. ATC 1800) with a base pressure of $<10^{-8}$ Torr. All sputtering targets have a 50.8 mm diameter, and depositions were performed at room temperature (22°C). The samples were plasma-cleaned in Ar at 20 mTorr and an RF power of 24 W for 5 minutes. Next, 15 nm of Ti was sputtered onto the substrates using a pressure of 3 mTorr of Ar and a DC power of 100 W for 5 minutes. A 300 nm layer of Cu was then deposited on the Ti underlayer using a pressure of 5 mTorr of Ar and a DC power of 100 W for 15 minutes. The Cu film serves as current collector, while the Ti underlayer is used to improve the adhesion between the Cu film and the glass substrate. Finally, a 100 nm Si film was

deposited on the Cu current collector using a pressure of 5 mTorr of Ar and a DC power of 100 W for 27 minutes. The thickness of the film was verified using profilometry, and was found to be 100 ± 10 nm. The working area of each silicon electrode is 8 mm by 30 mm. We have previously performed x-ray diffraction experiments to confirm that the silicon films are amorphous under these sputtering conditions.[146]

Electrochemical experiments were conducted in a custom-fabricated hermetic Teflon electrochemical cell with a glass window. The cell was assembled in a three-electrode configuration in an argon-filled glovebox, which was maintained at < 1 ppm moisture. The sputtered silicon film was used as the working electrode, and Li foil was used as the reference electrode and the counter electrode. A 1M solution of $LiPF_6$ in 4:3:3 (vol %) ethylene carbonate : dimethyl carbonate : diethyl carbonate with a vinylene carbonate additive was used as the electrolyte (MTI Corporation). Electrochemical measurements were performed with a VersaSTAT 3 galvanostat from Princeton Applied Research. During the first cycle, the cell was tested galvanostatically at a current density of 23.6 $\mu A/cm^2$ (a C/8 rate assuming a capacity of 3579 mAh/g[164]) between 0.8 and 0.05 V vs. Li/Li^+. The lower cutoff potential of 50 mV vs Li/Li^+ was employed to prevent crystallization of the a-Li_xSi electrodes.[122] Relatively thin films (100 nm) and an upper cutoff potential of 0.8 V vs Li/Li^+ were employed to prevent fracture during delithiation. During the second cycle, the cell was lithiated at a C/8 rate for one hour, followed by a number of segments with different charging rates. The duration of these segments was fixed such that the total

capacity during each segment was 50 mAh/g (1.4% of the total capacity of 3579 mAh/g). The relatively slow charging rates used in these experiments were selected to allow enough time for diffusive equilibrium through the films.[78],[156],[168] We use the data measured during the second cycle to minimize effects of SEI growth.[156] Stresses were measured during electrochemical cycling using the substrate curvature method, as described in detail in Section 8.2.

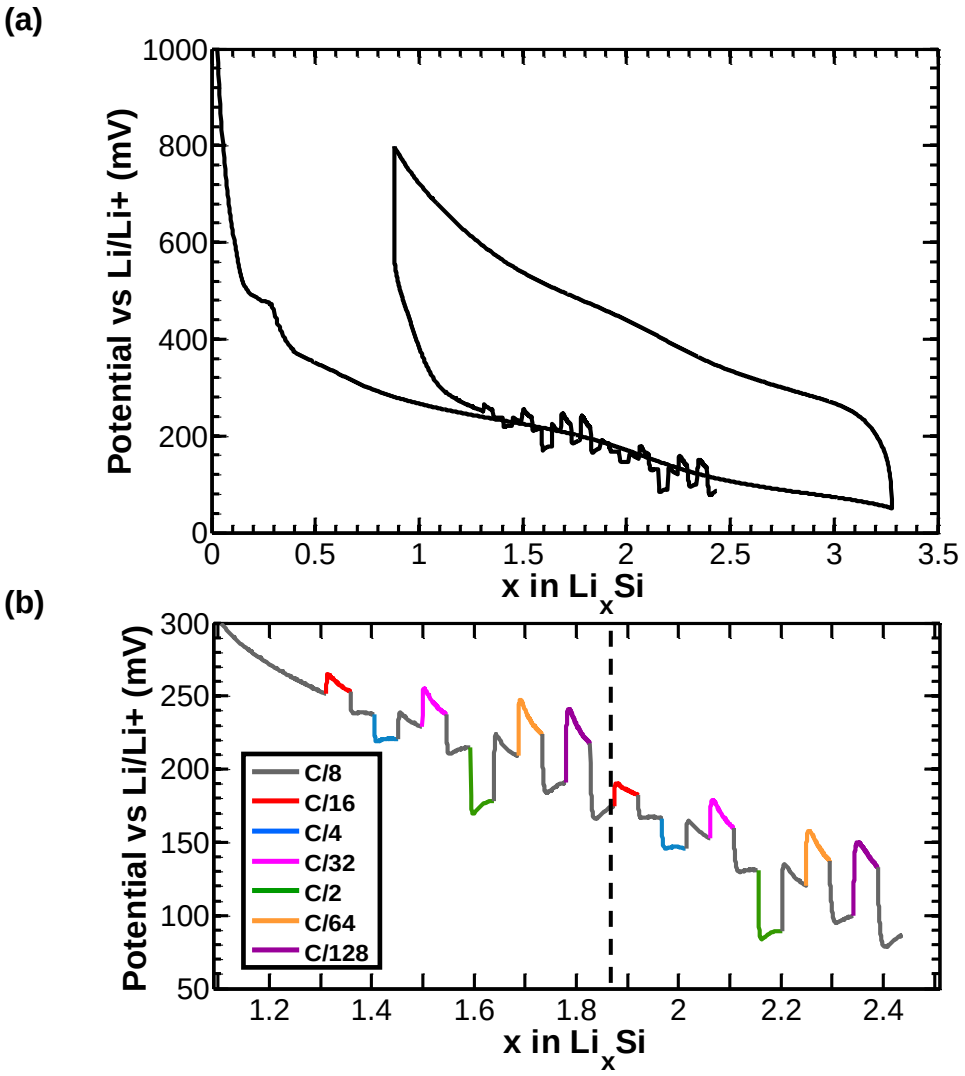

Figure 9.1. Results of electrochemical cycling of a 100 nm Si thin-film electrode. (a) Measured potential as a function of lithium concentration. (b) A zoomed-in view that focuses on the second lithiation. The vertical dashed line indicates the point at which the set of charging rates is repeated.

Figure 9.1 shows a typical sequence of the applied charging rate and the response in the measured voltage. During the second lithiation, an increase in the charging rate results in a decrease in the voltage, as is normally observed in Li_xSi electrodes. We should note that the horizontal axis in the figure is constructed by integrating the current during the experiment to get the total charge. The amount of charge does not necessarily represent the concentration of lithium in silicon, as SEI formation may consume lithium during the first cycle. However, the main focus of this chapter is related to the stress measurements as a function of charging rate (as shown in Figure 9.2). The stress data collected in these experiments were obtained during the second cycle. Using the second cycle minimizes the influence of the SEI on our data, as the majority of the SEI is formed during the initial lithiation.[156]

Figure 9.2 shows the stress measured in the film subject to the electrochemical cycling shown in Figure 9.1. Figure 9.2b is a zoomed-in view that focuses on the second lithiation. The legend shows the charging rate during each segment as expressed in the C-rate convention. In this convention, the denominator indicates the number of hours to theoretically fully lithiate the electrode. Figure 2b thus demonstrates that increasing the rate of lithiation, e.g., from C/128 to C/8, results in a quick and sustained increase in the magnitude of the stress (the stress becomes more compressive). Likewise, when the charging rate increases, but by a smaller amount, e.g., from C/16 to C/8, the stress increases in magnitude, but not as much as compared to, e.g., C/128 to C/8. In other words, the change in stress increases monotonically with charging rate – faster charging results in larger stress.

We believe that these observations are indicative of a material rate-effect, i.e., plastic deformation of a-Li_xSi is rate sensitive, even at room temperature.

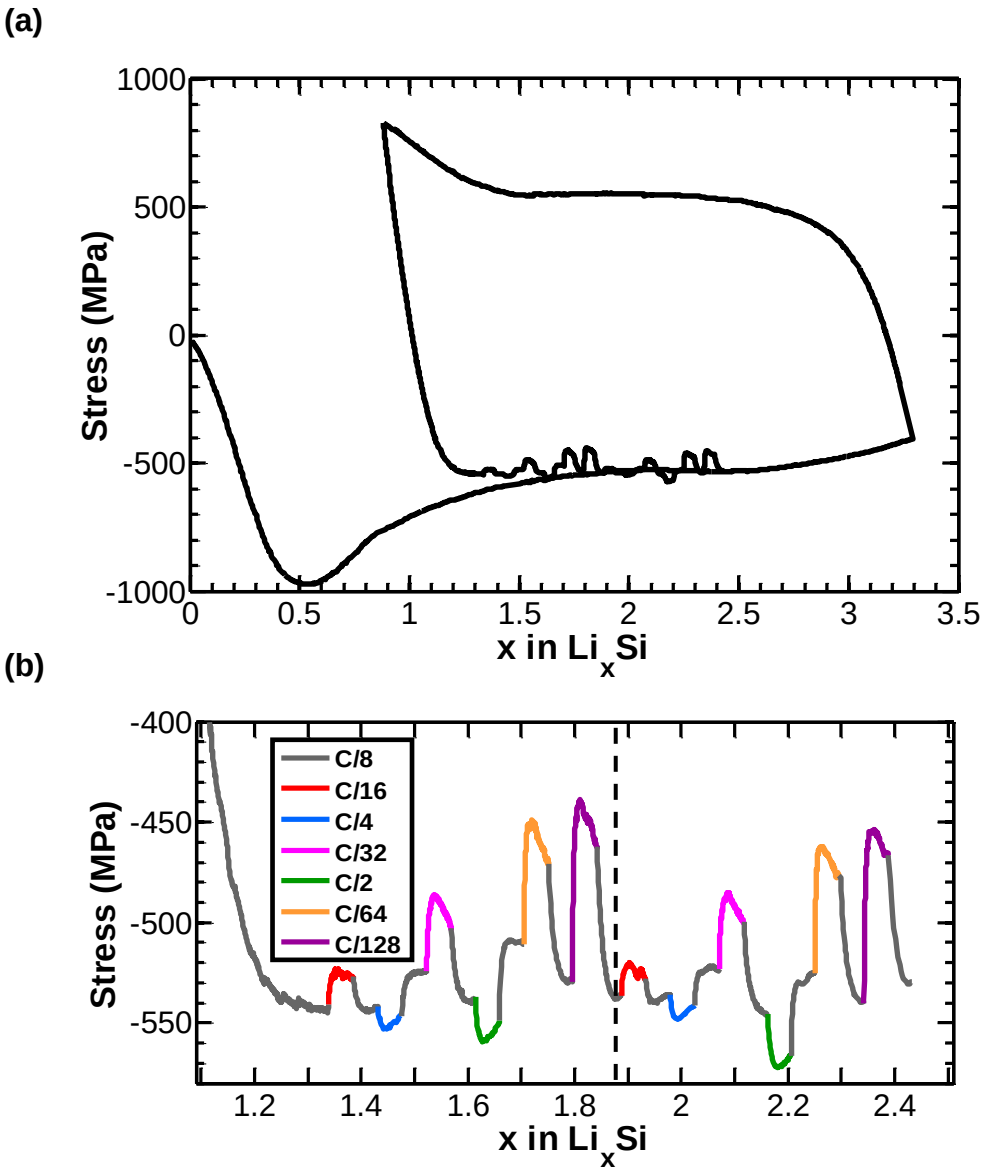

Figure 9.2. (a) Stress measured in the 100 nm thin-film Si electrode subject to the electrochemical cycling conditions shown in Figure 9.1. (b) A zoomed-in view that focuses on the second cycle. The vertical dashed line indicates the point at which the set of charging rates is repeated. A change in the charging rate results in a significant change in the stress.

9.3 A model of concurrent lithiation and rate-sensitive plasticity

We will now outline a simple mechanical model, with the goal of extracting creep material parameters from our experiments. The model extends our previously developed models to account for rate-sensitive plasticity,[15],[91],[115] and is similar to that of Bucci et al.[190] Following these models,[15],[91],[115],[190] we take the deformation to consist of contributions from elasticity, plasticity, and lithiation-induced swelling. The total true strain, ε_{ij}, can be written as

$$\varepsilon_{ij} = \varepsilon_{ij}^{L} + \varepsilon_{ij}^{E} + \varepsilon_{ij}^{P}, \tag{9.1}$$

where ε_{ij}^{L} represents the true lithiation-induced strain, ε_{ij}^{E} represents the true elastic strain, and ε_{ij}^{P} represents the true plastic strain. For a thin film on a thick substrate, the state of stress is equi-biaxial, $\sigma_{11} = \sigma_{22} = \sigma$, with all other components vanishing. Due to the constraint of the substrate, the total in-plane components vanish, $\varepsilon_{11} = \varepsilon_{22} = \varepsilon = 0$. Equation (9.1) becomes:

$$\varepsilon^{L} + \varepsilon^{E} + \varepsilon^{P} = 0, \tag{9.2}$$

where the ε represent the in-plane components of the true strains.

Following our previous work,[15] and validated by experiments,[15],[164]-[166] we take the volume of the film, V_f, to be linear in the state of charge:

$$V_f = V_f^{0}\left(1 + \beta s\right), \tag{9.3}$$

where V_f^{0} is the initial volume of the film, β is related to the atomic volumes (Ω) by $\beta = \left(\Omega_{Li3.75Si} - \Omega_{Si}\right)/\Omega_{Si}$, and s is the state of charge, with a value of 0 representing pure silicon and a value of 1 representing the fully lithiated state (assumed to be a-$Li_{3.75}Si$ with a capacity of 3579 mAh/g).[164]

Due to the amorphous nature of Li_xSi, the lithiation-induced deformation is assumed to be isotropic, such that the stretch ratios are equal, $\lambda_1^L = \lambda_2^L = \lambda_3^L = \lambda^L$. As in Chapter 8, we take $\lambda^L = (1+\beta s)^{1/3}$. By definition, the in-plane component of the true lithiation-induced strain is $\varepsilon^L = \ln(\lambda^L)$, such that

$$\varepsilon^L = \frac{1}{3}\ln(1+\beta s). \tag{9.4}$$

The elastic strains are given by Hooke's law:

$$\varepsilon^E = \frac{1-\nu_f}{E_f}\sigma, \tag{9.5}$$

where υ_f is Poisson's ratio of the film, E_f is the elastic modulus of the film, and σ is the in-plane component of the true (Cauchy) stress in the film.

The in-plane component of the true plastic strain will be left in a generalized form,

$$\varepsilon^P = \ln(\lambda^P). \tag{9.6}$$

Combining Equations (9.2) and (9.4 – 9.6), and taking a time-derivative, we get

$$-\frac{1}{\lambda^P}\frac{d\lambda^P}{dt} = \frac{d}{dt}\left[\frac{1-\nu_f}{E_f}\sigma\right] + \frac{\beta}{3(1+\beta s)}\frac{ds}{dt}. \tag{9.7}$$

In our experiments, the charging rate, *ds*/*dt*, is prescribed, and the stress is measured as a function of time. Thus, with knowledge of the material properties of the film (ν_f, E_f, and β), the plastic strain rate in our experiments, $\frac{1}{\lambda_P}\frac{d\lambda^P}{dt}$, can be calculated as a function of time.

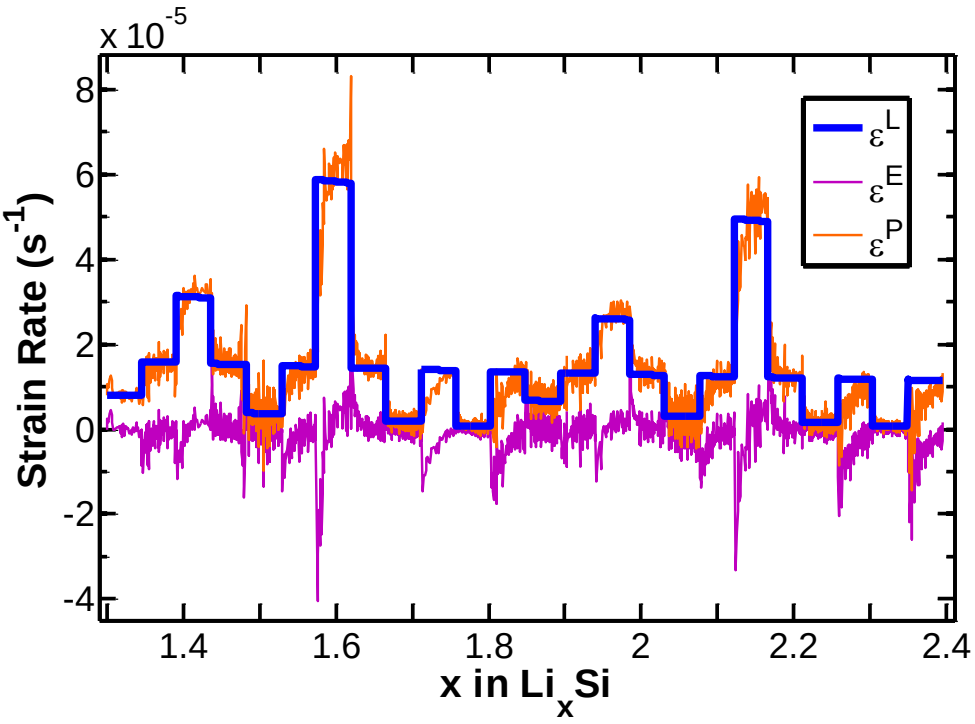

Figure 9.3. Components of the strain rate in the 100 nm thin-film Si electrode subject to the electrochemical cycling conditions shown in Figure 9.1. The thick blue line indicates the prescribed lithiation-induced strain rate, $\varepsilon^L = \beta/\left[3(1+\beta s)\right]\cdot ds/dt$. The thin purple line indicates the elastic component of the strain rate, $\varepsilon^E = \left(1-\nu_f\right)/E_f \cdot d\sigma/dt$. The thin orange line represents the plastic component of the strain rate, $\varepsilon^P = -1/\lambda^P \cdot d\lambda^P/dt$, as calculated from Equation (9.7).

Figure 9.3 shows the experimental values of the terms in Equation (9.7) subject to the electrochemical cycling conditions of Figure 9.1. The elastic component of the strain rate is calculated using a representative value of the biaxial modulus of $E_f/\left(1-\nu_f\right) = 45$ GPa, as reported in by Sethuraman et al.[117] In their study, they found this quantity to vary only slightly with lithium concentration over the range of concentrations examined in our studies; thus, in constructing Figure 9.3, we take the biaxial modulus as a constant. The lithiation-induced strain rate is calculated using the prescribed charging rate, $\left(ds/dt\right)$, and a value of $\beta = 2.8$, as

previously discussed. The plastic component of the strain rate is then computed using Equation (9.7). As can be seen from Figure 9.3, during the majority of our experiments, the elastic component of the strain rate is small compared to the lithiation-induced strain rate, thereby eliminating the need to know the value of the biaxial modulus to calculate the plastic strain rate. In this limit, Equation (9.7) becomes

$$-\frac{1}{\lambda^P}\frac{d\lambda^P}{dt}=\frac{\beta}{3(1+\beta s)}\frac{ds}{dt}. \tag{9.8}$$

Equation (9.8) has a straightforward physical interpretation: the plastic strain rate in the experiments is directly prescribed by the charging rate. By increasing the charging rate, we correspondingly impose an increased rate of plastic strain.

Combining our stress measurements with Equation (9.8), we can obtain a relationship between the rate of plastic strain and the stress in the a-Li_xSi, thereby extracting material parameters. In particular, we fit to our data to a typical viscoplastic power-law:[191],[192]

$$-\frac{1}{\lambda^P}\frac{d\lambda^P}{dt}=A\left[\frac{\sigma-\sigma_Y}{\sigma_Y}\right]^m, \tag{9.9}$$

where A, m, and σ_Y are fitting parameters. In this equation, σ_Y can be interpreted as the yield stress of the material at a vanishing plastic strain rate. Equation (9.9) is only applicable when the stress exceeds σ_Y. In the equation, σ represents the magnitude of the measured stress (a positive quantity), and the leading negative sign is a result of the compressive stress state during lithiation. One complicating factor in our experiments is that the yield stress varies with the

state of charge, as can be seen in the first cycle in Figure 9.2. To mitigate this complication, we have performed the strain-rate experiment over a concentration range in which the yield stress changes slowly with lithium concentration (Figure 9.2).

Upon changing the charging rate from the nominal rate of C/8 to a different rate (e.g., C/16), the stress quickly progresses toward a new value (Figure 9.2b). To use these data, we rewrite Equation (9.9) in a convenient form:

$$-\frac{1}{\lambda^P}\frac{d\lambda^P}{dt} = A\left[\frac{\left(\sigma-\sigma_{C/8}\right)-\left(\sigma_{C/8}-\sigma_Y\right)}{\sigma_{C/8}-\left(\sigma_{C/8}-\sigma_Y\right)}\right]^m, \tag{9.10}$$

where $\sigma_{C/8}$ represents the stress at the nominal charging rate of C/8, and all of the stresses represent the magnitude of the measured stresses (positive quantities). We assume that the quantity $\left(\sigma_{C/8}-\sigma_Y\right)$ is a constant, independent of the lithium concentration over the range of concentrations considered in the experiments. After each change in the charging rate, we measure the quantity $\left(\sigma_{C/8}-\sigma_Y\right)$. We also measure the quantity $\sigma_{C/8}$ immediately before (or after) each change in the charging rate. During the experiment, the charging rate, and hence the plastic strain rate (Equation 9.8) is prescribed as a function of time. Thus, we obtain a set of data to which we can fit Equation (9.10) using the quantities A, m, and $\left(\sigma_{C/8}-\sigma_Y\right)$ as fitting parameters.

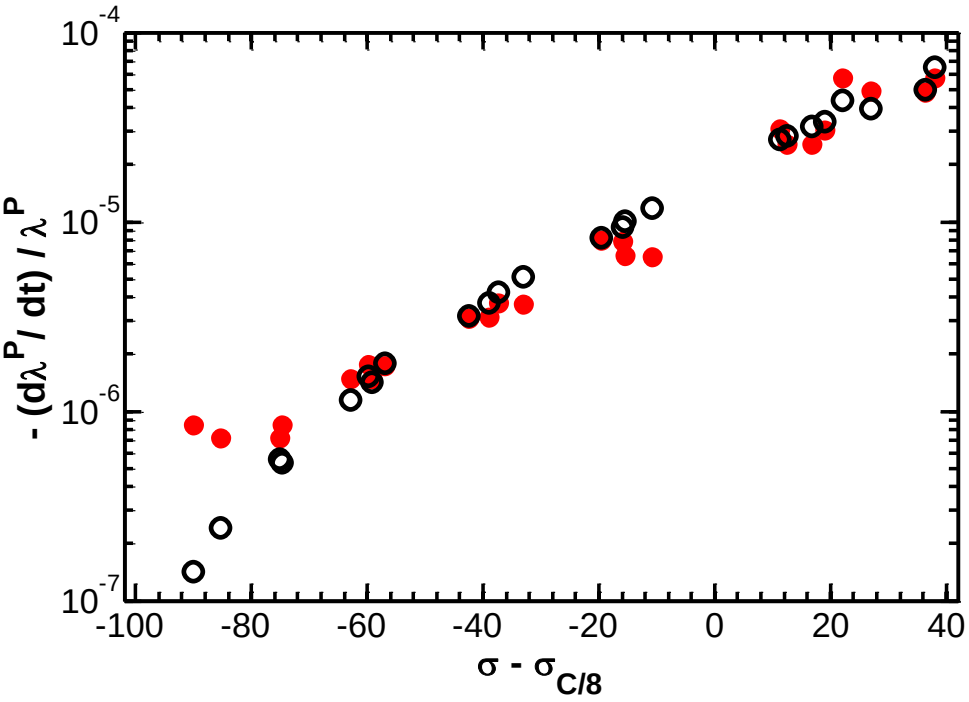

Figure 9.4. Plastic strain rate (in units of 1/s) versus the change in measured stress relative to the C/8 rate (in units of MPa). The solid red circles represent the experimental data and the open black circles represent the phenomenological model in Equation (9.10).

Figure 9.4 shows the best fit of Equation (9.10) to the data from the experiment corresponding to Figure 9.2. As is evident from Figure 9.4, the power-law form represents the data well. The results of the best fits for three such experiments are shown in Table 9.1. The exponent m, has values in the range of 2.58 - 4.07. For large values of m, the stress level is insensitive to the applied strain rate and is instead limited by the yield strength, σ_Y. In our experiments, the measured values of m demonstrate a moderate level of strain-rate sensitivity.

A (1/s)	m	$\sigma_{C/8} - \sigma_Y$ (MPa)	R^2
0.00175	4.07	130	0.947
0.00230	2.94	94.1	0.937
0.00168	2.58	82.9	0.892

Table 9.1. Results of the fit of the experimental data to Equation (9.10) for three separate experiments.

As a final note, this experimental technique could be used to measure rate-sensitive material properties as a function of lithium concentration by repeating the outlined procedure at various states of charge. In our experiments, we subject the film to the same set of (nominal) charging rates twice (Figure 9.2b). There is little variation in the extracted material parameters from each set of charging rates. It is of course possible that these properties could vary with the state of charge if we were to study a larger range of lithium concentrations; such work was not pursued in this chapter.

9.4 Discussion

Our results indicate that a-Li_xSi electrodes are rate sensitive at room temperature and that the rate effect is important at charging rates typically used in lithium-ion batteries. These observations have significant ramifications for the rate-capabilities of silicon anodes. In particular, due to the strain-rate sensitivity, faster charging will result in larger stresses, which may result in fracture of the electrode.

We should mention that a recent work by Boles et al. has investigated creep deformation in lithiated silicon.[193] In their work, constant-force creep tests were conducted on fully lithiated c-$Li_{15}Si_4$ nanowires. Their investigation was primarily performed at stress levels below the apparent yield stress of the material. Interestingly, at these low stress levels, the authors found a linear relationship between the strain rate and the stress, suggesting Newtonian viscous flow of

c-$Li_{15}Si_4$.[193] The nanowires tested by Boles et al. are polycrystalline; thus, the grain boundaries may allow diffusional transport as well as creep deformation.[193] Moreover, their testing of the crystalline phase allows for the possibility of creep deformation via dislocation motion. In this chapter, we focus on quantifying the relationship between the charging rate and the resulting stresses during electrochemical cycling of a-Li_xSi. We use charging rates typical of lithium-ion batteries and examine a range of lithium concentrations. We also limit the depth of discharge in this study to investigate amorphous electrodes, which are typically used in practice due to their improved cycling performance.[122] Since the material is amorphous, there are no dislocations. Even so, we observe a significant rate effect. Due to the large strains associated with lithiation/delithiation, stresses in Li_xSi electrodes readily reach the yield stress during cycling. At these large stresses, different from Boles et al., we observe a non-linear relationship between the stress and the strain rate. Our results can answer a number of open questions in literature, as will now be discussed.

Our observations of rate-sensitive plasticity in a-Li_xSi shed light on recent theories and experiments. For instance, Soni et al. found fracture only at large charging rates $\geq C/2$ in 150 nm silicon thin films.[188] The authors attributed this observation to diffusion limitations through the thickness of the film.[188] It is also possible that their observations are due to effects of rate-sensitive plasticity: for the range of charging rates used in our experiments (C/128 to C/2), the stresses varied by over 100 MPa. These variations in stress will significantly alter the driving force for

fracture, as the energy release rate scales with the square of the stress. Thus, substantially larger crack-driving forces develop at larger charging rates, potentially leading to fracture.

As another example, Brassart and Suo have suggested that inelasticity in batteries may occur by two processes: flow and reaction.[185] "Flow" changes the shape of the electrode while preserving volume and lithium concentration, and is driven by the deviatoric stress — a process similar to plastic flow in a metal. By contrast, "reaction" (i.e., lithium insertion/removal) changes both volume and lithium concentration.[185] These two processes, flow and reaction, are intimately coupled as they both involve the same physical processes: breaking and forming atomic bonds. As a result of this chemo-mechanical coupling, larger overpotentials (i.e., larger chemical driving forces) can result in flow at a smaller stress.[185] In our experiments, larger charging rates result in larger overpotentials. Thus, in the absence of any other rate effects, Brassart and Suo would predict a decrease in the magnitude of the flow stress with increasing charging rate. In contrast, we see the exact opposite trend in our experiments – larger charging rates result in an increase in the magnitude of the flow stress. Therefore, as previously discussed, we believe that our results are indicative of a material rate effect: a-Li_xSi is strain-rate sensitive. Larger charging rates result in larger strain rates in the material, which in turn generate larger stresses. We should note, however, that our experiments do not entirely preclude the existence of the so-called "reactive flow" effects discussed by Brassart and Suo. It is possible that these effects do indeed exist, but that they are

too small relative to the strain-rate dependence of the material to be observed in our experiments.

As another example, in Chapter 8, we have suggested that a-Li_xSi demonstrates a peculiar ability to both flow plastically and fracture in a brittle manner.[15] We did not speculate as to the physics governing this curious combination of properties. However, when a crack propagates in a-Li_xSi, it moves relatively fast, resulting in large strain-rates near the crack tip. In this chapter, we provide evidence for rate-sensitivity of a-Li_xSi: plastic flow at larger strain-rates requires larger stresses. Consequently the strains associated with fracture are mostly elastic, and the material fails in a brittle fashion, in agreement with fractographic observations and justifying the use of linear elastic fracture mechanics as employed in Chapter 8.

The discussion in this chapter underscores the importance of determining the exact microscopic picture governing plastic flow in a-Li_xSi. Some potential mechanisms have been investigated through computational atomistic simulations. For instance, Zhao, et al. found that continuous bond breaking and re-forming assisted by Li insertion can accommodate large plastic deformation.[139] In another study, Zhao, et al. found bond switching to occur at loosely packed free-volume regions, leading to localized plastic deformation.[189] Such deformation is reminiscent of that found in metallic glasses. It has been established that an applied stress can cause local atomic rearrangement in metallic glasses, resulting in macroscopic deformation. In particular, a flow equation is usually implemented

from transition-state theory, in which the strain-rate scales with the stress as $\dot{\varepsilon} \propto \sinh\left(\tilde{\Omega}\sigma / 2kT\right)$, where $\tilde{\Omega}$ is the activation volume, k is the Boltzmann constant, and T is the temperature.[194]-[196] Over a particular range of stress, this scaling is quite similar to that of Equation 9.9, which was found to describe our data well (Table 9.1). Although this similarity does not definitively point to a particular microscopic mechanism, it suggests that deformation of a-Li_xSi shares some of the same features as metallic glasses. In another atomistic study, Huang and Zhu attributed plastic deformation during lithiation of silicon to a decrease in strong covalent Si-Si bonds and an increase in weak Li-Li bonds.[183] The high mobility of Li atoms facilitates effective bond switching to accommodate mechanical deformation.[183] Thus, it further appears that bond breaking and re-forming, as well as the mobility of lithium are important for plastic deformation of a-Li_xSi. These processes take time and thus engender rate-dependent plasticity. Unfortunately, due to computational limitations of atomistic simulations, the time scales associated with these processes are not well understood. This chapter emphasizes the importance of gaining a better understanding the dynamics of plastic flow in a-Li_xSi, and thus warrants future theoretical and computational studies.

9.5 Summary

We have measured stresses in silicon thin films as a function of the charging rate. Increasing the rate of lithiation resulted in a corresponding increase in the flow stress. Our results indicate that rate-sensitive plasticity occurs in a-Li_xSi at

room temperature and at charging rates typically used in lithium-ion batteries. To extract material parameters, we have developed a model of concurrent lithiation and rate-sensitive plasticity. The data are well described by a power-law relationship between the strain-rate and the stress, with a value of the stress exponent, m, in the range of 2.58 – 4.07, indicating a moderate level of strain-rate sensitivity. These results provide insight into the unusual ability of a-Li_xSi to flow plastically but fracture in a brittle manner. Moreover, the results have direct ramifications concerning the rate-capabilities of silicon anodes. In particular, faster charging rates result in larger stresses, which can lead to fracture of the electrode. We hope that this work will provide guidance for the design of future theoretical models that account for material rate effects. Likewise, we hope that this work will inspire future computational studies aimed at understanding the dynamics of plastic flow in a-Li_xSi.

Chapter 10

Summary

This thesis has explored mechanical behavior of microelectronic devices and lithium-ion batteries. Continuum models were constructed and experiments were performed to investigate these systems. An emphasis was placed on the intimate coupling between mechanics and other fields, such as chemical reactions, electric fields, mass transport, and electrochemistry. Considerations from large deformation, plasticity, creep, kinetics, and fracture mechanics proved necessary for the analysis.

First, we examined electromigration-induced void formation in solder bumps in integrated circuits. Due to their relatively low melting points, solders creep significantly during operation. To account for this phenomenon, we have constructed a theory that couples electromigration and creep. From the theory, an intrinsic length emerged, which characterizes the relative rates of creep and diffusion. When diffusion is slow relative to creep, we found the stress to be relatively small and localized to the boundary of the solder. This theory can predict the critical current density below which voids do not form. Different from metallic interconnects, the critical current density is found to be independent of the solder size and decrease exponentially with increasing temperature. Our numerical predictions agree well with experimental observations in practical solder systems. Thus, our theory can

provide practical guidelines by predicting the conditions necessary to avoid electromigration-induced damage in solders.

We then turned our attention to lithium-ion batteries, examining the interplay between mass transport, deformation, stress, and fracture. We first modeled fracture of elastic electrodes by combining ideas from diffusion kinetics and fracture mechanics. This theory allowed us to construct "fracture maps" capable of predicting conditions to avoid fracture in terms of material properties, particle size, and charging rate. We performed a numerical example that predicts conditions to prevent fracture of a $LiCoO_2$ particle. Next, we examined mechanics of high-capacity lithium-ion batteries, which demonstrate inelastic deformation. To do so, we have constructed a continuum model that accounts for diffusion and elastic-plastic deformation. This model allowed us to calculate both the distribution of lithium and the stress in the host electrode during electrochemical cycling. The model suggests that fracture of high-capacity electrodes can be prevented in small and soft electrode materials that are cycled slowly. Using ideas from this theory, we investigated a promising design for high-capacity lithium-ion batteries: hollow, coated nano-structures. In these structures, we analyzed conditions to prevent fracture of the active materials and debonding between the active and inactive materials.

We also looked at crystalline silicon electrodes, which were found to accommodate lithiation by a two-phase reaction mechanism. To this point, we have constructed a continuum model of concurrent reaction-controlled kinetics and

plasticity. In silicon particles, the model predicted hoop tension in the lithiated phase during lithiation, different from models that incorporate diffusion-controlled kinetics. This prediction agrees with experimental observations of fracture during lithiation of crystalline silicon particles. Also, we found that the stresses generated substantially contribute to the driving force for lithiation. Under certain conditions, we predicted that these stresses will completely shut off the lithiation; this prediction was later confirmed by experiments. To quantify the kinetics of the lithiation process, we performed electrochemical experiments on {100}, {110}, and {111} crystalline silicon wafers. In relation to these experiments, we have presented a kinetic model coupling redox reactions, diffusion, and chemical reactions. The experiments indicated the existence of a moving phase boundary for all three orientations, indicating that short-range processes at the a-$Li_{\eta}Si$ /c-Si interface significantly contribute to the kinetics of the lithiation process. The velocity of this phase boundary was found to be faster for {110} silicon than for the other orientations. Using the measured velocities, we have implemented the model of concurrent reaction and plasticity into ABAQUS. The simulations accurately accounted for anisotropic morphologies and fracture patterns developed in crystalline silicon nanopillars of various axial orientations.

One important parameter in the continuum theories is the fracture energy. In many lithium-ion battery systems, the fracture energy is unknown, and may vary with lithium concentration. Thus, we have developed an experimental technique to measure the fracture energy of high-capacity lithium-ion battery electrodes. We

used this technique to measure the fracture energy of lithiated silicon electrodes as a function of lithium concentration. To do so, we electrochemically cycled multiple thin-film electrodes in parallel, while simultaneously measuring the stress in the film. Subsequently, we monitored the morphological development of cracks by optical microscopy. The fracture energy was determined to be similar to that of pure silicon and to be essentially independent of the lithium concentration. These findings demonstrated that lithiated silicon has a peculiar ability to flow plastically but fracture in a brittle manner. To investigate this interesting combination of properties, we measured stresses in silicon thin films as a function of charging rate. Increasing the rate of lithiation resulted in a corresponding increase in the flow stress, indicating rate-sensitive plasticity, at room temperature and at charging rates typical of lithium-ion batteries. The rate-sensitive material parameters were quantified, providing insight into this unusual ability of lithiated silicon to flow plastically but fracture in a brittle manner. These results have direct ramifications concerning the rate-capabilities of silicon anodes. In particular, faster charging rates result in larger stresses, which can lead to fracture of the electrode.

Bibliography

[1] Blech IA. Electromigration in thin aluminum films on titanium nitride. Journal of Applied Physics 1976; 47: 1203.

[2] Blech IA, Herring C. Stress generation by electromigration. Applied Physics Letters 1976; 29: 131.

[3] Hsiao LY, Duh JG. Intermetallic compound formation and diffusion path evolution in eutectic tin-lead flip chip solder bumps after aging. Soldering & Surface Mount Technology 2006; 18 (2): 18.

[4] Zeng K, Tu KN. Six cases of reliability study of Pb-free solder joints in electronic packaging technology. Materials Science & Engineering R-Reports 2002; 38 (2): 55.

[5] Van den Bossche P, Vergels F, Van Mierlo J, Matheys J, Autenboer W. SUBAT: An assessment of sustainable battery technology. Journal of Power Sources 2006; 162 (2): 913.

[6] Armand M, Tarascon JM. Building better batteries. Nature 2008; 451: 652.

[7] RF Service. Getting there. Science 2011; 332: 1494.

[8] Ellis BL, Lee KT, Nazar LF. Positive Electrode Materials for Li-Ion and Li-Batteries. Chemistry of Materials 2010; 22: 691.

[9] Marom R, Amalraj SF, Leifer N, Jacob D, Aurbach DJ. A review of advanced and practical lithium battery materials. Journal of Materials Chemistry 2011; 21: 9938.

[10] Zhang WJ. A review of the electrochemical performance of alloy anodes for lithium-ion batteries. Journal of Power Sources 2011; 196: 13.

[11] Hu YH, Zhao XH, Suo ZG. Averting cracks caused by insertion reaction in lithium-ion batteries. Journal of Materials Research 2010; 25: 1007.

[12] Zhao KJ, Pharr M, Vlassak JJ, Suo ZG. Fracture of electrodes in lithium-ion batteries caused by fast charging. Journal of Applied Physics 2010; 108: 073517.

[13] Wang HF, Jang YI, Huang BY, Sadoway DR, Chiang YT. TEM study of electrochemical cycling-induced damage and disorder in LiCoO2 cathodes for rechargeable lithium batteries. Journal of the Electrochemical Society 1999; 146: 473.

[14] Wang DY, Wu XD, Wang ZX, Chen LQ. Cracking causing cyclic instability of LiFePO4 cathode material. Journal of Power Sources 2005; 140: 125.

[15] Pharr M, Suo ZG, Vlassak JJ. Measurements of the Fracture Energy of Lithiated Silicon Electrodes of Li-Ion Batteries. Nano Letters 2013; 13 (11): 5570.

[16] Arora P, White RE, Doyle M. Capacity fade mechanisms and side reactions in lithium-ion batteries. Journal of the Electrochemical Society 1998; 145: 3647.

[17] Beaulieu LY, Eberman KW, Turner RL, Krause LJ, Dahn JR. Colossal reversible volume changes in lithium alloys. Electrochemical and Solid State Letters 2001; 4: A137.

[18] Nadimpalli SPV, Sethuraman VA, Dalavi S, Lucht B, Chon MJ, Shenoy VB, Guduru PR. Quantifying capacity loss due to solid-electrolyte-interphase layer

formation on silicon negative electrodes in lithium-ion batteries. Journal of Power Sources 2012; 215: 145.

[19] Tu KN. Recent advances on electromigration in very-large-scale-integration of interconnects. Journal of Applied Physics 2003; 94: 5451.

[20] Yeh ECC, Choi WJ, Tu KN, Elenius P, Balkan H. Current-crowding-induced electromigration failure in flip chip solder joints. Applied Physics Letters 2002; 80: 580.

[21] Korhonen MA, Borgesen P, Tu KN, Li CY. Stress evolution due to electromigration in confined metal lines. Journal of Applied Physics 1993; 73 (8): 3790.

[22] Filippi RG, Biery Ga, Wachnik RA. The electromigration short - length effect in Ti - AlCu - Ti metallization with tungsten studs. Journal of Applied Physics 1995; 78 (6): 3756.

[23] Suo Z. Stable state of interconnect under temperature change and electric current. Acta Materialia 1998; 46 (11): 3725.

[24] Park YJ, Andleigh VK, Thompson CV. Simulations of stress evolution and the current density scaling of electromigration-induced failure times in pure and alloyed interconnects. Journal of Applied Physics 1999; 85 (7): 3546.

[25] Rosenberg R, Edelstein DC, Hu CK, Rodbell KP, Copper Metallization for High Performance Silicon Technology. Annual Review of Materials Science 2000; 30: 229.

[26] Ogawa ET, Lee KD, Blaschke VA, Ho PS. Electromigration reliability issues in

Dual-Damascene Cu Interconnections. Ieee Transactions on Reliability 2002; 51 (4): 403.

[27] He J, Suo Z, Marieb TN, Maiz JA. Electromigration lifetime and critical void volume. Applied Physics Letters 2004; 85 (20): 4639.

[28] Siewert T, Liu S, Smith D, Madeni JC, Database for Solder Properties with Emphasis on New Lead-Free Solders, Properties of Lead-Free Solders, Release 4.0; 2002.

[29] Tribula D, Grivas D, Morris JW, Stress Relaxation in 60Sn-40Pb Solder Joints. Journal of Electronic Materials 1988; 17 (5): 387.

[30] Zhang Z, Suo ZG, He J. Saturated voids in interconnect lines due to thermal strains and electromigration. Journal of Applied Physics 2005; 98 (7): 074501.

[31] Suo Z. A continuum theory that couples creep and self-diffusion. Journal of Applied Mechanics-Transactions of the ASME 2004; 71: 646.

[32] Darken LS. Diffusion, Mobility, and their Interaction Through Free Energy in Binary Metallic Systems. Transactions of the American Institute of Mining and Metallurgical Engineers 1948; 175: 184.

[33] Lee TY, Tu KN, Kuo SM, Frear DR. Electromigration of eutectic SnPb solder interconnects for flip chip technology. Journal of Applied Physics 2001; 89: 3189.

[34] Xu LH, Pang JHL, Tu KN. Effect of electromigration-induced back stress gradient on nanoindentation marker movement in SnAgCu solder joints. Applied Physics Letters 2006; 89: 221909.

[35] Balluffi RW. The Supersaturation and Precipitation of Vacancies during Diffusion. Acta Metallurgica 1954; 2: 194.

[36] Balluffi RW, Seigle LL. Effect of Grain Boundaries upon Pore Formation and Dimensional Changes during Diffusion. Acta Metallurgica 1955; 3: 170.

[37] Daruka I, Szabo IA, Beke DL, et al. Diffusion-induced bending of thin sheet couples: Theory and experiments in Ti-Zr system. Acta Materialia 1996; 44: 4981.

[38] Suo Z, Kubair DV, Evans AG, Clarke DR, Tolpygo VK. Stresses induced in alloys by selective oxidation. Acta Materialia 2003; 51: 959-974.

[39] Huntington HB, Grone AR. Current-Induced Marker Motion in Gold Wires. Journal of Physics and Chemistry of Solids 1961; 20: 76.

[40] Chuang TJ, Kagawa KI, Rice JR, Sills LB. Non-Equilibrium Models for Diffusive Cavitation of Grain Interfaces. Acta Metallurgica 1979; 27 (3): 265.

[41] Wiese S, Wolter KJ. Microstructure and creep behaviour of eutectic SnAg and SnAgCu solders. Microelectronics Reliability 2004; 44 (12): 2004.

[42] Lee TY, Tu KN, Kuo SM, Frear DR. Electromigration of eutectic SnPb solder interconnects for flip chip technology. Journal of Applied Physics 2001; 8 (9): 3189.

[43] Coston C, Nachtrieb NH. Journal of Physical Chemistry 1964; 68 (8): 2219.

[44] Lu MH, Shih DY, Lauro P, Goldsmith C. Blech effect in Pb-free flip chip solder joint. Applied Physics Letters 2009; 94: 011912.

[45] Kaban I, Mhiaoui S, Hoyer W, Gasser JG. Surface tension and density of binary

lead and lead-free Sn-based solders. Journal of Physics-Condensed Matter 2005; 17: 7867.

[46] Hsu YC, Chou CK, Liu PC, Chen C, Yao DJ, Chou T, Tu KN. Electromigration in Pb-free SnAg3.8Cu0.7 solder stripes. Journal of Applied Physics 2005; 98: 033523.

[47] Yoon MS, Ko MK, Kim BN, Kim BJ, Park YB, Joo YC. Line length dependence of threshold current density and driving force in eutectic SnPb and SnAgCu solder electromigration. Journal of Applied Physics 2008; 103 (7): 073701.

[48] Department of Energy. Basic Research Needs for Electrical Energy Storage 2007.

[49] Nazri GA, Pistoia G., Lithium Batteries, Springer, 2003.

[50] Huggins RA, Nix WD. Decrepitation model for capacity loss during cycling of alloys in rechargeable electrochemical systems. Ionics 2000; 6: 57.

[51] Kasavajjula U, Wang CS, Appleby AJ. Nano- and bulk-silicon-based insertion anodes for lithium-ion secondary cells. Journal of Power Sources 2007; 163: 1003.

[52] Lazarraga MG, Mandal S, Ibanez J, Amarilla JM, Rojo JM. LiMn2O4-based composites processed by a chemical-route microstructural, electrical, electrochemical, and mechanical characterization. Journal of Power Sources 2003; 115: 315.

[53] Chen GY, Song XY, Richardson TJ. Electron microscopy study of the LiFePO4 to FePO4 phase transition. Electrochemical and Solid State Letters 2006; 9:

A295.

[54] Gabrisch H, Wilcox J, Doeff MM. TEM study of fracturing in spherical and plate-like LiFePO4 particles. Electrochemical and Solid State Letters 2008; 11: A25.

[55] Wilson JR, Cronin JS, Barnett SA, Harris SJ. Measurement of three-dimensional microstructure in a LiCoO2 positive electrode. Journal of Power Sources 2011; 196: 3443.

[56] Christensen J, Newman J. Stress generation and fracture in lithium insertion materials. Journal of Solid State Electrochemistry 2006; 10: 293.

[57] Christensen J, Newman J. A mathematical model of stress generation and fracture in lithium manganese oxide. Journal of the Electrochemical Society 2006; 153: A1019.

[58] Zhang XC, Sastry AM, Shyy W. Intercalation-induced stress and heat generation within single lithium-ion battery cathode particles. Journal of the Electrochemical Society 2008; 155: A542.

[59] Cheng YT, Verbrugge MW. The influence of surface mechanics on diffusion induced stresses within spherical nanoparticles. Journal of Applied Physics 2008; 104: 083521.

[60] Cheng YT, Verbrugge MW. Evolution of stress within a spherical insertion electrode particle under potentiostatic and galvanostatic operation. Journal of Power Sources 2009; 190: 453.

[61] Deshpande R, Cheng YT, Verbrugge MW. Modeling diffusion-induced stress in

nanowire electrode structures. Journal of Power Sources 2010; 195: 5081.

[62] Golmon S, Maute K, Lee SH, Dunn ML. Stress generation in silicon particles during lithium insertion. Applied Physics Letters 2010; 97: 033111.

[63] Haftbaradaran H, Gao HJ, Curtin WA. A surface locking instability for atomic intercalation into a solid electrode. Applied Physics Letters 2010; 96 (9): 091909.

[64] Zhang XC, Shyy W, Sastry AM. Numerical simulation of intercalation-induced stress in Li-ion battery electrode particles. Journal of the Electrochemical Society 2007; 154 (10): A910.

[65] Cheng YT, Verbrugge MW. Diffusion-Induced Stress, Interfacial Charge Transfer, and Criteria for Avoiding Crack Initiation of Electrode Particles. Journal of the Electrochemical Society 2010; 157: A508.

[66] Woodford WH, Chiang Y-M, Carter WC. "Electrochemical Shock" of Intercalation Electrodes: A Fracture Mechanics Analysis. Journal of the Electrochemical Society 2010; 157: A1052.

[67] Bhandakkar TK, Gao HJ. Cohesive modeling of crack nucleation under diffusion induced stresses in a thin strip: Implications on the critical size for flaw tolerant battery electrodes. International Journal of Solids and Structures 2010; 47: 1424.

[68] Aifantis KE, Hackney SA, Dempsey JP. Design criteria for nanostructured Li-ion batteries. Journal of Power Sources 2007; 165: 874.

[69] Bhandakkar TK, Gao HJ. Cohesive modeling of crack nucleation in a cylindrical

electrode under axisymmetric diffusion induced stresses. International Journal of Solids and Structures 2011; 48: 2304.

[70] Evans AG. Microfracture from Thermal-Expansion Anisotropy .1. Single-Phase Systems. Acta Metallurgica 1978; 26: 1845.

[71] Lu TC, Yang J, Suo Z, Evans AG, Hecht R, Mehrabian R. Matrix Cracking in Intermetallic Composites Caused by Thermal-Expansion Mismatch. Acta Metallurgica Et Materialia 1991; 39: 1883.

[72] Hutchinson JW, Suo Z. Mixed-Mode Cracking in Layered Materials. Advances in Applied Mechanics 1991; 29: 63.

[73] Jo M, Hong YS, Choo J, Cho J. Effect of LiCoO2 Cathode Nanoparticle Size on High Rate Performance for Li-Ion Batteries. Journal of the Electrochemical Society 2009; 156: A430.

[74] Wang Y, Cao GZ. Developments in nanostructured cathode materials for high-performance lithium-ion batteries. Advanced Materials 2008; 20: 2251.

[75] Reimers JN, Dahn JR. Electrochemical and Insitu X-Ray-Diffraction Studies of Lithium Intercalation in Li_xCoO_2. Journal of the Electrochemical Society 1992; 139: 2091.

[76] Xie J, Imanishi N, Matsumura T, Hirano A, Takeda Y, Yamamoto O. Orientation dependence of Li-ion diffusion kinetics in LiCoO2 thin films prepared by RF magnetron sputtering. Solid State Ionics 2008; 179: 362.

[77] Hart FX, Bates JB. Lattice model calculation of the strain energy density and other properties of crystalline $LiCoO_2$. Journal of Applied Physics 1998; 83:

7560.

[78] Shenoy VB, Johari P, Qi Y. Elastic softening of amorphous and crystalline Li-Si Phases with increasing Li concentration: A first-principles study. Journal of Power Sources 2010; 195: 6825.

[79] Chan CK, Peng HL, Liu G, McIlwrath K, Zhang XF, Huggins RA, Cui Y. High-performance lithium battery anodes using silicon nanowires. Nature Nanotechnology 2008; 3: 31.

[80] Takamura T, Ohara S, Uehara M, Suzuki J, Sekine K. A vacuum deposited Si film having a Li extraction capacity over 2000 mAh/g with a long cycle life. Journal of Power Sources 2004; 129: 96.

[81] Kim H, Han B, Choo J, Cho J. Three-Dimensional Porous Silicon Particles for Use in High-Performance Lithium Secondary Batteries. Angewandte Chemie-International Edition 2008; 47: 10151.

[82] Sethuraman VA, Chon MJ, Shimshak M, Srinivasan V, Guduru PR. In situ measurements of stress evolution in silicon thin films during electrochemical lithiation and delithiation. Journal of Power Sources 2010; 195: 5062.

[83] Freund LB, Suresh S. Thin film materials. Cambridge University Press, Cambridge. 2003.

[84] Maranchi JP, Hepp AF, Evans AG, Nuhfer NT, Kumta PN. Interfacial properties of the a-Si/Cu : active-inactive thin-film anode system for lithium-ion batteries. Journal of the Electrochemical Society 2006; 153: A1246.

[85] Duduta M, Ho B, Wood VC, Limthongkul P, Brunini VE, Carter WC, Chiang YM.

Semi-Solid Lithium Rechargeable Flow Battery. Advanced Energy Materials 2011; 1: 511.

[86] Bradwell DJ, Kim H, Sirk AHC, Sadoway DR. Magnesium-Antimony Liquid Metal Battery for Stationary Energy Storage. Journal of the American Chemical Society 2012; 134: 1895.

[87] Deshpande RD, Li JC, Cheng YT, Verbrugge MW. Liquid Metal Alloys as Self-Healing Negative Electrodes for Lithium Ion Batteries. Journal of the Electrochemical Society 2011; 158: A845.

[88] Hill R. The Mathematical Theory of Plasticity. Oxford University Press, 1950.

[89] Ding N, Xu J, Yao YX, Wegner G, Fang X, Chen CH, Lieberwirth I. Determination of the diffusion coefficient of lithium ions in nano-Si. Solid State Ionics 2009; 180: 222.

[90] Boukamp BA, Lesh GC, Huggins RA. All-Solid Lithium Electrodes with Mixed-Conductor Matrix. Journal of the Electrochemical Society 1981; 128: 725.

[91] Zhao KJ, Pharr M, Vlassak JJ, Suo ZG. Inelastic hosts as electrodes for high-capacity lithium-ion batteries. Journal of Applied Physics 2011; 109: 016110.

[92] Zhao KJ, Wang WL, Gregoire J, Pharr M, Suo ZG, Vlassak JJ, Kaxiras E. Lithium-Assisted Plastic Deformation of Silicon Electrodes in Lithium-Ion Batteries: A First-Principles Theoretical Study. Nano Letters 2011; 11: 2962.

[93] Choi NS, Yao Y, Cui Y, Cho J. One dimensional Si/Sn - based nanowires and

nanotubes for lithium-ion energy storage materials. Journal of Materials Chemistry 2011; 21: 9825.

[94] Haftbaradaran H, Xiao XC, Verbrugge MW, Gao HJ. Method to deduce the critical size for interfacial delamination of patterned electrode structures and application to lithiation of thin-film silicon islands. Journal of Power Sources 2012; 206: 357.

[95] Yu CJ, Li X, Ma T, Rong JP, Zhang RJ, Shaffer J, An YH, Liu Q, Wei BQ, Jiang HQ. Silicon Thin Films as Anodes for High-Performance Lithium-Ion Batteries with Effective Stress Relaxation. Advanced Energy Materials 2012; 2: 68.

[96] Soni SK, Sheldon BW, Xiao XC, Verbrugge MW, Ahn D, Haftbaradaran H, Gao HJ. Stress Mitigation during the Lithiation of Patterned Amorphous Si Islands. Journal of the Electrochemical Society 2012; 159: A38.

[97] Yao Y, McDowell MT, Ryu I, Wu H, Liu NA, Hu LB, Nix WD, Cui Y. Interconnected Silicon Hollow Nanospheres for Lithium-Ion Battery Anodes with Long Cycle Life. Nano Letters 2011; 11: 2949.

[98] McDowell MT, Lee SW, Ryu I, Wu H, Nix WD, Choi JW, Cui Y. Novel Size and Surface Oxide Effects in Silicon Nanowires as Lithium Battery Anodes. Nano Letters 2011; 11: 4018.

[99] Hertzberg B, Alexeev A, Yushin G. Deformations in Si-Li Anodes Upon Electrochemical Alloying in Nano-Confined Space. Journal of the American Chemical Society 2010; 132: 8548.

[100] Xiao XC, Lu P, Ahn D. Ultrathin Multifunctional Oxide Coatings for Lithium

Ion Batteries. Advanced Materials 2011; 23: 3911.

[101] Chen HX, Xiao Y, Wang L, Yang Y. Silicon nanowires coated with copper layer as anode materials for lithium-ion batteries. Journal of Power Sources 2011; 196: 6657.

[102] Liu Y, Hudak NS, Huber DL, Limmer SJ, Sullivan JP, Huang JY. In Situ Transmission Electron Microscopy Observation of Pulverization of Aluminum Nanowires and Evolution of the Thin Surface Al2O3 Layers during Lithiation-Delithiation Cycles. Nano Letters 2011; 11: 4188.

[103] He Y, Yu XQ, Wang YH, Li H, Huang XJ. Alumina-Coated Patterned Amorphous Silicon as the Anode for a Lithium-Ion Battery with High Coulombic Efficiency. Advanced Materials 2011; 23: 4938.

[104] Leung K, Qi Y, Zavadil KR, Jung YS, Dillon AC, Cavanagh AS, Lee SH, George SM. Using Atomic Layer Deposition to Hinder Solvent Decomposition in Lithium Ion Batteries: First-Principles Modeling and Experimental Studies. Journal of the American Chemical Society 2011; 133: 14741.

[105] Choi NS, Yew KH, Lee KY, Sung M, Kim H, Kim SS. Effect of fluoroethylene carbonate additive on interfacial properties of silicon thin-film electrode. Journal of Power Sources 2006; 161: 1254.

[106] Hu YS, Demir-Cakan R, Titirici MM, Muller JO, Schlogl R, Antonietti M, Maier J. Superior storage performance of a Si@SiOx/C nanocomposite as anode material for lithium-ion batteries. Angewandte Chemie-International Edition 2008; 47: 1645.

[107] Chan CK, Ruffo R, Hong SS, Cui Y. Surface chemistry and morphology of the solid electrolyte interphase on silicon nanowire lithium-ion battery anodes. Journal of Power Sources 2009; 189: 1132.

[108] Holzapfel M, Buqa H, Scheifele W, Novak P, Petrat FM. A new type of nano-sized silicon/carbon composite electrode for reversible lithium insertion. Chemical Communications 2005: 1566.

[109] Holzapfel M, Buqa H, Krumeich F, Novak P, Petrat FM, Veit C. Chemical vapor deposited silicon/graphite compound material as negative electrode for lithium-ion batteries. Electrochemical and Solid State Letters 2005; 8: A516.

[110] Wu H, Chan G, Choi JW, Ryu I, Yao Y, McDowell MT, Lee SW, Jackson A, Yang Y, Hu L, Cui Y. Nature Nanotechnology 2012; 7 (5): 309.

[111] Wu H, Zheng GY, Liu NA, Carney TJ, Yang Y, Cui Y. Engineering Empty Space between Si Nanoparticles for Lithium-Ion Battery Anodes. Nano Letters 2012; 12: 904.

[112] Hwang TH, Lee YM, Kong BS, Seo JS, Choi JW. Electrospun Core-Shell Fibers for Robust Silicon Nanoparticle-Based Lithium Ion Battery Anodes. Nano Letters 2012; 12: 802.

[113] Li X, Meduri P, Chen X, Qi W, Engelhard MH, Xu W, Ding F, Xiao J, Wang W, Wang C, Zhang J, Liu J. J. Mater. Chem. (2012) DOI: 10.1039/c0xx00000x.

[114] Timoshenko S, Goodier JN. Theory of Elasticity, 3rd Edition. Mcgraw-Hill College, Blacklick, OH. 1970.

[115] Zhao KJ, Pharr M, Cai SQ, Vlassak JJ, Suo ZG. Large Plastic Deformation in

High-Capacity Lithium-Ion Batteries Caused by Charge and Discharge. Journal of the American Ceramic Society 2011; 94: S226.

[116] Hertzberg B, Benson J, Yushin G. Ex-situ depth-sensing indentation measurements of electrochemically produced Si-Li alloy films. Electrochemistry Communications 2011; 13: 818.

[117] Sethuraman VA, Chon MJ, Shimshak M, Van Winkle N, Guduru PR. In situ measurement of biaxial modulus of Si anode for Li-ion batteries. Electrochemistry Communications 2010; 12: 1614.

[118] http://accuratus.com/alumox.html.

[119] Cui ZQ, Gao F, Qu JM. A finite deformation stress-dependent chemical potential and its applications to lithium ion batteries. Journal of the Mechanics and Physics of Solids 2012; 60: 1280.

[120] Limthongkul P, Jang YI, Dudney NJ, Chiang YM. Electrochemically-driven solid-state amorphization in lithium-silicon alloys and implications for lithium storage. Acta Materialia 2003; 51: 1103.

[121] Xun S, Song X, Wang L, Grass ME, Liu Z, Battaglia VS, Liu G. The Effects of Native Oxide Surface Layer on the Electrochemical Performance of Si Nanoparticle-Based Electrodes. Journal of the Electrochemical Society 2011; 158: A1260.

[122] Obrovac MN, Christensen L. Structural changes in silicon anodes during lithium insertion/extraction. Electrochemical and Solid State Letters 2004; 7: A93.

[123] Hatchard TD, Dahn JR. In situ XRD and electrochemical study of the reaction of lithium with amorphous silicon. Journal of the Electrochemical Society 2004; 151: A838.

[124] Chon MJ, Sethuraman VA, McCormick A, Srinivasan V, Guduru PR. Real-Time Measurement of Stress and Damage Evolution during Initial Lithiation of Crystalline Silicon. Physical Review Letters 2011; 107: 045503.

[125] Liu XH, Zheng H, Zhong L, Huan S, Karki K, Zhang LQ, Liu Y, Kushima A, Liang WT, Wang JW, Cho JH, Epstein E, Dayeh SA, Picraux ST, Zhu T, Li J, Sullivan JP, Cumings J, Wang CS, Mao SX, Ye ZZ, Zhang SL, Huang JY. Anisotropic Swelling and Fracture of Silicon Nanowires during Lithiation. Nano Letters 2011; 11: 3312.

[126] Lee SW, McDowell MT, Choi JW, Cui Y. Anomalous Shape Changes of Silicon Nanopillars by Electrochemical Lithiation. Nano Letters 2011; 11: 3034.

[127] Goldman JL, Long BR, Gewirth AA, Nuzzo RG. Strain Anisotropies and Self-Limiting Capacities in Single-Crystalline 3D Silicon Microstructures: Models for High Energy Density Lithium-Ion Battery Anodes. Advanced Functional Materials 2011; 21: 2412.

[128] Nye JF. Physical Properties of Crystals: Their Representation by Tensors and Matrices, Oxford University Press, New York. 1985.

[129] Subramanian VR, Ploehn HJ, White RE. Shrinking core model for the discharge of a metal hydride electrode. Journal of the Electrochemical Society 2000; 147: 2868.

[130] Subramanian VR, White RE. New separation of variables method for composite electrodes with galvanostatic boundary conditions. Journal of Power Sources 2001; 96: 385.

[131] Ryu I, Choi JW, Cui Y, Nix WD. Size-dependent fracture of Si nanowire battery anodes. Journal of the Mechanics and Physics of Solids 2011; 59: 1717.

[132] Deshpande R, Cheng Y-T, Verbrugge MW, Timmons A. Diffusion Induced Stresses and Strain Energy in a Phase-Transforming Spherical Electrode Particle. Journal of the Electrochemical Society 2011; 158: A718.

[133] Liu XH, Zhong L, Huang S, Mao SX, Zhu T, Huang JY. Size-Dependent Fracture of Silicon Nanoparticles During Lithiation. ACS Nano 2012; 6: 1522.

[134] Bower AF, Guduru PR, Sethuraman VA. A finite strain model of stress, diffusion, plastic flow, and electrochemical reactions in a lithium-ion half-cell. Journal of the Mechanics and Physics of Solids 2011; 59 (4): 804.

[135] Haftbaradaran H, Song J, Curtin WA, Gao HJ. Continuum and atomistic models of strongly coupled diffusion, stress, and solute concentration. Journal of Power Sources 2011; 196 (1): 361.

[136] Renganathan S, Sikha G, Santhanagopalan S, White RE. Theoretical Analysis of Stresses in a Lithium Ion Cell. Journal of the Electrochemical Society 2010; 157 (2): A155.

[137] Wan WH, Zhang QF, Cui Y, Wang EG. First principles study of lithium insertion in bulk silicon. Journal of Physics-Condensed Matter 2010; 22: 415501.

[138] Bockris J O'M, Reddy AKN, Gamboa-Aldeco M. Modern Electrochemistry, Vol. 2A, Fundamentals of Electrodics, 2nd ed., Kluwer Academic/Plenum Publishers. 2000.

[139] Zhao KJ, Wang WL, Gregoire J, Pharr M, Suo ZG, Vlassak, JJ, Kaxiras E. Lithium-Assisted Plastic Deformation of Silicon Electrodes in Lithium-Ion Batteries: A First-Principles Theoretical Study. Nano Letters 2011; 11: 2962.

[140] Li H, Huang XJ, Chen LQ, Zhou GW, Zhang Z, Yu DP, Mo YJ, Pei N. The crystal structural evolution of nano-Si anode caused by lithium insertion and extraction at room temperature. Solid State Ionics 2000; 135: 181.

[141] Key B, Bhattacharyya R, Morcrette M, Seznec V, Tarascon JM, Grey CP. Real-Time NMR Investigations of Structural Changes in Silicon Electrodes for Lithium-Ion Batteries. Journal of the American Chemical Society 2009; 131: 9239.

[142] Key B, Morcrette M, Tarascon JM, Grey CP. Pair Distribution Function Analysis and Solid State NMR Studies of Silicon Electrodes for Lithium Ion Batteries: Understanding the (De)lithiation Mechanisms. Journal of the American Chemical Society 2011; 133: 503.

[143] Zhao KJ, Pharr M, Wan Q, Wang WL, Kaxiras E, Vlassak JJ, Suo ZG. Concurrent Reaction and Plasticity during Initial Lithiation of Crystalline Silicon in Lithium-Ion Batteries. Journal of the Electrochemical Society 2012; 159: A238.

[144] Yang H, Huang S, Huang X, Fan FF, Liang WT, Liu XH, Chen LQ, Huang JY, Li

J, Zhu T, Zhang SL. Orientation-Dependent Interfacial Mobility Governs the Anisotropic Swelling in Lithiated Silicon Nanowires. Nano Letters 2012; 12: 1953.

[145] Li J, Dahn JR. An in situ X-ray diffraction study of the reaction of Li with crystalline Si. Journal of the Electrochemical Society 2007; 154: A156.

[146] Zhao KJ, Tritsaris AG, Pharr M, Wang WL, Okeke O, Suo ZG, Vlassak JJ, Kaxiras E. Reactive Flow in Silicon Electrodes Assisted by the Insertion of Lithium. Nano Letters 2012; 12 (8); 4397.

[147] Deal BE, Grove AS. General Relationship for Thermal Oxidation of Silicon. Journal of Applied Physics 1965; 36: 3770.

[148] Li JC, Xiao XC, Yang FQ, Verbrugge MW, Cheng YT. Potentiostatic Intermittent Titration Technique for Electrodes Governed by Diffusion and Interfacial Reaction. Journal of Physical Chemistry C 2012; 116: 1472.

[149] Gonzalez C, McVittie JP. A Study of Trenched Capacitor Structures. IEEE Electron Device Letters 1985; 6: 215.

[150] Kao DB, McVittie JP, Nix WD, Saraswat KC. Two-Dimensional Thermal-Oxidation of Silicon. 1. Experiments. IEEE Transactions on Electron Devices 1987; 34: 1008.

[151] Xie J, Imanishi N, Zhang T, Hirano A, Takeda Y, Yamamoto O. Li-ion diffusion in amorphous Si films prepared by RF magnetron sputtering: A comparison of using liquid and polymer electrolytes. Materials Chemistry and Physics 2010; 120: 421.

[152] Baggetto L, Danilov D, Notten PHL. Honeycomb-Structured Silicon: Remarkable Morphological Changes Induced by Electrochemical (De)Lithiation. Advanced Materials 2011; 23: 1563.

[153] Yamada M, Ueda A, Matsumoto K, Ohzuku T. Silicon-Based Negative Electrode for High-Capacity Lithium-Ion Batteries: "SiO"-Carbon Composite. Journal of the Electrochemical Society 2011; 158: A417.

[154] Freund LB, Suresh S. Thin Film Materials: Stress, Defect Formation and Surface Evolution. Cambridge, UK: Cambridge University Press; 2003.

[155] Lee SW, McDowell MT, Berla LA, Nix WD, Cui Y. Fracture of crystalline silicon nanopillars during electrochemical lithium insertion. Proceedings of the National Academy of Sciences of the United States of America 2012; 109: 4080.

[156] Soni SK, Sheldon BW, Xiao X, Tokranov A. Thickness effects on the lithiation of amorphous silicon thin films. Scripta Materialia 2011; 64: 307.

[157] Kushima A, Huang JY, Li J. Quantitative Fracture Strength and Plasticity Measurements of Lithiated Silicon Nanowires by In Situ TEM Tensile Experiments. ACS Nano 2012; 6: 9425.

[158] Aifantis KE, Hackney SA. Mechanical stability for nanostructured Sn- and Si-based anodes. Journal of Power Sources 2011; 196: 2122.

[159] Xiao X, Liu P, Verbrugge MW, Haftbaradaran H, Gao H. Improved cycling stability of silicon thin film electrodes through patterning for high energy density lithium batteries. Journal of Power Sources 2011; 196: 1409.

[160] Gao YF, Zhou M. Coupled mechano-diffusional driving forces for fracture in

electrode materials. Journal of Power Sources 2013; 230: 176.

[161] Peng K, Jie J, Zhang W, Lee S-T. Silicon nanowires for rechargeable lithium-ion battery anodes. Applied Physics Letters 2008; 93: 033105.

[162] Stoney GG. The tension of metallic films deposited by electrolysis. Proceedings of the Royal Society of London Series A-Containing Papers of a Mathematical and Physical Character 1909; 82: 172.

[163] Nix WD. Mechanical Properties of Thin Films. Metallurgical Transactions A-Physical Metallurgy and Materials Science 1989; 20: 2217.

[164] Obrovac MN, Krause LJ. Reversible cycling of crystalline silicon powder. Journal of the Electrochemical Society 2007; 154: A103.

[165] He Y, Yu X, Li G, Wang R, Li H, Wang Y, Gao H, Huang X. Shape evolution of patterned amorphous and polycrystalline silicon microarray thin film electrodes caused by lithium insertion and extraction. Journal of Power Sources 2012; 216: 131.

[166] Beaulieu LY, Hatchard TD, Bonakdarpour A, Fleischauer MD Dahn JR. Reaction of Li with alloy thin films studied by in situ AFM. Journal of the Electrochemical Society 2003; 150 (11): A1457.

[167] McArthur MA, Trussler S, Dahn JR. In Situ Investigations of SEI Layer Growth on Electrode Materials for Lithium-Ion Batteries Using Spectroscopic Ellipsometry. Journal of the Electrochemical Society 2012; 159 (3): A198.

[168] Pharr M, Zhao KJ, Wang XW, Suo ZG, Vlassak JJ. Kinetics of Initial Lithiation of Crystalline Silicon Electrodes of Lithium-Ion Batteries. Nano Letters 2012;

12, (9): 5039.

[169] McDowell MT, Lee SW, Harris JT, Korgel BA, Wang C, Nix WD, Cui Y. In Situ TEM of Two-Phase Lithiation of Amorphous Silicon Nanospheres. Nano Letters 2013; 13 (2): 758.

[170] Wang JW, He Y, Fan FF, Liu XH, Xia SM, Liu Y, Harris CT, Li H, Huang JY, Mao SX, Zhu T. Two-Phase Electrochemical Lithiation in Amorphous Silicon. Nano Letters 2013; 13 (2): 709.

[171] Nakamura T, Kamath SM. 3-Dimensional Effects in Thin-Film Fracture-Mechanics. Mechanics of Materials 1992; 13 (1): 67.

[172] Beuth JL. Cracking of Thin Bonded Films in Residual Tension. International Journal of Solids and Structures 1992; 29: 1657.

[173] Hutchinson JW. Fundamentals of the Phenomenological Theory of Non-Linear Fracture-Mechanics. Journal of Applied Mechanics-Transactions of the ASME 1983; 50: 1042.

[174] Lu N, Wang X, Suo Z, Vlassak J. Metal films on polymer substrates stretched beyond 50%. Applied Physics Letters 2007; 91: 221909.

[175] Lu N, Suo Z, Vlassak JJ. The effect of film thickness on the failure strain of polymer-supported metal films. Acta Materialia 2010; 58: 1679.

[176] Ballarini R, Kahn H, Tayebi N, Heuer AH. Effects of Microstructure on the Strength and Fracture Toughness of Polysilicon: A Wafer Level Testing Approach. In: Mechanical Properties of Structural Films. Orlando, FL: American Society for Testing and Materials; 2001: 37.

[177] Ballarini R, Mullen RL, Yin Y, Kahn H, Stemmer S, Heuer AH. The fracture toughness of polysilicon microdevices: A first report. Journal of Materials Research 1997; 12: 915.

[178] Chen CP, Leipold MH. Fracture-Toughness of Silicon. American Ceramic Society Bulletin 1980; 59: 469.

[179] Deshpande R, Verbrugge M, Cheng YT, Wang J, Liu P. Battery Cycle Life Prediction with Coupled Chemical Degradation and Fatigue Mechanics. Journal of the Electrochemical Society 2012; 159: A1730.

[180] Zhang H, Braun PV. Three-Dimensional Metal Scaffold Supported Bicontinuous Silicon Battery Anodes. Nano Letters 2012; 12: 2778.

[181] Huang JY, Zhong L, Wang CM, Sullivan JP, Xu W, Zhang LQ, Mao SX, Hudak NS, Liu XH, Subramanian A, Fan H, Qi L, Kushima A, Li J. In Situ Observation of the Electrochemical Lithiation of a Single SnO2 Nanowire Electrode. Science 2010; 330: 1515.

[182] Fan F, Huang S, Yang H, Raju M, Datta D, Shenoy VB, van Duin ACT, Zhang S, Zhu T. Mechanical properties of amorphous LixSi alloys: a reactive force field study. Modelling and Simulation in Materials Science and Engineering 2013; 21.

[183] Huang S, Zhu T. Atomistic mechanisms of lithium insertion in amorphous silicon. Journal of Power Sources 2011; 196: 3664.

[184] Brassart L, Suo Z. Reactive Flow in Large-Deformation Electrodes of Lithium-Ion Batteries. International Journal of Applied Mechanics 2012; 4 (3).

[185] Brassart L, Suo Z. Reactive flow in solids. Journal of the Mechanics and Physics of Solids 2013; 61: 61.

[186] Cui Z, Gao F, Cui Z, Qu J. A second nearest-neighbor embedded atom method interatomic potential for Li-Si alloys. Journal of Power Sources 2012; 207: 150.

[187] Sheldon BW, Soni SK, Xiao X, Qi Y. Stress Contributions to Solution Thermodynamics in Li-Si Alloys. Electrochemical and Solid State Letters 2012; 15: A9.

[188] Soni SK, Sheldon BW, Xiao X, Bower AF, Verbrugge MW. Diffusion Mediated Lithiation Stresses in Si Thin Film Electrodes. Journal of the Electrochemical Society 2012; 159: A1520.

[189] Zhao KJ, Li YG, Brassart L. Pressure-sensitive plasticity of lithiated silicon in Li-ion batteries. Acta Mechanica Sinica 2013; 29: 379.

[190] Bucci G, Nadimpalli SPV, Sethuraman VA, Bower AF, Guduru PR. Measurement and modeling of the mechanical and electrochemical response of amorphous Si thin film electrodes during cyclic lithiation. Journal of the Mechanics and Physics of Solids 2014; 62: 276.

[191] Bower AF, Guduru PR, Sethuraman VA. A finite strain model of stress, diffusion, plastic flow, and electrochemical reactions in a lithium-ion half-cell. Journal of the Mechanics and Physics of Solids 2011; 59: 804.

[192] Chaboche JL. Constitutive Equations for Cyclic Plasticity and Viscoplasticity. International Journal of Plasticity 1989; 5: 247.

[193] Boles ST, Thompson CV, Kraft O, Moenig R. In situ tensile and creep testing of

lithiated silicon nanowires. Applied Physics Letters 2013; 103: 263906.

[194] Spaepen F. A microscopic mechanism for steady state in homogeneous flow in metallic glasses. Acta Metallurgica 1977; 25: 407.

[195] Heggen M, Spaepen F, Feuerbacher M. Creation and annihilation of free volume during homogeneous flow of a metallic glass. Journal of Applied Physics 2005; 97: 033506.

[196] Egami T, Iwashita T, Dmowski W. Mechanical Properties of Metallic Glasses. Metals 2013; 3: 77.

Appendix

Appendix A: Stresses in coated and hollow silicon nanowires (Chapter 5)

Here, we derive the stress field in a hollow silicon nanowire coated with a stiff shell. The geometry of the cross section is shown in Figure 5.3. We represent a material element in the reference configuration, Figure 5.3a, by its distance R from the center of the nanowire. At time t, it moves to a place at a distance r from the center, Figure 5.3b. The function $r(R, t)$ specifies the deformation kinematics of the silicon nanowire. Due to the constraint imposed by the shell, lithiated silicon is assumed to deform under the plane-strain conditions. To focus on the main ideas, we neglect the elasticity of both the core and the shell; we model the lithiated silicon as a rigid-plastic material. Consequently, the expansion of lithiated silicon is entirely due to lithiation. Consider an annulus of the lithiated silicon between the radii B and r. This annulus is lithiated from the annulus of pristine silicon between the radii B and R. We assume that the rate of lithiation is slow relative to diffusion of Li in the core, so that Li atoms have enough time to homogenize in the core. That is, the ratio of the volume of the lithiated silicon over the volume of pristine silicon $\tilde{\beta}$, is taken to be homogeneous and evolves in time. Upon full lithiation, $\tilde{\beta}$ reaches $\tilde{\beta}=4$ for silicon. Thus,

$$B^2 - r^2 = \tilde{\beta}\left(B^2 - R^2\right). \tag{A1}$$

This equation gives the function $r(R, t)$ once the function $\tilde{\beta}(t)$ is given. That is,

$\tilde{\beta}(t)$ fully specifies the kinematics of the silicon nanowire,

$$r = \sqrt{B^2 - \tilde{\beta}\left(B^2 - R^2\right)}. \tag{A2}$$

The stretches can be calculated as

$$\lambda_r = \frac{\partial r}{\partial R} = \frac{R\tilde{\beta}}{r}, \quad \lambda_\theta = \frac{r}{R}, \quad \lambda_z = 1. \tag{A3}$$

We decompose the stretches by writing

$$\lambda_r = \lambda_r^p \tilde{\beta}^{1/3}, \quad \lambda_\theta = \lambda_\theta^p \tilde{\beta}^{1/3}, \quad \lambda_z = \lambda_z^p \tilde{\beta}^{1/3}, \tag{A4}$$

where $\tilde{\beta}$ represents the volume change due to the insertion of Li, and the plastic stretch λ^p represents the shape change during lithiation. The volume change has been assumed to be isotropic for amorphous silicon. We can calculate the strain components from the stretches,

$$\varepsilon_r = \log \lambda_r, \quad \varepsilon_\theta = \log \lambda_\theta, \quad \varepsilon_z = \log \lambda_z. \tag{A5}$$

The incremental plastic deformation is given by

$$\begin{aligned}
\delta\varepsilon_r^p &= \delta \log \lambda_r - \frac{1}{3}\delta \log \tilde{\beta} = \left(\frac{1}{6} + \frac{1}{2}\frac{B^2}{r^2}\right)\frac{\delta\tilde{\beta}}{\tilde{\beta}}, \\
\delta\varepsilon_\theta^p &= \delta \log \lambda_\theta - \frac{1}{3}\delta \log \tilde{\beta} = \left(\frac{1}{6} - \frac{1}{2}\frac{B^2}{r^2}\right)\frac{\delta\tilde{\beta}}{\tilde{\beta}}, \quad . \\
\delta\varepsilon_z^p &= \delta \log \lambda_z - \frac{1}{3}\delta \log \tilde{\beta} = -\frac{1}{3}\frac{\delta\tilde{\beta}}{\tilde{\beta}}
\end{aligned} \tag{A6}$$

The equivalent plastic strain is

$$\delta\varepsilon_{eq}^p = \sqrt{\frac{2}{3}\delta\varepsilon_{ij}^p \delta\varepsilon_{ij}^p} = \frac{\delta\tilde{\beta}}{\tilde{\beta}}\sqrt{\frac{1}{9} + \frac{1}{3}\frac{B^4}{r^4}}. \tag{A7}$$

We adopt the flow rule

$$s_{ij} = \frac{2}{3}\frac{\sigma_Y}{\delta\varepsilon_{eq}^p}\delta\varepsilon_{ij}^p, \tag{A8}$$

where s_{ij} is the deviatoric stress, defined as $s_{ij} = \sigma_{ij} - \frac{1}{3}\sigma_{ii}\delta_{ij}$, and σ_Y the yield strength of lithiated silicon. Therefore,

$$
\begin{aligned}
s_r &= \frac{\sigma_Y}{\sqrt{\frac{1}{9}+\frac{1}{3}\frac{B^4}{r^4}}}\left(\frac{1}{9}+\frac{1}{3}\frac{B^2}{r^2}\right), \\
s_\theta &= \frac{\sigma_Y}{\sqrt{\frac{1}{9}+\frac{1}{3}\frac{B^4}{r^4}}}\left(\frac{1}{9}-\frac{1}{3}\frac{B^2}{r^2}\right), \quad , \\
s_z &= -\frac{2}{9}\frac{\sigma_Y}{\sqrt{\frac{1}{9}+\frac{1}{3}\frac{B^4}{r^4}}}
\end{aligned}
\tag{A9}
$$

and

$$
\sigma_r - \sigma_\theta = s_r - s_\theta = \frac{2\sigma_Y}{\sqrt{r^4/B^4+3}} \quad . \tag{A10}
$$

Consider the force balance of a material element in lithiated silicon

$$
\frac{\partial \sigma_r}{\partial r} + \frac{\sigma_r - \sigma_\theta}{r} = 0 ; \tag{A11}
$$

the radial stress can be obtained by integrating Equation (A11), giving

$$
\sigma_r = -\frac{\sqrt{3}}{3}\sigma_Y \log\frac{\sqrt{r^4+3B^4}-\sqrt{3}B^2}{r^2} + D, \qquad a \le r \le B , \tag{A12}
$$

where D is the integration constant. With the traction-free boundary condition, $\sigma_r(a, t) = 0$,

$$
\sigma_r = -\frac{\sqrt{3}}{3}\sigma_Y\left(2\log\frac{a}{r} + \log\frac{\sqrt{r^4+3B^4}-\sqrt{3}B^2}{\sqrt{a^4+3B^4}-\sqrt{3}B^2}\right), \qquad a \le r \le B . \tag{A13}
$$

The stresses along hoop and axial directions are obtained from Equations (A10) and (A9),

$$
\begin{aligned}
\sigma_\theta &= \sigma_r - \frac{2\sigma_Y}{\sqrt{r^4/B^4+3}} \\
\sigma_z &= \sigma_r - \frac{\sigma_Y}{\sqrt{r^4/B^4+3}} - \frac{\sigma_Y}{\sqrt{3B^4/r^4+1}}
\end{aligned} \quad . \tag{A14}
$$

Therefore the radial stress at the interface $r = B$ is given by,

$$\sigma_r = -\frac{\sqrt{3}}{3}\sigma_Y\left(2\log\frac{a}{B}+\log\frac{\left(2-\sqrt{3}\right)B^2}{\sqrt{a^4+3B^4}-\sqrt{3}B^2}\right). \tag{A15}$$

In the fully lithiated state of a hollow silicon nanowire, $a \ll B$. The radial stress at the interface can then be approximated by a Taylor expansion, which gives

$$\sigma_r \approx \frac{2\sqrt{3}}{3}\sigma_Y \log\frac{a}{B}. \tag{A16}$$

The stress field in the elastic shell can be solved using the familiar solution of Lamé problem,[114] giving,

$$\begin{aligned}
\sigma_r &= -\frac{2\sqrt{3}}{3}\sigma_Y\left(\log\frac{a}{B}\right)\left(\frac{B^2}{C^2-B^2}\right)\left(1-\frac{C^2}{r^2}\right),\\
\sigma_\theta &= -\frac{2\sqrt{3}}{3}\sigma_Y\left(\log\frac{a}{B}\right)\left(\frac{B^2}{C^2-B^2}\right)\left(1+\frac{C^2}{r^2}\right), \qquad B<r\le C.\\
\sigma_z &= -\frac{2\sqrt{3}}{3}\sigma_Y\left(\log\frac{a}{B}\right)\left(\frac{2\nu B^2}{C^2-B^2}\right).
\end{aligned} \tag{A17}$$

Similar to the analysis of a sphere, the energy release rate in the coating shell takes the following solution:

$$G_f = \frac{8}{3}\frac{{\sigma_Y}^2}{E_s}\left(\log\frac{B}{a}\right)^2\left(\frac{B^2}{C^2-B^2}\right)^2\left(1+\frac{C^2}{B^2}\right)^2(C-B). \tag{A18}$$

During delithiation, the tensile radial stress in silicon at the interface becomes

$$\sigma_r \approx \frac{2\sqrt{3}}{3}\sigma_Y \log\frac{B}{a}. \tag{A19}$$

Thus, using Equation (5.14), the energy release rate for interfacial debonding takes the solution

$$G_d = \frac{4\pi}{3}\frac{{\sigma_Y}^2}{E_e}\left(\log\frac{B}{a}\right)^2(C-B). \tag{A20}$$

Appendix B: Supporting Information for Chapter 7

B.1 Electrochemical Measurements on {100} and {111} Si wafers

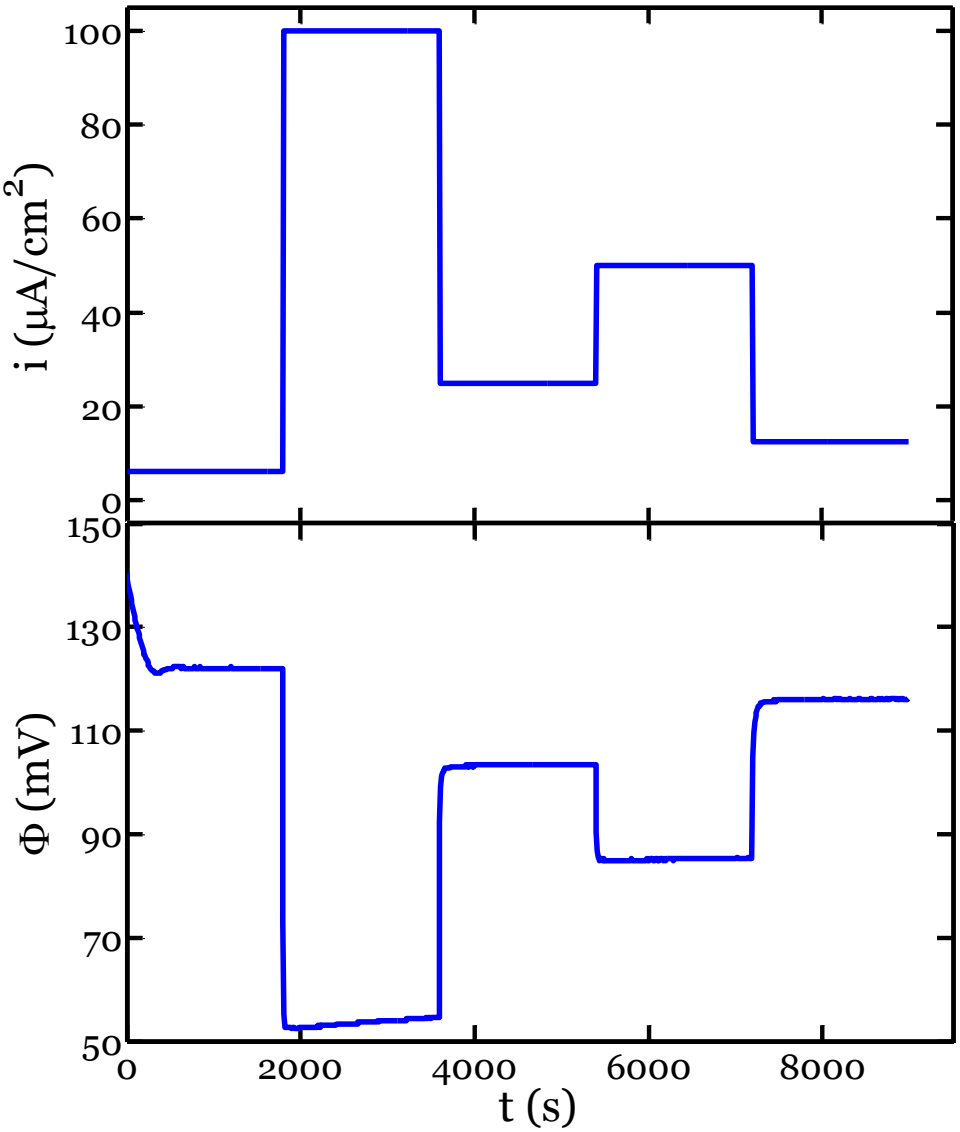

Figure B.1. Typical sequence of applied current density, i, and measured response of the potential vs. Li/Li^+, Φ, for a {100} Si wafer.

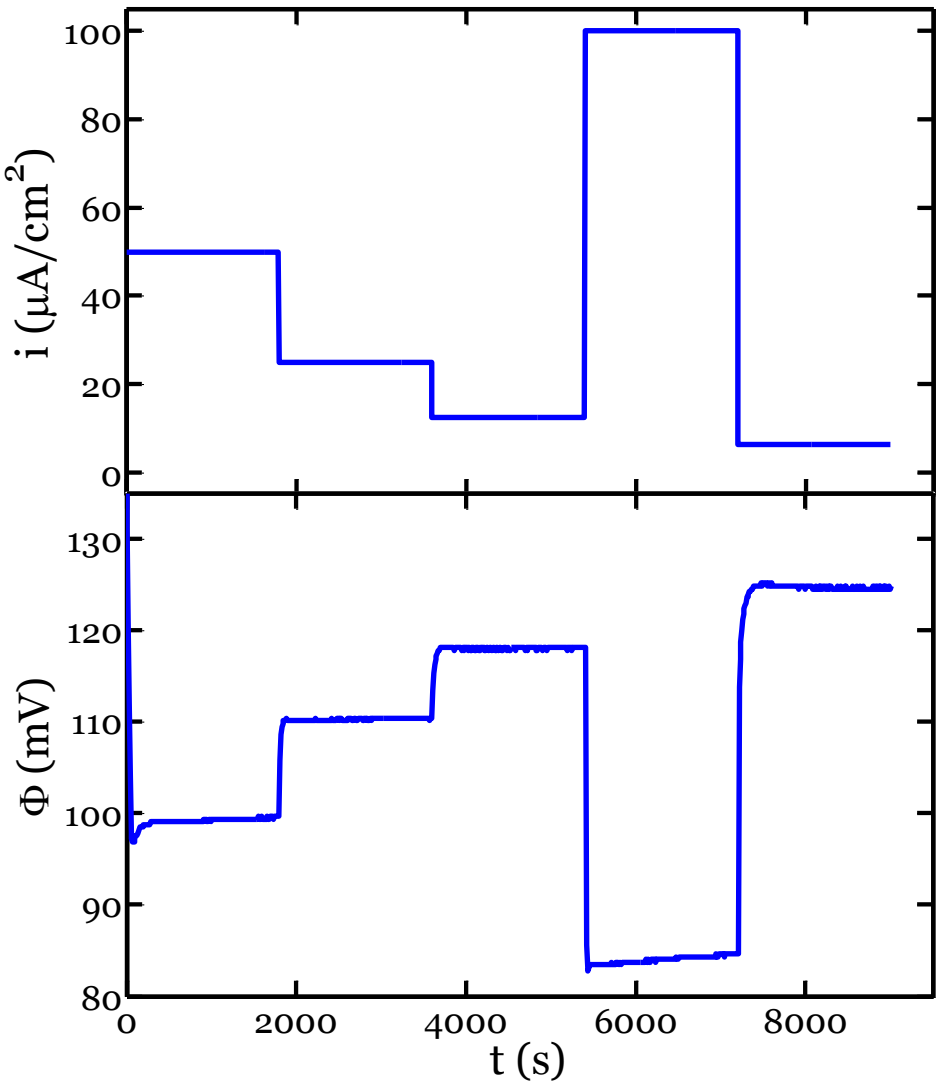

Figure B.2. Typical sequence of applied current density, i, and measured response of the potential vs. Li/Li^+, Φ, for a {111} Si wafer.

B.2 Derivation of kinetic model

The redox reaction at the electrolyte/ a-$Li_\eta Si$ interface is given by

$$Li^+ + e^- = Li\,. \tag{B1}$$

Associated with this redox reaction, we take the current density through the electrolyte/ a-$Li_\eta Si$ interface as given by the Butler-Volmer equation:

$$i = i_o\left[\exp\left(-\frac{\alpha F}{RT}\left[\Phi - \Phi_{eq}{}^{curr}\right]\right) - \exp\left(\frac{[1-\alpha]F}{RT}\left[\Phi - \Phi_{eq}{}^{curr}\right]\right)\right], \tag{B2}$$

where i is the current density, i_o is the exchange current density, α is the charge transfer coefficient, F is Faraday's constant, R is the ideal gas constant, T is the temperature, Φ is the potential of the electrode (i.e., the measured voltage), and $\Phi_{eq}{}^{curr}$ is the equilibrium potential in the current state, corresponding to the lithium concentration in the electrode near the electrolyte/ a-$Li_\eta Si$ interface. Here, we have neglected mass transport through the electrolyte, i.e., we do not consider the concentration polarization. For comparison to our experiments, we believe this assumption should be valid because of the relatively small currents in our tests. Additionally, in general the exchange current density can be a function of the lithium concentration in the electrode near the electrolyte/ a-$Li_\eta Si$ interface. However, in this model, we will examine small changes in concentration from a metastable phase, a-$Li_\eta Si$, and hence i_o will be taken as a constant. Also, since the redox reaction involves one electron per lithium atom, the flux is given by $J = i/q$, where q is the elementary charge. Taking $\alpha = 1/2$ for simplicity, we get

$$J_1 = 2\frac{i_o}{q}\sinh\left[-\frac{F}{2RT}\left(\Phi - \Phi_{eq}{}^{curr}\right)\right]. \tag{B3}$$

In the lithiated phase, $\eta+\delta$ is the number of lithium atoms hosted by each silicon atom. We regard η as a constant and δ as a small deviation, $\delta \ll \eta$. As a result, the diffusion of lithium atoms in the lithiated silicon phase is driven by the position-dependence of the composition, $\delta(y)$, where y is the position as shown in Figure 7.3. Let C be the concentration of lithium in the lithiated phase (i.e., the amount of lithium per unit volume of the lithiated phase). The concentration of lithium in this phase relates to the composition by $C=(\eta+\delta)/\Omega_{\mathrm{Li}_\eta\mathrm{Si}}$, where $\Omega_{\mathrm{Li}_\eta\mathrm{Si}}$ is the atomic volume of the lithiated phase. We take the flux, J_2, to be driven by the gradient in the concentration of lithium through the thickness of the lithiated silicon:

$$J_2 = -D\frac{\partial C}{\partial y}, \tag{B4}$$

where D is the diffusivity of lithium in the lithiated silicon. Because $\delta \ll \eta$, D is taken to be a constant, independent of the concentration. In general, the flux of lithium is driven by the gradient in chemical potential. In writing Equation (B4), we have taken the concentration gradient as the sole driving force, i.e., we have neglected any other driving forces such as those due to stress gradients. This assumption should be valid for a planar geometry for which the stress is constant through the thickness of the lithiated silicon.[143] In support of this hypothesis, Chon, et al. experimentally observed a constant stress, independent of time, during the lithiation process for {100} Si wafers.[124]

In the steady state, the flux is independent of position, and the concentration is linear in the position, so that

$$J_2 = D\frac{C_1 - C_2}{y_0}, \tag{B5}$$

where C_1 is the concentration of lithium in the lithiated silicon at the interface between the electrolyte and the lithiated silicon, C_2 is the concentration of lithium in the lithiated silicon at the interface between the lithiated silicon and crystalline silicon phases, and y_0 is the thickness of the lithiated silicon.

At the interface between the lithiated silicon and the crystalline silicon phases, a chemical reaction occurs:

$$(\eta + \delta)\mathrm{Li} + \mathrm{Si} = \mathrm{Li}_{\eta+\delta}\mathrm{Si}. \tag{B6}$$

The reaction is driven by the excess lithium δ_2 in the lithiated silicon at this interface. The rate of reaction controls the flux of lithium across the interface. For simplicity, we take the flux corresponding to this reaction to be given by the first-order relation:

$$J_3 = k\frac{\delta_2}{\Omega_{\mathrm{Li}_\eta\mathrm{Si}}}, \tag{B7}$$

where k is the rate of the reaction. In general, the flux, J_3, may have a nonlinear dependence on δ_2. However, Equation (B7) should be valid to first order for $\delta << \eta$. Additionally, we propose that k is a function of the crystallographic orientation, as is consistent with the experiments in this paper.

In the steady state, all of the fluxes are equal: $J_1 = J_2 = J_3$. In a unit time, dt, the number of atoms that react to form new lithiated silicon is $J_3 \cdot A \cdot dt$, where A is the cross-sectional area of the planar interface. During this time, dt, the reaction increases the volume of the a-$\mathrm{Li}_\eta\mathrm{Si}$ layer by $J_3 \cdot A \cdot dt \cdot \Omega_{\mathrm{Li}_\eta\mathrm{Si}} / \eta$. As a

result, the thickness of the lithiated silicon phase increases by $dy_o = J_3 \cdot dt \cdot \Omega_{Li_\eta Si} / \eta$ so that the instantaneous velocity of phase boundary is given by

$$\frac{dy_o}{dt} = \frac{\Omega_{Li_\eta Si}}{\eta} J_3, \tag{B8}$$

We will take the quantity $\Omega_{Li_\eta Si} / \eta$ as a constant, which is valid for small changes in composition, $\delta << \eta$. In fact, more generally, this quantity has been found to be constant for large values of $\eta + \delta$.[146]

Since $J_1 = J_3$ in the steady state, the velocity of the phase boundary is given by:

$$\frac{dy_o}{dt} = 2 \frac{\Omega_{Li_\eta Si}}{\eta} \frac{i_o}{q} \sinh\left[-\frac{F}{2RT} \left(\Phi - \Phi_{eq}^{curr} \right) \right]. \tag{B9}$$

From the Nernst equation, the equilibrium potential, Φ_{eq}, is given by

$$\Phi_{eq} = -\frac{RT}{F} \ln(\gamma x_1), \tag{B10}$$

where the reference electrode is taken to be that of pure metallic Li. The parameter γ is the activity coefficient, which in general can be a function of the concentration, and x_1 denotes the mole fraction of lithium atoms in a-$Li_\eta Si$ at the interface with the electrolyte. If the composition of the amorphous lithiated region at the interface with the electrolyte is given by $Li_{\eta+\delta_1} Si$, the mole fraction is

$$x_1 = \frac{\#\text{Li atoms}}{\#\text{Li atoms} + \#\text{Si atoms}} = \frac{\eta + \delta_1}{\eta + \delta_1 + 1}. \tag{B11}$$

Let Φ_{eq}^{ref} denote the equilibrium potential in the reference state, corresponding to a-$Li_\eta Si$. Noting that $\Phi - \Phi_{eq}^{curr} = \Phi - \Phi_{eq}^{ref} - \left(\Phi_{eq}^{curr} - \Phi_{eq}^{ref} \right)$, and combining with Equation (B10):

$$\Phi - \Phi_{eq}^{\ curr} = \Phi - \Phi_{eq}^{\ ref} - \left[-\frac{RT}{F} \ln\left(\gamma \frac{\eta + \delta_1}{\eta + \delta_1 + 1} \right) + \frac{RT}{F} \ln\left(\gamma \frac{\eta}{\eta + 1} \right) \right]. \quad \text{(B12)}$$

Expanding this equation for $\delta_1 << \eta$ to first order gives:

$$\Phi - \Phi_{eq}^{\ curr} = \Phi - \Phi_{eq}^{\ ref} + \frac{RT}{F} \left[\frac{\delta_1}{\eta(\eta + 1)} \right]. \quad \text{(B13)}$$

Since $C = (\eta + \delta)/\Omega_{\mathrm{Li}_\eta\mathrm{Si}}$ and $J_2 = J_3$ in the steady-state:

$$\delta_1 = \left(\frac{k y_0}{D} + 1 \right) \delta_2. \quad \text{(B14)}$$

Combining Equations (B7)-(B9), (B13) and (B14) we obtain:

$$\frac{dy_0}{dt} = 2 \frac{\Omega_{\mathrm{Li}_\eta\mathrm{Si}}}{\eta} \frac{i_0}{q} \sinh\left\{ -\frac{F}{2RT} \left(\Phi - \Phi_{eq}^{\ ref} + \frac{RT}{F} \left[\frac{1}{(\eta + 1)} \left(1 + \frac{k y_0}{D} \right) \frac{1}{k} \frac{dy_0}{dt} \right] \right) \right\}. \quad \text{(B15)}$$

This is an implicit equation for the instantaneous velocity of the phase boundary, dy_0/dt, as a function of measured potential, Φ. Recalling that $J = i/q$, we get an implicit relationship between the applied current density and the measured potential:

$$\frac{i}{i_0} = 2 \sinh\left\{ -\frac{F}{2RT} \left(\Phi - \Phi_{eq}^{\ ref} + \frac{RT}{F} \left[\frac{\Omega_{\mathrm{Li}_\eta\mathrm{Si}}}{q\eta(\eta + 1)} \left(1 + \frac{k y_0}{D} \right) \frac{1}{k} i \right] \right) \right\}. \quad \text{(B16)}$$